Irradiation effects of swift heavy ions in matter

Dissertation

zur Erlangung des Grades
Doktor der Naturwissenschaften

an der Fakultät für Physik
der Universität Duisburg–Essen

von

Orkhan Osmani

aus

Essen

Erstgutachter: Prof. Dr. rer.nat. Marika Schleberger

Zweitgutachter: Dr. Bärbel Rethfeld

Tag der mündlichen Prüfung: 22. Dezember 2011

Erklärung

Hiermit versichere ich, dass ich die vorliegende Arbeit selbstständig verfasst und ohne unzulässige Hilfe Dritter und ohne Benutzung anderer als der angegebenen Hilfsmittel angefertigt habe. Die verwendeten Hilfsmittel und alle wörtlich oder inhaltlich übernommenen Stellen sind unter Angabe der Quelle gekennzeichnet.

Die Arbeit wurde bisher weder im Inland noch im Ausland in gleicher oder ähnlicher Form einer anderen Prüfungsbehörde vorgelegt.

Der Doktorgrad eines Doktors der Naturwissenschaften (Dr. rer. nat.) wird gemäß §1 Satz 2 der Promotionsordnung angestrebt.

Duisburg, den 14. Oktober 2011

Orkhan Osmani

Abstract

In the this thesis irradiation effects of swift heavy ions in matter are studied. The focus lies on the projectiles charge exchange and energy loss processes.

A commonly used computer code which employs rate equations is the so called ETACHA code. This computer code is capable to also calculate the required input cross–sections. Within this thesis a new model to compute the charge state of swift heavy ions is explored. This model, the so called matrix method, takes the form of a simple algebraic expression, which also requires cross–sections as input. In the present implementation of the matrix method, cross–sections are taken from the ETACHA code, while excitation and deexcitation processes are neglected.

Charge fractions for selected ion/target combinations, computed by the ETACHA code and the matrix method are compared. It is shown, that for sufficient large ion energies, both methods agree very well with each other. However, for lower energies pronounced differences are observed. These differences are believed to stem from the fact, that no excited states as well as the decay of theses excited states are included in the present implementation of the matrix method. Both methods are then compared with experimental measurements, where significant deviations are observed for both methods. While the predicted equilibrium charge state by both methods is in good agreement with the experiments, the matrix method predicts a much too large equilibrium thickness compared to both the ETACHA calculation as well as the experiment. Again, these deviations are believed to stem from the fact, that excitation and the decay of excited states are not included in the matrix method. A possible way to include decay processes into the matrix method is presented, while the accuracy of the applied capture cross–sections is tested by comparison with scaling rules.

Swift heavy ions penetrating a dielectric are known to induced structural modifications both on the surface and in the bulk, so called ion tracks. In order to describe this track creation, the so called two temperature model (TTM) is often used. This TTM is based on a set of two coupled heat diffusion equations, describing the heat transport of the electrons and the phonons, while both equations are coupled by an exchange parameter, the so called electron–phonon coupling parameter. Within the TTM material parameters like the (excited) electron density, the electron heat capacity and the electron–phonon coupling are required. These parameters are often unknown, especially for insulators or semiconductors. In this work, the TTM is applied to the case of crystalline silicon, where the so called damage threshold, *i.e.* the minimal required ion energy to induce a modification, is calculated. It is demonstrated that without a profound knowledge of the material parameters, especially the excited electron density and the electron–phonon coupling, a reliable estimation of the damage threshold, for instance cannot be achieved. In order to determine the density of excited electrons Monte Carlo (MC) simulations of the penetration of a swift heavy ion in matter are presented. As a model system the irradiation of 11.4 MeV/u Ca^{19+} in SiO_2 is chosen. Within the MC method spatial and temporal profiles of the electron energy and number density are calculated. Using this data a method is presented that allows to obtain the electron temperature and the transport properties of the electrons. A criterion is presented, that allows to determine whether the electron system can be treated with thermodynamical equations like the TTM. Furthermore, it is demonstrated how material parameters like the electron heat capacity, the electron diffusivity and the electron–phonon coupling can be extracted out of the MC output. Finally, the obtained material parameters and the MC output are used as initial conditions for a TTM calculation, from which the induced track radius is obtained. This radius is in good agreement with experimentally measured track radii for a similar system.

Zusammenfassung

In dieser Arbeit werden Bestrahlungseffekte von schweren schnellen Ionen in Materie untersucht. Das Augenmerk liegt auf den Ladungaustausch– und Energieverlusstprozessen des Projektils.

Ein oft verwendeter Computercode, welcher Ratengleichungen verwendet, ist der sogenannte ETACHA Code. Dieser Computercode ist ebenfalls in der Lage die als Input benötigten Wirkungsquerschnitte zu berechnen. In dieser Arbeit wird ein neues Model zu Berechnung von Ladungszuständen schwerer schneller Ionen untersucht. Dieses Model, die Matrixmethode, nimmt die Form eines einfachen algebraischen Ausdrucks an, welches ebenfalls Wirkungsquerschnitte als Input voraussetzt. In der gegenwärtigen Implementierung der Matrixmethode werden Wirkungsquerschnitte aus dem ETACHA Code verwendet, wobei Anregung und Abregung vernachlässigt werden.

Ladungsfraktionen werden sowohl mit dem ETACHA Code als auch mit der Matrixmethode Ufer ausgewählte Ionen/target Kombinationen berechnet und miteinander verglichen. Für ausreichend hohe Energien ist die Übereinstimmung beider Modelle gut. Jedoch werden ausgeprägte Unterschiede für kleinere Energien sichtbar. Diese Unterschiede rühren daher, dass innerhalb der gegenwärtigen Implementierung der Matrixmethode keine Anregungen und Abregungen berücksichtigt werden. Beide Methoden werden anschließend mit experimentell gemessen Ladungfraktionen verglichen. Hierbei zeigen beide Modelle deutliche Abweichungen von den Experimenten. Während die vorhergesagte Gleichgewichtsladung von beiden Modellen in guter Übereinstimmung mit dem Experiment ist, zeigt die Matrixmethode eine deutliche Überschätzung der Gleichgewichts Eindringtiefe. Auch hier wird angenommen, dass dieser Unterschied durch die Vernachlässigung der Anregungs– und Abregungsprozesse herrührt. Eine Möglichkeit Abregungsprozesse zu berücksichtigen ist vorgestellt.

Es ist bekannt, dass die Bestrahlung von Dielektrika mit schweren schnellen Ionen zu strukturellen Veränderungen sowohl auf der Oberfläche als auch im Volumen führen, so genannte Ionen Spuren. Zu Beschreibung dieser Spuren wird häufig das so genannte zwei Temperaturen Modell (TTM) verwendet. Dieses TTM basiert auf zwei gekoppelten Wärmediffusionsgleichungen, welche den Wärmetransport der Elektronen als auch der Phononen beschreiben. Beide Gleichungen werden durch einen Austauschparamter, der so genannten Elektron–Phonon Kopplung, miteinander gekoppelt. Für die Anwendung des TTM werden Materialparameter wie z.B. die Dichte (der angeregten) Elektronen, die Wärmekapazität der Elektronen und die Elektron–Phonon Kopplung verwendet. Diese Parameter sind, besonders für Halbleiter und Isolatoren, oft nicht bekannt. In dieser Arbeit wird das TTM auf die Bestrahlung von kristallinem Silizium angewendet, um den so genannten Schwellenwert, d.h. die minimal nötige Energie um Strukturveränderungen hervorzurufen, zu berechnen. Es ist gezeigt, dass ohne die nötigen Kenntnisse der Materialparameter, dieser Schwellenwert nur mit einer grossen Unsicherheit bestimmt werden kann. Monte Carlo (MC) Simulationen für die Bestrahlung von SiO_2 mit 11.4 MeV/u Ca^{19+} werden vorgestellt. Mit Hilfe dieser MC Simulation wird die Elektronendichte sowie die Energiedichte berechnet, woraus sich wiederum die Elektronentemperatur sowie das Transportverhalten der Elektronen abschätzen lässt. Es wird ein Kriterium vorgestellt, mit welchem es möglich ist zu bestimmen, ob das Elektronensystem mittels thermodynamischen Gleichungen wie dem TTM beschrieben werden kann. Weiterhin werden die benötigten Materialparameter aus den MC Daten extrahiert und in einem TTM verwendet um den Radius der Modifikation zu bestimmen. Dieser Radius ist in guter Übereinstimmung mit experimentell gemessenen Radien für ein ähnliches System.

Contents

1 Introduction

The research field of ion beam physics dates back more than a hundred years. Electron beams and beams of positive ions were discovered by Thomson in 1897 [1] and Goldstein in 1902, followed by a strong activity on how to control and manipulate such beams. In 1911 the analysis of Rutherford led to the understanding that matter is constructed out of heavy positively charged atomic cores with the same amount of light negatively charged electrons [2].

Following this experiment and its findings, many papers on the penetration of particles in matter appeared, based on classical mechanics and the concept of the scattering cross section. Later on, relativistic extensions were included, which ultimately led to the incorporation of quantum mechanical concepts and the idea of a statistical treatment. Niels Bohr improved the Rutherford atomic model in 1913 by incorporating the quantal behavior of the electron [3].

With the discovery of the neutron by James Chadwick in 1932 it was suggested that the chemical element can be changed with the injection of a neutron [4]. In the same year John Cockroft and Ernest Walton irradiated Lithium with high energetic protons and accomplished the transmutation into helium (^{7}Li + p $\rightarrow$ ^{4}He + ^{4}He + 17.35 MeV) using an accelerator *(Cockcroft–Walton–accelerator)* [5]. This led to a constant improvement of high energy particle accelerators and detection tools like photographic plates, the bubble and later on the cloud chamber.

Yet another major break–through was in 1938 when Lise Meitner, Fritz Straßmann and Otto Hahn successfully demonstrated nuclear fission [6]. Under supervision of Enrico Fermi the first nuclear fission reactor, Chicago Pile 1, was constructed in 1942 [7].

The discovery of nuclear fission allowed for a much broader range of available particle energies and masses and was the main source for MeV ion beams until 1960, when it was replaced by van de Graaf generators. Since then, particle beams have been applied in a wide variety of fields, like material–modification and material–analysis or biophysics.

Ion beams play a large role in space science as well: Space crafts are constantly exposed to cosmic radiation such as α–particles, high energetic photons or electrons. This exposure may affect the equipment carried on a space craft leading to accidents or wrong measurements.

Low energetic ions are used within the Rutherford–backscattering (RBS) method to identify the chemical composition of a target. The depth resolution can easily be varied within six orders of magnitude depending on the energy and mass of the probing ion.

The classical scattering technique has been modified for instance by using ion–surface–scattering (ISS), where light keV ions are scattered from the target surface, or when photons are detected after being emitted due to the collisions (particle–induced X–ray emission, PIXE). Furthermore ejected target ions, so called secondary ions, may be studied, using the secondary ion mass spectroscopy (SIMS) or, in the case of neutral atoms, using the secondary neutral mass spectroscopy (SNMS) technique.

One special case is the so called accelerator mass spectrometry (AMS), where the sample is used as a sputter source. The sputtered target ions are then accelerated and mass separated within the accelerator. This allows for a very high mass sensitivity and single ion counting, so that for instance the ^{14}C percentage can be determined. This in turn determines the age of

the sample.

In the field of biophysics, swift heavy ion (SHI) beams are used, for instance in cancer therapy. The special properties of the SHI allows for a very selective energy deposition within the human body, thus destroying the tumor while the irradiation of the surrounding tissue is minimal.

Ion beams are also used for the modification of target material. In ion implantation experiments the projectile ions are implanted into a target material creating alloys or inducing defects. The target modification can be very precisely controlled, since the number of ions in the beam per area determines the number of implanted ions, while the beam energy controls the depth profile.

SHI irradiation of insulators has long been known to create macroscopic structural modifications both in bulk and surface. Such modifications, commonly called ion tracks, may appear as craters or hillocks on the surface, which are detectable, for instance by means of atomic force microscopy. Other more subtle modifications are color centers and changes in the chemical composition or binding of atoms. Such modifications can sometimes be detected by chemical etching of the surface. The damaged area, both bulk and surface, will exhibit a different etching rate compared to that of the virgin sample. Examples of swift heavy ion induced modifications are shown in figure 1.1.

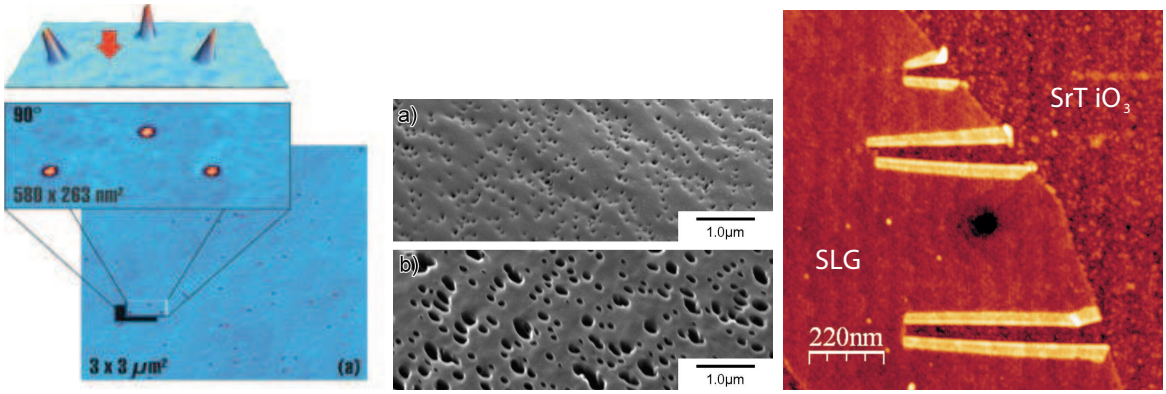

Figure 1.1: Left: Example of a surface modification, induced by a swift heavy ion in $SrTiO_3$. Middle: Scanning electron microscopy image of an ion–irradiated polycarbonate film after chemical etching with NaOH [8]. Right: Atomic force microscopy image of SHI irradiated graphene on $SrTiO_3$ [9].

Models, aimed at the understanding of these track creation phenomenon induced by SHI, first emerged in the mid 1960s, when Fleischer, Price and Walker introduced the idea of the so called *Coulomb explosion model*. This model arrived to explain the origin of the track formation in terms of a strong Coulomb repulsion experienced by the target atoms due to a removal of the target electrons by the penetrating ion beam. Therefore, the timescale of the coulomb explosion model is the time needed for the electrons to screen the atomic charges.

In the case of metals, the time until the atomic charges are screened by the electrons is on the order of some 10^{-15} s to some 10^{-14} s, which would require the atomic displacement to happen in that time period. Thus, it was believed that tracks can not be produced in metals. However, later tracks were also found in metals. In 1956, Kaganov, Lifshitz and Tanatorov

described the interaction of swift heavy ions with solids in terms of two heat diffusion equations, for the electrons and phonons individually, coupled by an exchange parameter, the so called electron–phonon coupling–parameter. Most notable was the derivation of the electron–phonon coupling based on the free electron model. Their derivation is still used today with only slight modifications.

Later, in 1974, Anisimov, Kapelovich and Perel'man applied the coupled heat diffusion equations to the irradiation of metals with a laser. In this text the term *two temperature system* was used, which later turned into the well known *two temperature model* (TTM). Around ten years later, the two temperature model was used again by Martynenko and Yavlinskii to describe ion solid interactions, where now the temperature dependence of the electron specific heat capacity and conductivity was accounted for. In the context of swift heavy ion beams, in the 1990s the two temperature model was often referred to as the *inelastic thermal spike* (I-TS) model. This terminology is still used today. The I-TS, as it is commonly used, employs thermodynamical quantities like the heat conductivity. This in turn makes it difficult to apply the model to insulators, where such quantities are missing, or in general to a system not well defined thermodynamically. Furthermore the I-TS often takes flak due to the fitting character of the calculations.

Many works have been published, where either the Coulomb explosion or the I-TS has been employed to explain the track creation, depending on the authors preferred model. But still even today the track creation process is not fully understood and both models are treated in a pitch-and-toss manner.

The description of the penetration of matter with swift heavy ions is a complicated task that requires the modeling of several different processes. In general these processes are

- Redistributions of the ions' charge due to charge exchange processes
- Excitation of the target electrons
- Transport of the excited electrons
- Creation of secondary electrons
- Creation of either permanent or transient structural modifications

Ion beams of some 100 MeV kinetic energy are usually created by using the fact that charged particles can be accelerated by electrical fields. Thus the ion source delivers an ion with a specific charge q, which is then given a certain kinetic energy and finally aimed towards a target. The ion beam might not be monochromatic, i.e. the ion beam might contain ions with different charges. The difference in the ion charge can affect the energy deposition within the target and thus the final outcome might be different from shot to shot. Even with a perfectly monochromatic ion beam the ion charge would fluctuate due to the fact that during the passage through the target the ion will capture target electrons or might be ionized or excited. The fluctuation in the mean charge will lead to a fluctuation of the mean energy loss. Such fluctuations will alter the energy depositioning in the target and therefore the spectrum of the exited electrons. The fluctuation in the mean energy loss, the so called *straggling*, is known to cause fluctuations in the mean total range of the projectile. This in turn could have a significant effect, *e.g.* in the aforementioned application of swift heavy ion beams in the field of cancer therapy. Therefore the knowledge of the ion charge state evolution during the passage through the target is necessary.

During the penetration, the ion excites target electrons. The excited electrons then travel through the target, spreading the primarily deposited energy. The transport of the electrons can be treated with different approaches, while the most notable difference is whether a continuum description like the two temperature model is used or a kinetic approach is employed, using Monte Carlo methods or the Boltzmann–Transport equation for instance.

While the electrons travel through the target, collisions with target atoms will result in the creation of ionized target atoms and thus in the creation of secondary electrons. These electrons then in turn lead to further ionization of atoms and thus to more "secondary" electrons. In the laser irradiation of dielectrics such electron cascades may lead to a "steady" increase of the electron density in the conduction band and may finally result in the so called dielectric–breakdown.

The electrons (both primarily and secondarily created) will transfer their energy to the target's atomic system, which may result in the local melting of the target. The observable permanent modifications of the target surface as well as of the target bulk can then be modeled using an atomistic description like a molecular dynamics simulation of the target atoms.

The aim of this thesis is to give a better understanding of the track creation process induced by swift heavy ions. The starting point will be the calculation of the charge exchange process of the ion during the penetration of a target media. After that the two temperature model is explained in detail, which serves as a basis to describe the electron–lattice interactions. The next chapter deals with a more sophisticated calculation of the electron dynamics using the Monte–Carlo method. It will then be demonstrated how target material parameters can be calculated using the MC data. The controversial issue of the definition of an electron temperature will be addressed. Finally, the coupling of the MC method to the TTM will be presented.

2 General considerations

In general, particle penetration through matter is a statistical phenomenon in the sense that two particles, well separated in time, will never undergo the same collisional events. However, these two particles are connected by an underlying statistical distribution. This chapter serves as the backbone of the theoretical considerations of the charged particle penetration through matter and is adapted from [10].

2.1 Cross section

The term "cross section" is of fundamental importance in the theory of particle penetration. Simply put, the cross section of a target is the area in which a bullet may hit it, thus a dartboard with a radius a presents a cross section of πa^2 to the dart arrow. In this macroscopic idea of a cross section it is obvious that the larger the cross section of the target is, the more probable it is to hit it. However, one still has to define what "to hit" actually means. In the case of the dartboard it is easy do define whether the arrow has hit the board (arrow stuck in) or not. However, one may argue that the probability of the arrow to be stuck in the board depends on the brand (thus on the quality) of the arrow or board. This is even more pronounced in the case of a microscopical particle, like an atom, as the determination of whether the projectile has actually hit the target depends on the fact that this has to have a measurable effect. This in turn means, that the magnitude of the cross section depends on the specific projectile, the specific target and on the specific physical effect that is measured. Therefore one speaks of specific types of cross sections like *energy loss* cross section, *ionization* cross section, *capture* cross section or *scattering* cross section *etc.*

To define a cross section one can assume a beam of projectiles, spread over a target with an area A, a density N (number of atoms per volume) and thickness x. A beam with a low current J is assumed, so that the projectiles interact with the target medium, but not with each other. Then the mean number of events per time for a certain process i is given as

$$v_i = JANx\sigma_i \ , \tag{2.1}$$

where σ_i is the corresponding cross section for the process i. Assuming further that the target is thin or the target density is low, the probability P_i of one projectile to undergo an event i is

$$P_i = Nx\sigma_i \ , \tag{2.2}$$

implying that $Nx\sigma_i \ll 1$.

2.2 Poisson formula

The projectile will undergo many collisional events during the passage through the target. To determine the probability $P_i^{(n)}$, that the projectile will experience n times the event i, the

Poisson formula can be used

$$P_i^{(n)} = \frac{(NV)^n}{n!} e^{-NV} \ , \tag{2.3}$$

where $V = \sigma_i x$ is the volume of a cylinder with a radius σ_i around the trajectory x of the projectile and n is a positive integer. The main assumptions are that the target atoms are uncorrelated and that V is small compared to the total volume. The Poisson distribution is normalized, so that

$$\sum_n^\infty P_i^{(n)} = 1 \ , \tag{2.4}$$

and the average

$$\langle n_i \rangle = \sum_n^\infty n P_i^{(n)} = NV \ . \tag{2.5}$$

Therefore the average number of the occurrence of events i is given by

$$\langle n_i \rangle = Nx\sigma_i \ . \tag{2.6}$$

Finally, the mean square fluctuation or the variance is given as

$$\langle (n_i - \langle n_i \rangle)^2 \rangle = Nx\sigma_i \ . \tag{2.7}$$

2.3 Energy loss

During its passage through matter a charged projectile may loose a part of its kinetic energy. Assuming that the projectile looses its energy in discrete portions T_i while moving through a target with thickness Δx, the energy loss ΔE is given by

$$\Delta E = \sum_i n_i T_i \ , \tag{2.8}$$

where n_i is the number of events i with the corresponding energy loss T_i. To find the average energy loss $\langle \Delta E \rangle$, the Poisson statistic can be applied

$$\langle \Delta E \rangle = \sum_i \langle n_i \rangle T_i \ . \tag{2.9}$$

The average number of events is given according to eq. (2.6)

$$\langle n_i \rangle = N \Delta x \sigma_i \ , \tag{2.10}$$

and thus

$$\langle \Delta E \rangle = N \Delta x \sum_i T_i \sigma_i \ . \tag{2.11}$$

The quantity σ_i here can be called an *energy–loss cross section* and

$$S = \sum_i T_i \sigma_i \tag{2.12}$$

is called the *stopping cross section*. The (mean) energy loss per unit pathlength

$$\frac{\langle \Delta E \rangle}{\Delta x} = N \sum_i T_i \sigma_i = NS \tag{2.13}$$

is called the stopping power.

2.4 Energy loss straggling

The mean square fluctuation of the energy loss is called the energy loss straggling Ω^2,

$$\Omega^2 = \langle \Delta E - \langle \Delta E \rangle^2 \rangle \ , \tag{2.14}$$

and according to eqs. (2.8) and (2.9), Ω^2 can be written as

$$\Omega^2 = \langle (\Delta E - \langle \Delta E \rangle)^2 \rangle = \sum_{i,j} \langle (n_i - \langle n_i \rangle)(n_j - \langle n_j \rangle) \rangle T_i T_j \ . \tag{2.15}$$

Separation between the terms with $i = j$ and $i \neq j$ leads to

$$\langle (n_i - \langle n_i \rangle)^2 \rangle \underset{\text{eq. (2.7)}}{=} N \Delta x \sigma_i \quad , \quad i = j \tag{2.16}$$

$$\langle (n_i - \langle n_i \rangle)(n_j - \langle n_j \rangle) \rangle \quad = \quad \langle (n_i - \langle n_i \rangle) \rangle \cdot \langle (n_j - \langle n_j \rangle) \rangle \quad , \quad i \neq j \tag{2.17}$$

The latter is zero, since[1] $\langle (n_i - \langle n_i \rangle) \rangle = 0$. Therefore the energy loss straggling reads

$$\Omega^2 = \sum_i \langle n_i \rangle T_i^2 = N \Delta x \sum_i T_i \sigma_i \ . \tag{2.18}$$

With a similar definition to that of the stopping cross section eq. (2.12) we define

$$W = \sum_i T_i^2 \sigma_i \ , \tag{2.19}$$

as the so–called straggling parameter.

2.5 Total pathlength

The loss of energy results in a slowing down of the projectile; consequently the projectile has a finite range in matter. From the Wilson chamber experiment [11] it is obvious that the energy loss fluctuation is small compared to the total energy of the projectile (see figure 2.1), therefore $E(x)$ is well defined at every point x. Therefore (2.13) can be written as

$$\frac{\mathrm{d}E}{\mathrm{d}x} = -NS(E) \ , \tag{2.20}$$

where the minus sign enters since an energy loss is considered here and is called the *continuous–slowing–down approximation*. The solution of this differential equation is given as[2]

$$x = \int_{E(x)}^{E(0)} \frac{\mathrm{d}E'}{NS(E')} \ , \tag{2.21}$$

here $E(x)$ is the initial energy of the projectile. By setting $E(x) = 0$, the total pathlength of the ion, i.e. the travelled pathlength after which the ion has lost all of its kinetic energy, can be calculated. This derivation of the total pathlength does not take into account any statistical fluctuations.

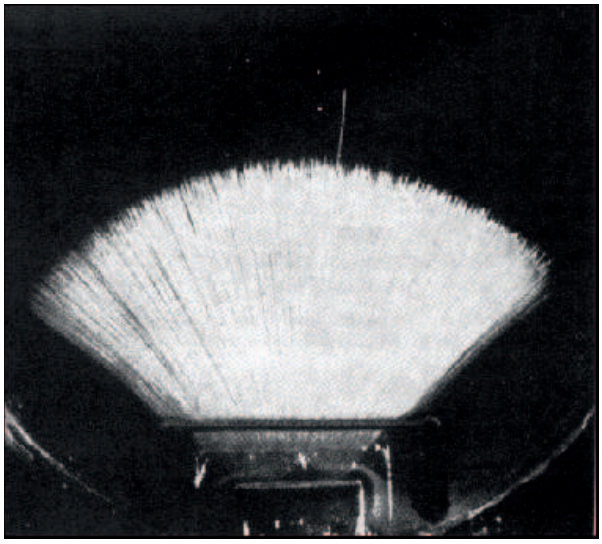

Figure 2.1: Tracks of α–particles in a Wilson chamber. Picture taken from [11].

2.6 Bothe–Landau formalism

In this section an approach based on a probability distribution will be presented.
Be $F(\Delta E, x)\mathrm{d}\Delta E$ the probability distribution for the energy loss ΔE of a particle traversing through a target with a thickness of x. The penetrated target can be build up as a sequence of layers with thickness y and x, so that the total thickness is $x+y$. The energy loss experienced by a penetrating particle with an initial energy E in the y–layer is $\Delta E'$, while the energy loss in the x–layer is $\Delta E - \Delta E'$ (see figure 2.2). The processes in both layers are statistically independent from each other. The joint probability distribution $F(\Delta E, x+y)$ is given by the Chapman–Kolmogorov equation [12]

$$F(\Delta E, x+y) = \int_0^{\Delta E} \mathrm{d}\Delta E' F(\Delta E', y) F(\Delta E - \Delta E', x) \ . \tag{2.22}$$

In Fourier space[3],

$$F(\Delta E, x) = \frac{1}{2\pi} \int_{-\infty}^{\infty} \mathrm{d}k \ e^{ik\Delta E} F(k, x) \tag{2.23}$$

the convolution can be written as

$$F(k, x+y) = F(k, y) F(k, x) \tag{2.24}$$

and its solution

$$F(k, x) = e^{xC(k)} \ , \tag{2.25}$$

where $C(k)$ is an unknown function, which depends on the processes occurring during the penetration. Employing again the small target thickness limit, the probability distribution

[1] $\langle (n_i - \langle n_i \rangle) \rangle = \langle n_i \rangle - \langle \langle n_i \rangle \rangle = \langle n_i \rangle - \langle n_i \rangle = 0$
[2] The minus sign is compensated by switching the integral boundaries.
[3] The introduced variable k is here treated as a so–called *nuisance* variable, i.e. the variable k is of no direct interest.

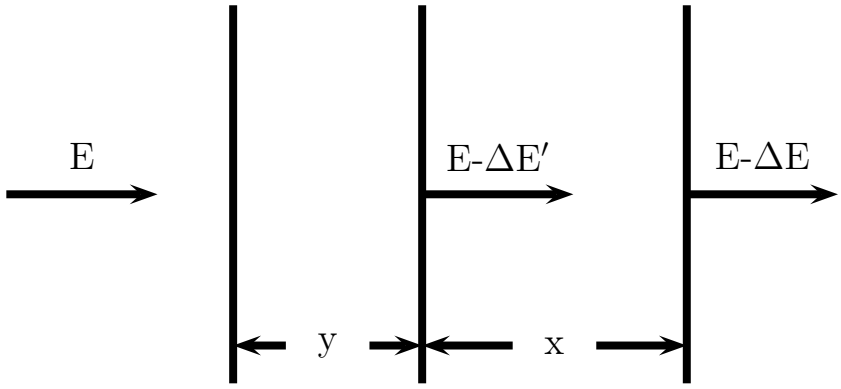

Figure 2.2: The energy loss in a target composed of a succession of two layers y and x.

can be written as

$$F(\Delta E, x) = (1 - \sum_i P_i)\delta(\Delta E) + \sum_i P_i \delta\left(\Delta E - T_i\right) \quad , \quad x \text{ small}, \tag{2.26}$$

where δ is the Dirac delta function. The first term in eq. (2.26) represents the probability that no event with zero energy loss happens. The second term represents the possibility that one event with the corresponding energy loss happens. Rewriting eq. (2.26) in Fourier space and utilizing eq. (2.2) leads to,

$$F(k, x) = 1 - \sum_i N x \sigma_i (1 - e^{-ikT_i}) \quad , \quad x \text{ small}. \tag{2.27}$$

From the comparison between eq. (2.27) and eq. (2.25) with the limit of small x the function $C(k)$ can be obtained[4]

$$\begin{aligned} C(k) &= -N \sum_i \sigma_i (1 - e^{-ikT_i}) \ , \\ \sigma(k) &\equiv \sum_i \sigma_i (1 - e^{-ikT_i}) \ , \end{aligned} \tag{2.28}$$

where $\sigma(k)$ is the so called transport cross section. Substituting eqs. (2.25) and (2.28) in eq. (2.23), yields the so–called *Bothe–Landau equation*

$$F(\Delta E, x) = \frac{1}{2\pi} \int_{-\infty}^{\infty} \mathrm{d}k \ e^{ik\Delta E - Nx\sigma(k)} \ . \tag{2.29}$$

[4]With the limit of small x eq. (2.25) reads: $F(k, x) = 1 + xC(k), \ldots$.

From this point on it is convenient to calculate the fluctuations of the energy with the help of the probability distribution. Multiplication of eq. (2.29) by the n–th moment of the energy and integration gives

$$\int_{-\infty}^{\infty} \mathrm{d}\Delta E \Delta E^n F(\Delta E, x) = \left(i \frac{\partial}{\partial k} \right)^n e^{-Nx\sigma(k)}|_{k=0} \tag{2.30}$$

where $n = 0, 1, 2....$

For $n = 0$ particle conservation is given by,

$$\int \mathrm{d}\Delta E F(\Delta E, x) = 1 \ , \tag{2.31}$$

while the first moment expresses the mean energy loss

$$\langle \Delta E \rangle = -iNx \frac{\mathrm{d}\sigma(k)}{\mathrm{d}k}|_{k=0} = Nx \sum_i T_i \sigma_i = NxS \ . \tag{2.32}$$

According to eq. (2.14), the second moment minus the square of eq. (2.32) then gives the energy loss straggling

$$\begin{aligned} \Omega^2 &= \overline{(\Delta E - \langle \Delta E \rangle)^2} \\ &= Nx \frac{\mathrm{d}^2\sigma(k)}{\mathrm{d}k^2}|_{k=0} - \left(Nx \frac{\mathrm{d}\sigma(k)}{\mathrm{d}k} \right)^2 |_{k=0} - \left(iNx \frac{\mathrm{d}\sigma(k)}{\mathrm{d}k} \right)^2 |_{k=0} \\ &= Nx \sum_i T_i^2 \sigma_i = NxW \ . \end{aligned} \tag{2.33}$$

In the same way higher order moments can be calculated; however, these moments have no physical meaning.

3 Charge exchange

In this section, the concept of charge exchange and the physical background as well as the processes leading to charge exchange will be introduced. Three different methods to compute the charge fraction of ions in matter will be presented. The main focus will be the implementation of an algebraic method, the so called matrix method. This is followed by the introduction of the ETACHA code, an implementation based on rate equations, which is often used to compute charge fractions. The input required for the matrix method are cross–sections of the charge changing processes. In the present implementation these cross–sections are taken from the input parameters of the ETACHA code, thus a direct comparison of the calculated charge fractions by the matrix method with the ETACHA results will be given. Both methods are then compared with experimental measurements of charge states. Finally the complexity of cross–section calculations will be addressed and scaling rules, based on empirical formulas, will be presented. This is followed by the conclusions. Results of the studies presented here have been published in [13, 14].

3.1 Introduction

During the passage through a target medium, charged particles undergo collisions which result in a loss of the particle's energy. The mean of this energy loss defines the projectiles range (see eq. (2.21) in sec. 2.5). Fluctuations of the mean energy loss will therefore result in fluctuations of the total range.

It was suggested almost a hundred years ago by Flamm and Schumann that the range of alpha particles in a target may be affected by charge–exchange processes [15]. Experimentally this was demonstrated in 1922 by Henderson [16]. Furthermore, Henderson showed that the stopping power of a singly charged helium ion differed from that of an alpha particle at the same energy. Two years later Rutherford measured the electron capture and loss rates of an alpha particle passing trough matter [17]. He concluded that the alpha particle suffered more than a thousand collisions accompanied by charge exchange. In 1948 Bohr noted that the energy transfer due to charge exchange may not be small and should therefore be considered [18].

3.2 Basics

During the penetration of a target medium with a given atomic density N, the ion starting with a charge q may undergo a series of charge changing events $q \rightarrow q' \rightarrow q''$ and may then exit the target with a charge q_{out} after a certain travelled pathlength x. This is schematically shown in fig. 3.1. Assuming now a beam of ions, each initially with a charge q, it is obvious that the ion beam will exhibit a distribution of ion charges, so called charge fractions $F_{ij}(x)$, which depends on the travelled pathlength x. Here i is the initial and j the final state. Experimentally, these charge fractions may be determined by using thin foils of different thicknesses and measuring

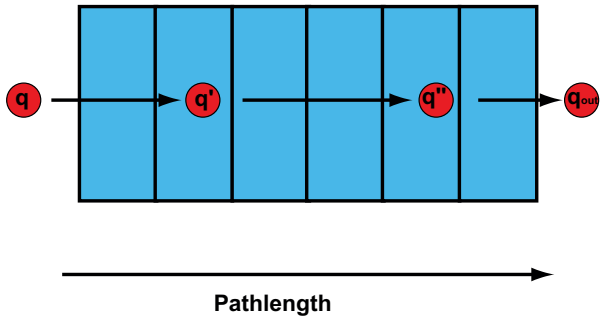

Figure 3.1: Schematic drawing of an ion with charge q penetrating a target medium, changing its charge due to collisions and exiting the target with a charge q_{out}.

the charge of the exiting ions. For large pathlengths the ion beam will reach an equilibrium in the charge fractions. At this equilibrium pathlength X_{eq} the charge fractions no longer depend on the initial charge,

$$F_{ij} \rightarrow F_j \quad , \quad x > X_{eq}. \tag{3.1}$$

From a theoretical point of view, analytic expressions to calculate charge exchange for systems with up to three states exist [19], but are hardly useful nowadays.

In principal there are three methods to compute the charge exchange evolution

- Rate equations [19–22]
- Monte–Carlo method [23]
- Matrix method [24, 25]

The three methods are equivalent from a physical point of view and they share the same needed input in the form of cross–sections. However, there are significant differences concerning the numerical implementation and the ability to handle a system with a large number of involved states.

In terms of the rate equations the charge fraction $F_i(x)$ of ions being in the state i is computed by

$$\frac{\mathrm{d}F_i(x)}{\mathrm{d}x} = \sum_{ij} F_i(x)\sigma_{ij} - F_i(x)\sum_i \sigma_{ij} \ , \tag{3.2}$$

where σ_{ij} is a transition cross–section. In this approach one rate equation is written down for every available projectile state i. It is evident that this calculation is a backtracking method, *i.e.* to calculate the charge fraction at the point x, the charge fraction at the previous point x' has to be known. This implies that the accuracy of the result is not only determined by the cross–section σ_{ij} but also by the applied numerical method.

Within the Monte–Carlo method each ion is followed individually. Using a random number generator it is determined whether a charge changing collision takes place or not. This "decision" is then repeated for the desired pathlength of the projectiles. Then the entire process for the entire pathlength is repeated many times, so that statistical fluctuations become small. Therefore, the Monte–Carlo method is very time consuming both for large pathlengths as well as for a system with many states.

The matrix method takes the form of a compact algebraic solution and will be discussed in detail in a following section. The main advantages of the matrix method are its simple form and the fact that no backtracking is nessecary, *i.e.* the charge fractions $\mathbf{F}(\mathbf{x})$ can be computed at any desired pathlength x, without the need to know the charge fraction at previous pathlengths.

3.3 Charge changing processes

As was stated in section 2.1, the term cross–section needs to be specified. Therefore a brief overview of the charge changing processes and thus the related cross-section will be given here. During the penetration, the ion can capture an electron from the target or lose an electron due to ionization, leading to a change of the ion charge. The ion may also be excited and the excited electron may decay again, which may or may not preserve the charge during that process. These processes are shown in figure 3.2 for an atom with three atomic orbitals, 1s, 2s and 2p. The blue arrows indicate the capture of an electron into the different atomic orbitals 1s, 2s, 2p *etc.*. The red arrows indicate the ionization of the projectile, *i.e.* the loss of an electron from an atomic orbital. The green arrows indicate the excitation/deexcitation of a projectile electron. The electron may be initially in the 1s orbital and may be excited, for instance into the 2s orbital. This is shown by the arrows pointing upwards. Downward arrows indicate an deexcitation of an electron, for instance from the 2p into the 2s orbital. The purple arrows indicate Auger processes. One electron in the 2p orbital is deexcited into the 1s orbital, while the excess energy is transferred into an electron in the 2p orbital, which then may be ionized.

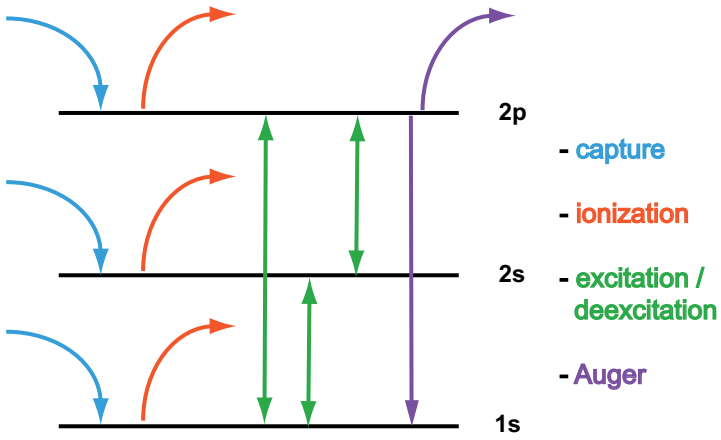

Figure 3.2: Schematic drawing of the charge changing processes. The blue arrows indicate the capture of an electron. The red arrows indicate the ionization of the projectile, *i.e.* the loss of an electron from an atomic orbital. The green arrows indicate the excitation/deexcitation of a projectile electron. The purple arrows indicate Auger processes.

3.4 The matrix method

In this section, the matrix method will be derived based on [24, 25].

The charge changing processes suffered by the projectile during the passage through the target can be divided into instantaneous (capture, loss and excitation) and delayed processes (Auger cascades and deexcitation). In the following considerations, two assumptions will be made:

1. Only instantaneous processes will be considered.

2. The energy loss is assumed to be small, so that the projectile's velocity is constant.

The penetrating projectile can be in any initial state $i = 0, 1, 2 \ldots$ and a corresponding final state j. The transition from state i to state j during a (instantaneous) collision at a given penetrated thickness x is governed by the cross–section σ_{ij} and the corresponding probability by $F_{ij}(x)$.

The joined probability for a convolution of two targets with thickness x and y is then similar[1] to eq. (2.24)

$$F_{ij}(x+y) = \sum_k F_{ik}(x) F_{kj}(y) \quad , \tag{3.3}$$

introducing the matrix notation $\mathbf{F}(x) = ||F_{ij}||$ this reads

$$\mathbf{F}(x+y) = \mathbf{F}(x)\mathbf{F}(y) \quad . \tag{3.4}$$

The solution of this matrix equation is given by

$$\mathbf{F}(x) = e^{x\mathbf{Q}} \quad , \tag{3.5}$$

with an unknown matrix $\mathbf{Q}$. Following then the general scheme outlined in section 2.6 to determine the matrix $\mathbf{Q}$, assuming a thin layer, so that only one collision takes place

$$F_{ij}(x) = \left(1 - Nx \sum_k \sigma_{ik}\right) \delta_{ij} + Nx\sigma_{ij} \quad , \quad x \text{ small}, \tag{3.6}$$

where δ_{ij} is a Kronecker symbol and N is again the target atomic density. Here the first term gives the projectile's probability to remain in the state i, while the second term is the probability for a transition from the state i to state j.

Comparing this with eq. (3.5) in the limit of small x, the matrix $\mathbf{Q}$ is determined as,

$$Q_{ij} = N\left(\sigma_{ij} - \delta_{ij} \sum_k \sigma_{ik}\right). \tag{3.7}$$

Assumption 2 is a more technical consideration, allowing to assume that the cross–sections σ_{ij} and since eq. (3.7) also the $\mathbf{Q}$ matrix remain constant during the penetration. By dividing the target into layers according to (3.4), each fulfilling assumption 2, one can account for the ion's energy loss and thus a change in the cross–sections.

Assumption 1, however, means that no time evolution is considered within this approach, therefore no Auger decays are included. A possible way to include the Auger decay is presented in section 3.7.3. Additionally it should be noted here that no excited states are included in this implementation of the matrix method.

[1] The energy loss ΔE in eq. (2.24) is omitted here, as $\Delta E = 0$ is assumed later on.

3.4.1 Numerical implementation

Computation of the exponential of a matrix is a delicate task. A overview of different methods is given in [26]. In this work the exponential has been computed by operating with a truncated exponential series

$$\exp(NxQ) = \sum_{n=0}^{n_{\max}} \frac{(NxQ)^n}{n!} \quad . \tag{3.8}$$

A computer program has been written that accepts cross–sections as input, then constructs the **Q** matrix according to eq. (3.7) and generates the charge fractions as output. Numerical stability is tested by checking, if the sum rule $\sum_j F_{ij} = 1$ is fulfilled at every point x and if asymptotic charge fractions were independent of the initial ion charge. Convergence is monitored at every step for every element $F_{ij}(x)$. To limit round–of errors, the calculations are performed using double precision.

Another method to compute the exponential of a matrix is to solve the ordinary differential equation (ODE) belonging to the solution given by eq. (3.5). The ODE was solved using a GSL ODE solver [27] and compared with the numerical implementation of eq. (3.8). No significant differences in the entire x interval are observed, if convergence is reached by eq. (3.8). Calculation times for eq. (3.8) range from "instantaneous" to some minutes, depending on the number of states involved. The stability of the solution was tested by calculating a system with 100 states and schematic input cross sections.

One of the main advantages of the matrix method is, that charge fractions $\mathbf{F}(x)$ can be calculated for any given thickness x without having to compute previous thicknesses, also avoiding pile–up errors. It will be shown later that eq. (3.8) leads to severe convergence problems for large pathlengths. This problem can be solved by dividing the penetrated layer according to eq. (3.4).

3.4.2 Two charge states

In this section an example of a charge state evolution will be given for the case of an ion with only two accessible projectile states. The calculation has been performed using arbitrary cross–sections. The charge fractions will be called $F_{00}, F_{01}, F_{10}, F_{11}$, meaning that F_{00} represents the transition $0 \to 0$, *i.e.* that the ion beam is in state 0 and stays in state 0. Consequently F_{01} is the transition from state 0 to state 1. The numbering of the states is not unambiguous: what exactly is the meaning of "state 0"? From here on the state will represent the ion's charge, thus "state 0" is the neutral atom, while "state 1" represents a single positively charged ion, etc. Here a perfectly monochromatic hydrogen ion beam is assumed, where all ions are initially prepared to have charge 0. Each individual hydrogen ion (or atom in that case) has a cross–section to lose its electron during a collision with a target atom. According to this setup the initial charge fractions are: $F_{00}(x = 0) = 100\%$ and $F_{01}(x = 0) = 0\%$.

Throughout the penetration the "hydrogen beam will lose electrons" (negatively charged hydrogen is not allowed here), so that F_{00} will drop and consequently F_{01} will increase by exactly that amount. Finally, after the equilibrium depth, the charge fractions reach their asymptotic value.

However, one can reverse the situation by initially replacing all the hydrogen atoms in the beam with positively charged hydrogen ions. Then the initial charge fractions are: $F_{11}(x = 0) = 100\%$ and $F_{10}(x = 0) = 0\%$. Obviously the charge evolution is now set in a way that the "hydrogen beam will capture electrons" (there is no electron to lose), so that F_{11} will drop

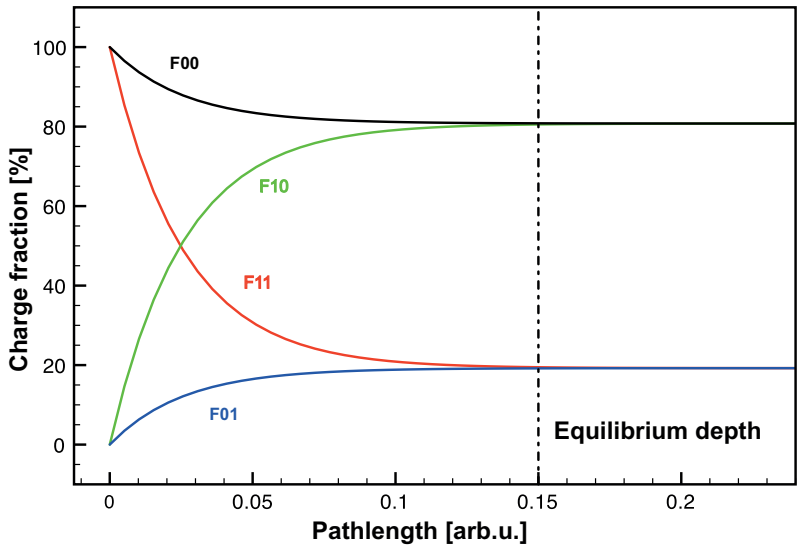

Figure 3.3: Charge fractions F_{ij} versus pathlength x for an ion with only two accessible projectile states.

and consequently F_{10} will increase by exactly the same amount. Finally, after the equilibrium depth the charge fractions reach their asymptotic value.

Both gedankenexperiments are shown in fig. 3.3. Obviously $F_{00} = F_{10}$ as well as $F_{11} = F_{01}$ for large x, as it should be according to eq. (3.1).

This is another major advantage of the matrix method: both gedankenexperiments are calculated simultaneously. In the case of a two state problem this is trivial, but for the case of many states it becomes quite an advantage.

3.5 Computed charge fractions

In this section the computer code ETACHA will be introduced. This code serves as a reference for charge fractions calculated with the matrix method.

In the current implementation of the matrix method total cross–sections are used. The cross–sections are obtained, using the cross–sections calculated by the ETACHA code, in such a way, that all partial cross–sections referring to a pertinent charge–changing event are summed up. Thus the number of states included is equal to the number of charge states. Excitation and deexcitation as well as Auger decay of states are not included.

The calculated charge fractions using the matrix method are then compared with the ETACHA code. Finally both computer codes are compared with experimentally measured charge fractions.

3.5.1 ETACHA calculations

The computer code ETACHA, developed by Rozet *et al.* [22, 28], is based on rate equations to compute the charge fractions of ions. As input, ETACHA calculates state–specific so called

partial cross–sections. Within ETACHA, the eikonal approximation for non–radiative [29] and the Bethe–Salpeter formula for radiative capture [30] is used to calculate the capture cross–sections. The loss cross–sections are obtained using the plain–wave Born approximation. The cross sections are scaled according to the *independent electron approximation*. The cross–sections for capture and loss as well as the independent electron approximation are discussed in section 3.7. Excitation states up to $n = 4$, where n is the principal quantum number, are implemented. For the Auger decay tabulated data is used.

Due to the fact that the number of partial cross–sections used within ETACHA are limited, the charge fractions that can be calculated within the ETACHA code are limited to systems with up to 28 electrons. Furthermore, the authors of [22] state that the cross–sections calculated are only valid for ion energies greater than 1 MeV/u.

The code used was written in 1997 and is available at

http://www-linux.gsi.de/∼weick/charge_states/

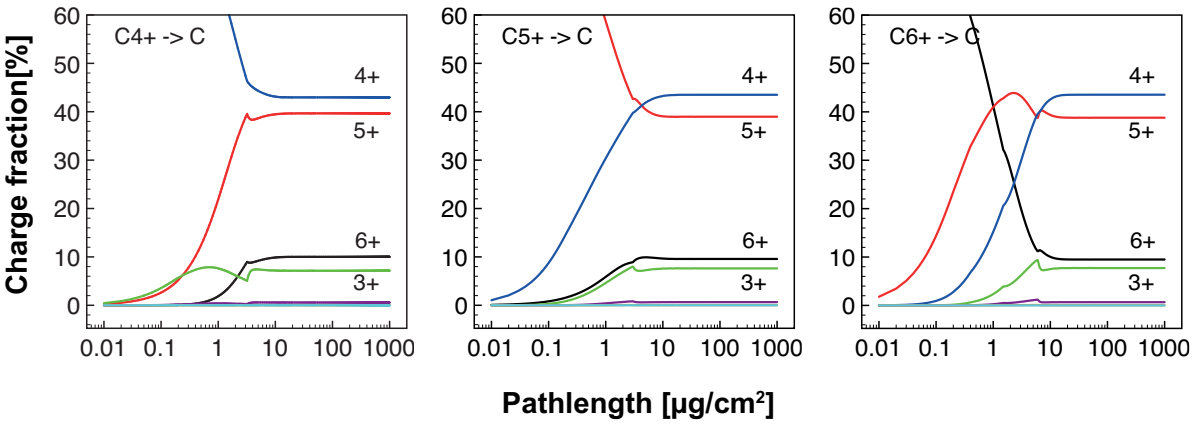

Figure 3.4: Calculated charge fractions for C in C @ 0.5 MeV/u using the ETACHA code.

The ETACHA code has been used to calculate the charge fractions for the case of 0.5 MeV/u carbon in carbon. As the incoming ions C^{6+}, C^{5+} and C^{4+} have been chosen. The results are shown in figure 3.4. From this figure kinks in the calculated charge fractions can be observed. These kinks are numerical artifacts due to numerical instabilities in the applied routine to integrate the rate equations. Increase of the numerical accuracy may minimize these artifacts for certain target–projectile–energy combinations, however, in the presented example this accuracy was set to the maximum value allowed by the program. In figure 3.4 one can also observe that the asymptotic value of the charge fractions is not independent of the initial charge state. For a better estimation of this effect, figure 3.5 shows the outgoing charge state C^{6+} for all incoming charges C^{1+} - C^{6+}. The asymptotic regime has been magnified. The ions' energy has been increased to 1 MeV/u. Evidently, the asymptotic charge fractions predicted by ETACHA depend on the incoming ion charge. For the case presented in figure 3.5, the variation in the asymptotic charge fraction is almost 5%. These deviations from the asymptotic behavior, the kinks in the charge fractions and sometimes even oscillatory behavior are only related to numerical instabilities in the applied algorithm and can be found throughout all target–projectile–energy combinations.

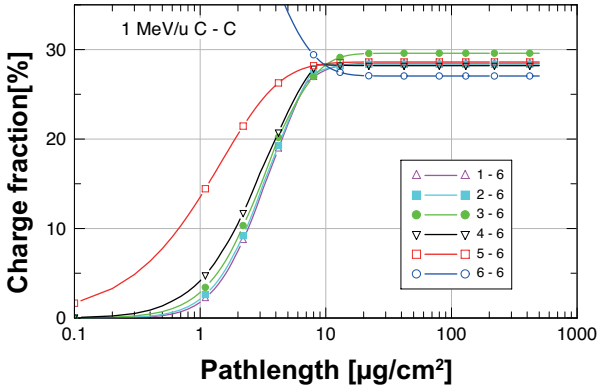

Figure 3.5: Charge fraction $F_{q6}(x)$ for C in C @ 1 MeV/u for incoming charges $q = 1 - 6$ and $q = 6$ outgoing state, calculated by ETACHA. The target density has here been set to 0.001 g/cm^3. Figure taken from [13].

3.5.2 Comparison of the matrix method with ETACHA

From a physical point of view, the rate equation approach implemented in the ETACHA code and the matrix method are equivalent. It should be noted here, that ETACHA is utilizing partial cross–sections, while the current implementation of the matrix method uses total cross–sections and in addition excitation/deexcitation states, and Auger decay is not included in the matrix method. Thus an exact equality between both methods can not be expected. Therefore, in this section the charge fractions obtained using the matrix method will be compared with those calculated by the ETACHA code. The comparison presented below should be understood as a qualitative comparison. As neither excitation/deexcitation nor Auger decay processes are included in the matrix method a quantitative agreement is not to be expected.

Calculations have been performed for the irradiation of carbon with carbon ions at 5 MeV/u, 2 MeV/u and 1 MeV/u.

The charge fractions for the case of 5 MeV/u carbon ions in carbon are shown in figure 3.6. Only incoming and outgoing charge states q= 4 - 6 are shown, since the equilibrium charge fractions for the outgoing charge states $q < 4$ are below 0.001 %. For a direct comparison, both the matrix method as well as the ETACHA calculations are shown. The incoming charge fractions are identified by colors while the outgoing charge fractions are given by symbols, *e.g.* the charge fraction F_{54} (the transition from C^{5+} to C^{4+}) is given by a red rectangular. The results of the matrix method calculation are given by the solid black lines.

For 5 MeV/u the agreement with ETACHA, both concerning the transient as well as the asymptotic behavior, is nearly perfect, despite the neglect of excitation and decay processes in the matrix calculations. Minor differences are found for the charge fractions $4+ \rightarrow 4+$ and $4+ \rightarrow 6+$. The calculations presented in figure 3.6 show that at 5 MeV/u the carbon ion is almost completely striped after a pathlength of around 30 μg/cm^2 or 0.12 μm, which is in agreement with the Thomas–Fermi estimate (see section 3.9) and the considerations by Bohr [20].

For the calculations shown in figure 3.7 the beam energy of the carbon ions is reduced to 2 MeV/u. As expected, the charge fractions exhibit a broader distribution with around 80 % of the ion beam constituting of bare carbon ions and 20 % C^{5+}. Again the agreement, both in the asymptotic as well as the transient behavior, is nearly perfect.

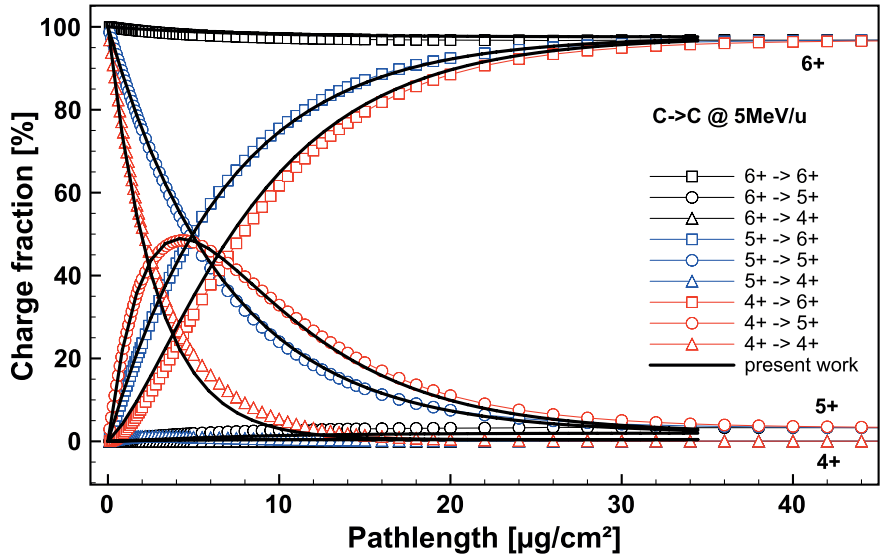

Figure 3.6: Calculated charge fractions for 5 MeV/u C^{q+} in C for $q = 4 - 6$ (identified by colors) and outgoing charges $q = 4 - 6$ (identified by symbols). Solid lines: matrix method. Points: ETACHA. Picture taken from [13].

For the next calculation the energy of the ion beam has been further reduced to 1 MeV/u as is shown in figure 3.8. At this energy the comparison with ETACHA shows more pronounced differences. The largest discrepancies are found for the charge fractions $5+ \rightarrow 6+$, $6+ \rightarrow 5+$ and $6+ \rightarrow 6+$. It is also observed that within the matrix method, the asymptotic charge fraction F_6 is underestimated while F_5 is overestimated compared to the ETACHA calculations. This indicates that the effective loss cross–section in charge equilibrium is underestimated within the matrix method.

In figure 3.8 differences in the asymptotic charge fractions calculated by ETACHA can be observed. These differences were already shown in figure 3.4, where the final charge state 6+ is shown in detail. Figure 3.8 demonstrates that this problem is completely avoided within the matrix method.

3.5.3 Convergence

The present implementation of the matrix method is based on a truncated series expansion eq. (3.8). Since only a finite number of series elements are included, this approach must lead to convergence problems for large pathlengths, *i.e.* large values of x. In the figures 3.6, 3.7 and 3.8 the asymptotic regime is reached before the expansion breaks down. However, in general this is not the case. In figure 3.9 the case of 2 MeV/u sulphur in carbon is shown. The calculations shown in the left figure demonstrate the breaking down of the series expansion. As is evident asymptotic charge fractions can not be extracted from that figure. However, it can also be observed that the instabilities start rather abruptly at some critical depth, which is common to all outgoing charges. This critical depth is around 180 $\mu g/cm^2$ for the case shown on the left side of figure 3.9. Therefore, this problem can easily be overcome by dividing the target into layers and applying eq. (3.4) for each layer. If necessary, this procedure can be repeated until the desired pathlength is reached. In figure 3.9 (right graph) both the unconvoluted (colored

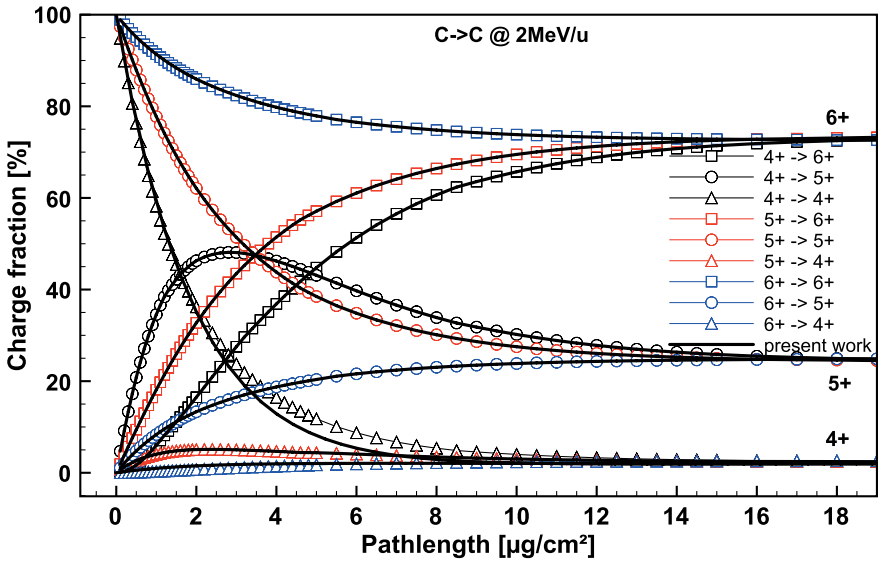

Figure 3.7: Calculated charge fractions for 2 MeV/u C^{q+} in C for $q = 4 - 6$ (identified by colors) and outgoing charges $q = 4 - 6$ (identified by symbols). Solid lines: matrix method. Points: ETACHA.

lines) and the convoluted (black lines) calculations are shown. The convolution is performed 4 times with layers of 150 μg/cm^2 thickness each, which eliminates the problem efficiently.

3.6 Comparison of the charge fractions with experiments

In this section the calculated charge fractions are compared with experimental measurements. The first comparison is the case of 2 MeV/u sulfur ions in carbon [31, 32]. In the original papers the measured charge fractions have been compared with the ETACHA code. The following results are therefore in principal a comparison between the two theoretical models as improved agreement cannot be expected, since both methods share the same input.

In figure 3.10 the charge fractions for 2 MeV/u S^{12+} in C are shown. Only the outgoing charge fractions 12 to 15 are shown. For these calculations, the carbon density is set to be 2 g/cm^3, to reflect the experimental conditions.

The largest discrepancy is found for the outgoing charge state $q = 10+$. For the charge fraction $q = 11+$ the rising edge at around 1 μg/cm^2 and the falling edge at 3 μg/cm^2 predicted by ETACHA are not reproduced by the matrix method calculation.

The fact that the high ionization states $q = 14+$ and $q = 15+$ are slightly overestimated while the charge fractions $q = 10-13$ are in general underestimated, is likely due to an underestimation of the loss cross–section caused by neglecting of excited states. This underestimation is in accordance with the Bohr–Lindhard model [20].

Next, the mean charges $\bar{q} = \sum_q qF_q$ for 2 MeV/u S $\rightarrow$ C for both the matrix method as well as ETACHA calculations are compared with experimental results [31, 32]. This is shown in figure 3.11. Again both methods exhibit well pronounced differences from the experiment concerning the behavior of the charge fractions far from equilibrium. For the matrix method, the largest difference can again be found for low charge states, which is again due to neglected

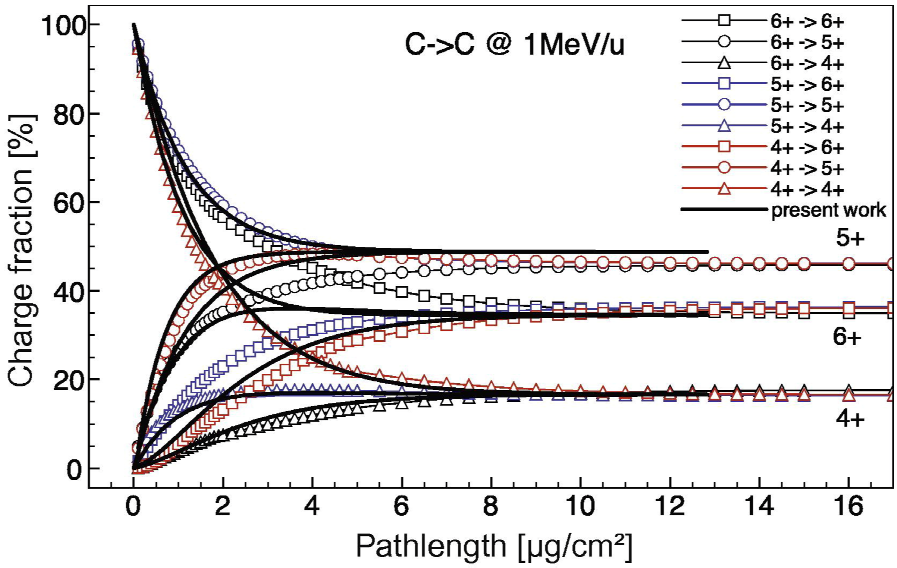

Figure 3.8: Calculated charge fractions for 1MeV/u C^{q+} in C for $q = 4-6$ (identified by colors) and outgoing charges $q = 4-6$ (identified by symbols). Solid lines: matrix method. Points: ETACHA. Picture taken from [13].

excited states. Furthermore Imai *et al.* [32] suggest that multiple-electron loss and capture processes may be significant in this context.

However, the most significant discrepancy both concerning the experimental data as well as the ETACHA calculation is that the equilibrium thickness is dramatically overestimated within the matrix method. This overestimation may be due to the fact that density effects like Auger decay are not yet included.

3.7 Cross Sections

In this section the cross–sections necessary[2] for the charge fraction calculations will be summarized. The matrix method as it is implemented is completely free of pile–up errors, the accuracy of the calculations is exclusively determined by the quality of the cross–sections. As stated above four types of cross–sections govern the charge exchange evolution. From the viewpoint of the ion these are:

- The cross–section to capture an electron from the target
- The cross–section to lose an electron
- The cross–section that an electron is captured/lost into/from an exited state
- The cross–section of Auger decay of electron states

The importance of capture and loss cross–sections is obvious. The role of excited states is not so clear. Considering an ion as a positive core with electrons orbiting it, excitation of an

[2]Again, it should be noted, that within the present implementation of the matrix method excitation/deexcitation cross–sections as well as Auger decay processes are not included.

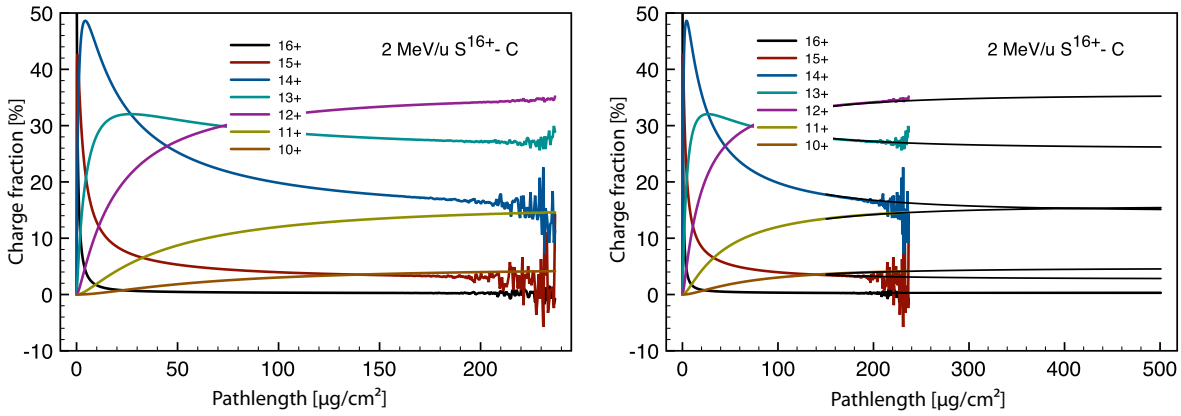

Figure 3.9: 2 MeV/u S^{16+} in C and outgoing charges $q = 10 - 16$, calculated by the matrix method. Left graph: Single-layer computation; right graph: Convolution of up to four layers, compared with the single-layer case. Pictures taken from [13].

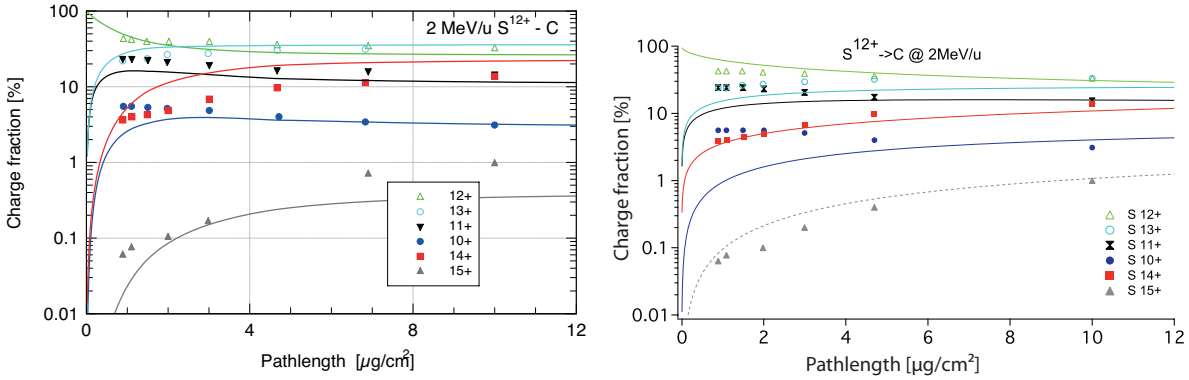

Figure 3.10: Charge fractions for 2 MeV/u S^{+12} in C. Left graph: Calculated with ETACHA (lines) and measurements by Imai *et al.* [31] (symbols). Right graph: Same system calculated with the matrix method (lines) and again measurements by Imai *et al.*. Both pictures are taken from [31][13].

electron means that the electron is located at a larger radius from the core. Consequently the binding of that electron to the ion is weaker, *i.e.* its ionization potential is lower. Therefore it is easier to remove an excited electron from the ion as compared to an electron in the ground state, the loss or ionization cross–section is higher for excited electrons. Thus excitations of ions lead to a higher "effective" electron loss cross– section. It is then obvious, that, if excited states are included, the deexcitation/decay of such states has also to be taken into account.

Due to this consideration of excited states one may think of a picture where the electrons are arranged according to their principal quantum number. Then the cross–sections are given with respect to the electron orbitals 1s, 2s, 2p ... and are called partial cross–sections. This is shown schematically in figure 3.2. However, this leads to a problem even in the simplest case of a hydrogen ion. The hydrogen may be neutral, but in which orbital is its electron located? Therefore one charge state will split up into an infinite number of possible states. The highest principal quantum number may be limited due to physical considerations to n_{max}, this means

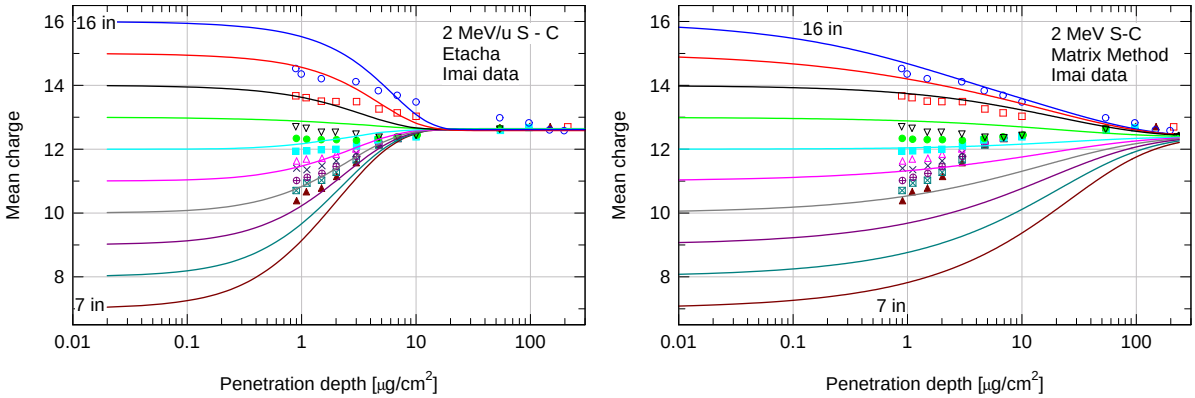

Figure 3.11: Mean charge for 2 MeV/u S^{q+} in C for different target thicknesses. Points: Measurements by Imai et al. [31, 32]. Solid lines: ETACHA (left graph); Matrix method (right graph). Picture taken from [13]

that the number of involved states in the two charge state case is $n_{max} \times 2$ for the 1s/2s state and $n_{max} \times 6$ for the 2p state, *etc.* This is obviously not a pleasant thought considering heavy ions like gold or uranium.

Furthermore these partial cross–sections also depend on the ion's current electron configuration. The capture into the 1s state for instance depends heavily on the question whether the state is unoccupied or if there is already an electron in that state. Therefore the so called independent electron approximation is often employed and also used within the ETACHA code. This approximation will be studied in section 3.7.4 in detail. Within that approximation the loss cross–section is proportional to the number of electrons in that state, while the capture cross–section is proportional to the number of vacancies in that state. In order to limit the number of exited states to be considered numerically, for instance the ETACHA code only takes 4 shells into account.

3.7.1 Loss and excitation cross–section

A nice overview on the topic of excitation and ionization cross–sections can be found in [33, 34], where the first work is a more experimental approach while the latter is a theoretical paper.

The loss of an electron can be calculated using any theory that can handle the ionization of an ion. This could be for instance Binary theory like it is implemented in the PASS code [35, 36]. Another method is the calculation using the plain–wave Born approximation as it is used within the ETACHA for instance.

Excitation cross–section can in principle be calculated using the same method as is used to calculate the loss cross–section.

3.7.2 Capture cross–section

Dewangan and Eichler wrote a review article on the topic of electron capture that is worth reading [37].

The capture cross–sections are divided in radiative electron capture and non radiative capture.

The non radiative electron capture cross–sections can be calculated using the continuum distorted wave approximation [38–40] or the eikonal approximation [29]. Both approximations are relativistic calculations.

The radiative electron capture cross–section can be calculated using the Bethe–Salpeter formula [30]. Both the Bethe–Salpeter as well as the eikonal approximation are used within ETACHA.

3.7.3 Auger decay

Both the electron capture as well as the electron loss process do not distinguish between a solid or a gas target. The target density N enters in eq. (3.8) only as a scaling parameter for the pathlength x, thus the denser the target the shorter the pathlength will be to reach the asymptotic charge fractions. However, to distinguish between a gas and a solid target the time between two subsequent collisions must play a role. By including the Auger decay of excited states (into a future implementation of the matrix method) this differentiation will improve and can in principle be done in the following way: The mean free path between two collisions is given by

$$\lambda(E) = \frac{1}{N \cdot \sigma(E)} \quad . \tag{3.9}$$

Here $\lambda(E)$ and $\sigma(E)$ are the energy dependent mean free path and the corresponding cross–section, respectively. Assuming that the ion's energy and therefore the velocity v is constant, the mean free path is given as

$$\lambda(E) = v \cdot t = \frac{1}{N \cdot \sigma(E)} \quad , \tag{3.10}$$

Where t is the mean collision time. Introducing now the Auger decay rate $\tau_{au} = 1/t$, substituting it in eq. (3.10), the cross–section for the corresponding Auger decay then reads

$$\sigma(E) = \frac{\tau_{au}}{N \cdot v} \quad . \tag{3.11}$$

The assumption that the ion's energy is constant leads to a constant Auger decay "cross–section". This assumption is easily fulfilled by dividing the targets into small layers. From eq. (3.11) it is evident that now the target density N also scales the cross–section. This means, if the target is dense enough, the excited state is still alive for at least one following collision and thus changing the probability for the loss or capture of the excited electron in that collision. This is schematically shown in fig. 3.12, where the black circles represent the target atoms, red circles represent an excited projectile and the green circle is a projectile in the ground state. Both projectiles are ionized during a collision with a target atom at the same point. Since the pathlength in which the projectile is still excited is shorter for the first projectile than the mean distance between two target atoms d, this projectile will undergo a collisional event with the next target atom in its ground state. While for the second exited projectile the pathlength in which the projectile is still in an excited state is longer than the mean distance d, thus the projectile collides with the next target atom while being in an excited state. In this gedankenexperiment the target density was kept fixed while the projectiles were given different lifetimes.

Obviously the reversed gedankenexperiment can by done by keeping the decay rate fixed and varying the mean atomic distance by changing the target density.

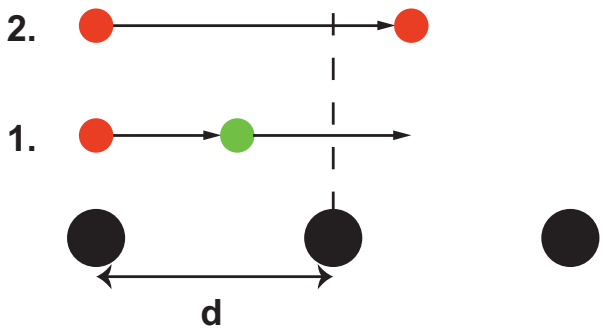

Figure 3.12: Collision between excited projectile (red) and target atoms (black) for fixed target density and variable Auger decay time. Green denotes a projectile in the ground state.

The gas/solid difference as well as the dependence on the target density of the equilibrium charge states has be experimentally confirmed by N. Lassen [41, 42] and is described by Bohr and Lindhard [20]. Tabulated values for both partial as well as total Auger decay rates are available in the literature [?].

3.7.4 Independent electron approximation

The calculation of partial cross–sections is usually performed using hydrogen–like projectiles, thus projectiles which are treated as bare hydrogen ions with a larger atomic number. Thus, capture/loss processes are usually treated as a capture/loss process into/from a bare projectile. However, in the case of a capture process into the 1s state for example, the cross–section to capture one electron depends heavily on the question of the 1s state being unoccupied or occupied by another electron. The capture cross–section into an unoccupied 1s state is significantly larger than the capture into an 1s state which is occupied by one electron.

The same consideration is applied for the loss process. The removal of one electron is more probable, hence the cross–section is larger, if the 1s state is initially occupied by two electrons, compared to the case of only one electron in the respective state.

To account for the effects of the "residual" electrons, the independent electron approximation is used. Within this approximation, the capture cross–section is scaled by the number of vacancies, while the loss cross–section is scaled by the number of electrons in the respective state.

Using measured partial capture cross–sections, the quality of the independent electron approximation can be tested. For that, the cross–section corresponding to the process $C^{6+}+H_2 \rightarrow C^{5+}+H_2^+$ is taken as the single electron capture cross–section $\sigma_{1s}^{(2)}$ into the 1s state. Therefor, the cross–section $\sigma_{1s}^{(2)}$ is the cross section of a bare C ion, *i.e.* a C ion with two 1s vacancies, to capture one electron into the unoccupied 1s state.

Consequently, the cross–section to capture one electron into the 1s state that is occupied with one electron, *i.e.* with one vacancy, is called $\sigma_{1s}^{(1)}$. Measuring the process $C^{5+}+H_2 \rightarrow C^{4+}+H_2^+$ yields $\sigma_{1s}^{(1)}$.

Within the independent electron approximation $\sigma_{1s}^{(2)}$ and $\sigma_{1s}^{(1)}$ are related in such a way, that

$$\sigma_{1s}^{(2)} = 2\sigma_{1s}^{(1)} \rightarrow \sigma_{1s}^{(1)} = \sigma_{1s}^{(2)}/2. \tag{3.12}$$

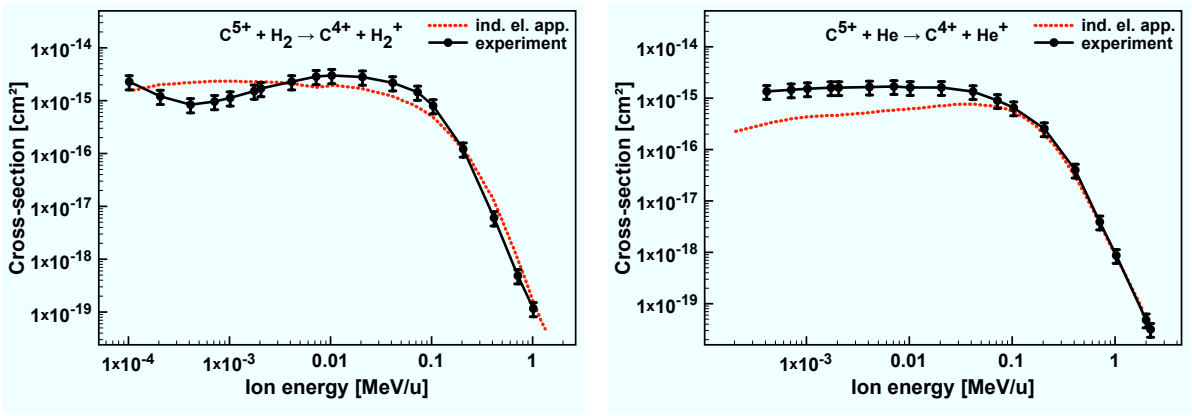

Figure 3.13: Capture cross–section into 1s state for different processes.
Left: $C^{5+} + H_2 \rightarrow C^{4+} + H_2^+$
Right: $C^{5+} + He \rightarrow C^{4+} + He^+$
Dashed line: independent electron approximation.
Points: experimental measurements.

Equation (3.12) can be directly verified if both cross–sections are measured. The experimental data were made available by Preben Hvelplund and Helge Knudsen from the University of Aarhus. In the interpretation of the experimental data two assumptions have been made: First, the electron related to the C^{5+} ion is initially in the 1s ground state, and second, the electron is captured directly into the 1s ground state of the C^{6+} ion.

The data points in figure 3.13 (left graph) show the capture cross–section $\sigma_{1s}^{(1)}$ for the transition $C^{5+} \rightarrow C^{4+}$. The red dotted line shows the calculated cross–section according to (3.12) as obtained from the measurements of the capture process $C^{6+} \rightarrow C^{5+}$. Within the independent electron approximation, both cross–sections should be equal, *i.e.* both curves should be equal. However, rather strong deviations are observed, where not even the trend is predicted correctly, for ion energies smaller than 0.1 MeV/u. For larger energies the overall agreement is quite satisfactory.

The same calculation is done for the process $C^{5+} + He \rightarrow C^{4+} + He^+$ and is shown in the right graph in figure 3.13. The independent electron approximation shows a significant underestimation of the σ_{1s}^{1} cross–section for energies lower than 0.1 MeV/u, while for larger energies the agreement is again much better.

Figure 3.14 (left graph) shows the independent electron approximation for the process $O^{7+} + H \rightarrow O^{6+} + H^+$, where the process $O^{8+} + H \rightarrow O^{7+} + H^+$ is taken as the single electron capture cross–section $\sigma_{1s}^{(2)}$ into the 1s state. Here, an underestimation of the cross–section for low energies is observed, while being slightly overestimated for larger energies. However, the overestimation is well within the experimental error bars.

Finally, the case $C^{3+} + H_2 \rightarrow C^{2+} + H_2^+$ is studied. In this case, the electron is not captured into the 1s state, but into the 2s state of the ion. The general considerations are the same, so that eq. (3.12) is used while replacing 1s with 2s. The result is shown in the right graph in figure 3.14. Unlike the case for the capture into 1s, here the independent electron approximation overestimates the capture cross–section. Furthermore, the approximation fails to reproduce the minimum around 9×10^{-4} MeV/u. Again for energies around 0.1 MeV/u the agreement

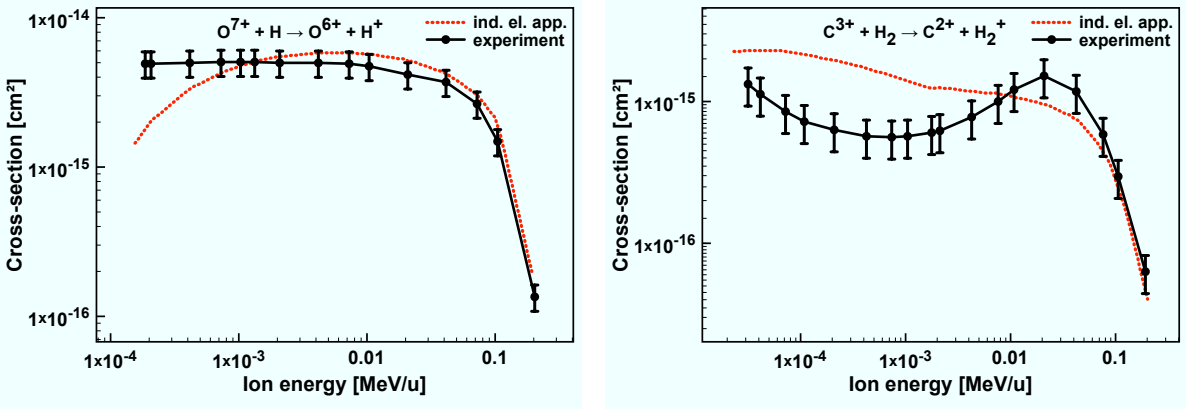

Figure 3.14: Capture cross–section for different processes.
Left: $O^{7+} + H \rightarrow O^{6+} + H^+$ (capture into 1s)
Right: $C^{3+} + H_2 \rightarrow C^{2+} + H_2^+$ (capture into 2s)
Dashed line: independent electron approximation.
Points: experimental measurements.

between the measurements and the independent electron approximation is good.

From figures 3.13 and 3.14 it is observed that the cross–sections for ion energies larger than 0.1 MeV/u are reproduced in a satisfactory way. Larger deviations are found for low energies. This can be understood quite easily, as the interaction time between electrons decreases with increasing ion velocities and thus more correlations between the electrons are expected at low ion velocities. It should be noted here that only the most simplest cases of 1s and 2s capture were studied. In both cases the number of allowed electrons is two per state. For the case of capture into 2p the system is much more complicated, as this state allows for six electrons. Additionally, the assumptions made in this section are rather drastic. Here it was assumed that the electrons are captured directly into the 1s state of the bare ion and that the electrons of the ion were initially in the 1s ground state before the capture process, *i.e.* any excitation is neglected. The same assumption is even more severe for the case of 2s capture, where all residual electrons are assumed to be in their ground state.

3.8 Scaling rules

As was mentioned, the use of partial cross–section leads to the calculation of much more states than the available charge states. This is undesirable in the case of heavy ions, since cross–sections for all participating states are not available. However, most of the calculations deal with partial cross–sections. Additionally, the use of partial cross–sections leads to the use of the independent electron approximation. This approximation is not applicable for low energetic ions. Even at high energies, this approximation may break down for certain projectile target combinations. Over the years many experiments were performed measuring cross–sections related to charge exchange processes. With the amount of available data, scaling rules were considered, *i.e.* empirical formulas to predict cross–sections. In this section different scaling rules for the electron capture cross–sections will be shown. The general idea is, that in future works such scaling rules will be used to deliver total capture cross–sections as input for the

matrix method.

3.8.1 Schlachter formula

The general derivation of the scaling formula for electron capture cross–sections given by Schlachter *et al.* [43] is as follows:

Generalized reduced coordinates are introduced

$$\sigma' = \sigma Z_2^{c1}/q^{c2} \quad , \quad E' = E/(Z_2^{c3} q^{c4}), \tag{3.13}$$

where σ is the electron capture cross–section, q is the projectile charge state, E is the projectile energy per nucleon and Z_2 is the target atomic number and c_1–c_4 are fitting parameters.

The reduced capture–cross section is given as

$$\sigma' = P_1 \cdot \frac{1-\exp(-P_2 E'^{P_4})}{P_2 E'^{P4}} \cdot \frac{1-\exp(P_3 E'^{P_5})}{P_3 E'^{P_5}}, \tag{3.14}$$

with P_1–P_5 being fitting parameters.

These scaling parameters are fitted to measured electron capture cross–section data using a least–squares fit, which then yields

$$\sigma' = \sigma Z_2^{1.8}/q^{0.5} \quad , \quad E' = E/(Z_2^{1.25} q^{0.7}), \tag{3.15}$$

with σ in cm^2 and E in keV/u.

And finally

$$\sigma' = \frac{1.1\times 10^{-8}}{E'^{4.8}} \cdot [1-\exp(-0.037 E'^{2.2})] \cdot [1-\exp(-2.44\times 10^{-5} E'^{2.6})]. \tag{3.16}$$

Equation (3.16) is restricted by:

$$E' \geq 10 \quad , \quad q \geq 3. \tag{3.17}$$

A comparison with measured cross–sections is given in figure 3.15, where the axes are plotted in reduced coordinates according to eq. (3.15). It should be noted that the Schlachter formula is only valid for single–capture events.

3.8.2 CAPTURE code

Shevelko et al. [44] have compared different methods to calculate the electron–capture cross section:

- The Schlachter formula
- The eikonal approximation [29]
- Their CAPTURE code [45]

While in general the eikonal approximation and the CAPTURE code both calculate partial capture cross sections σ_n, where $n = 1s,\ 2s...$, the total cross section σ_{tot} is compared with the Schlachter formula using that

$$\sigma_{tot} = \sum_n \sigma_n.$$

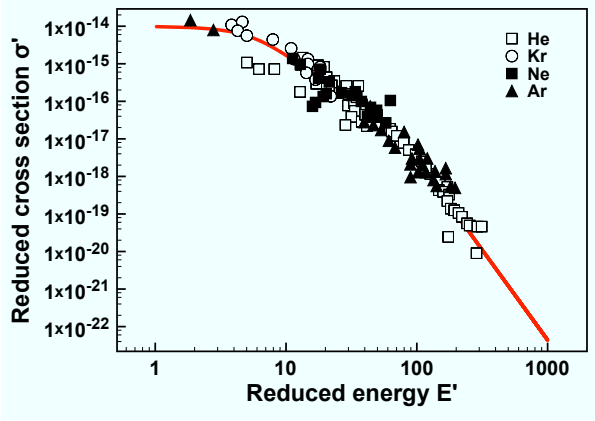

Figure 3.15: Electron–capture cross section data in reduced coordinates. Solid line: eq. (3.16) The figure is reproduced from [43].

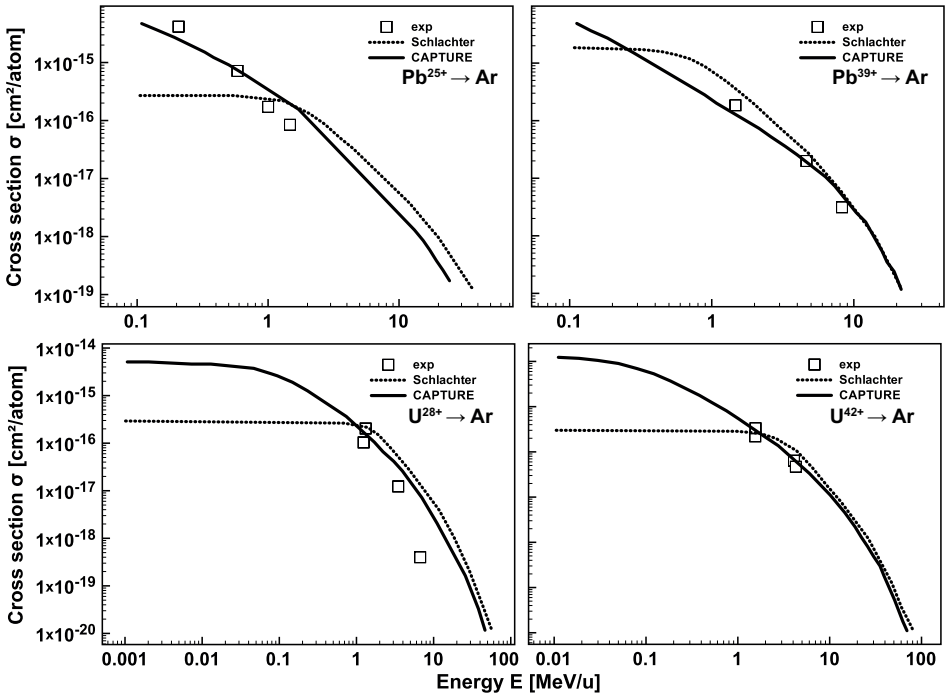

Figure 3.16: Electron–capture cross sections. Comparison between CAPTURE code and the Schlachter formula with experiments. The figures are reproduced from [44]

The CAPTURE code, a quantum mechanical code based on the Oppenheimer–Brinkmann–Kramers approximation[3], is valid for ion energies from 0.1 MeV/u to 100 MeV/u [44, 45]. The comparison between the Schlachter formula and the CAPTURE code shows how both agree fairly well with each other for $E > 1$ MeV/u. However, the Schlachter formula shows a

[3]The OBK approximation is in principal a perturbation theory.

significantly lower cross section for $E < 1$ MeV/u, due to the fact that the predicted drop in the cross–section "starts" at larger energies for the Schlachter formula than for the CAPTURE code. This is shown in figure 3.16.

3.8.3 Knudsen scaling rule

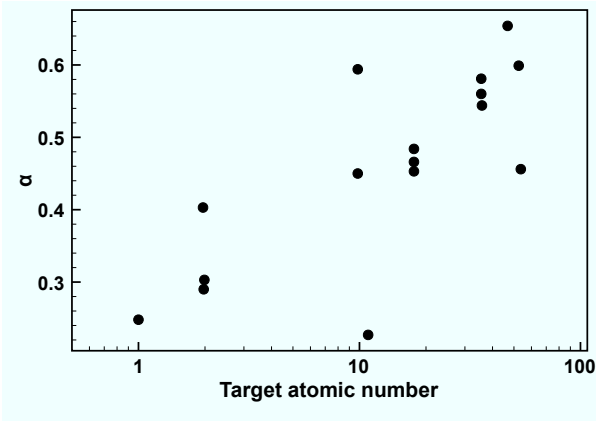

Figure 3.17: The adjustable parameter α versus target atomic number entering eq. (3.18). Reproduced from [46].

Knudsen *et al.* [46] suggested a scaling rule for the electronic–capture cross section as follows:

$$\frac{\sigma}{\pi a_0^2 q} = \begin{cases} \frac{1}{2}Z^{2/3}\left[\left(\frac{\alpha v_a}{v_0}\right)^{-2} - (\beta Z)^{-2}\right] & (v_1 < \alpha v_a) \\ \frac{8}{3}\xi^{-7}\left[\left(\frac{z^{2/3}}{8}\xi^7\right)^{3/5} - \left(\frac{\alpha v_a}{v_0}\right)^3\right] + \frac{1}{2}Z^{2/3}\left[\left(\frac{z^{2/3}}{8}\xi^7\right)^{-2/5} - (\beta Z)^{-2}\right] & (\alpha v_a < v_1 < \beta Z v_0) \\ \frac{8}{3}\xi^{-7}\left[(\beta Z)^3 - \left(\frac{\alpha v_a}{v_0}\right)^3\right] & (\beta Z v_0 < v_1), \end{cases} \quad (3.18)$$

where Z is the target atomic number, v_0 the Bohr velocity, a_0 the Bohr radius and q the ion charge. Furthermore

$$v_a = v_0(I/I_0)^{1/2},$$

where $I_0 = \frac{1}{2}mv_0^2$ and I is the atomic ionization potential.

The parameter β is a normalization parameter and is given as

$$\beta = Z^{-1/3} + \frac{\alpha}{Z}\frac{v_a}{v_0}.$$

α is used as a scaling parameter taking values between 0 and 1. The velocity v_1 is given as

$$v_1 = \left[\frac{Z^{2/3}}{8q^2}\left(\frac{V}{v_0}\right)^7\right]^{1/5} v_0,$$

where V is the ion velocity.
Finally

$$\xi = \left(\frac{1}{25} E/q^{4/7} \right)^{1/2},$$

where E is the ion energy in keV/u and q is the projectile charge state.
Equation (3.18) is limited by $q \geq 4$ and by

$$2q(V/v_0)^{-1} \ll 1.$$

The cross–section obtained by eq. (3.18) is sensitive in the parameter α. The authors state that for defining α, figure 3.17 can be used. However, for the case of a target atomic number 10 (neon) the value α varies between 0.2 and 0.6. These large variations are caused by the closing of atomic shells and can also be found for argon and xenon.

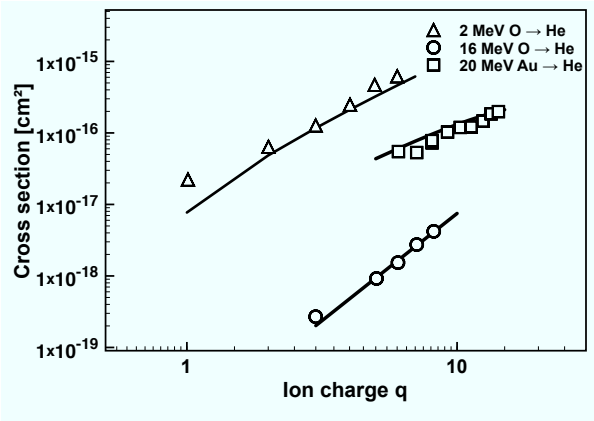

Figure 3.18: Comparison between experimental data (symbol) [46] for single-capture cross–section versus the ion charge q and eq. (3.18) (solid line). Gold data is scaled by a factor of 0.1. Data points taken from [46].

The scaling law eq. (3.18) was tested thoroughly in the original work [46]. For the implementation in the matrix method, the dependence of the cross–section on the ion charge is of great importance. The dependence of the capture cross–section on the ion charge is shown in figure 3.18 for the irradiation scenario of oxygen at 2 MeV and 16 MeV in helium and 20 MeV gold in helium. The correspondence between the calculated cross–sections and the experimental measurements is in good agreement. For the sake of readability the gold data is scaled by a factor of 0.1.

It should be noted here that the scaling law given by Knudsen et al. is only valid for single–capture events.

Furthermore the scaled capture cross–section results obtained via ETACHA were compared with the scaling rule given by eq. (3.18) for the case of S in C @ 10 MeV/u. The result is shown in fig. 3.19. In general the agreement in the trend and the magnitude is fairly well. The biggest deviations between the scaling rule and the ETACHA cross–section are observed for the case of low ion charge, where ETACHA predicts a non zero capture probability for neutral atoms.

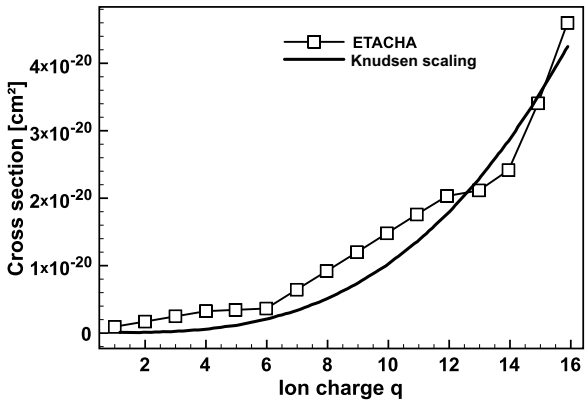

Figure 3.19: Comparison between the scaled capture cross–section obtained via the ETACHA code (symbols) and the scaling rule eq. (3.18) (solid line).

3.9 Equilibrium charge state

The equilibrium charge state of an ion traversing through matter can be calculated by using the Thomas–Fermi estimation [47]

$$\langle q \rangle = Z_1 \left(1 - e^{-v/Z_1^{2/3} v_0}\right), \tag{3.19}$$

where Z_1 and v are the ion's atomic number and velocity and v_0 is the Bohr velocity. This estimation is in good agreement with experimental data at least up to argon ions [47].

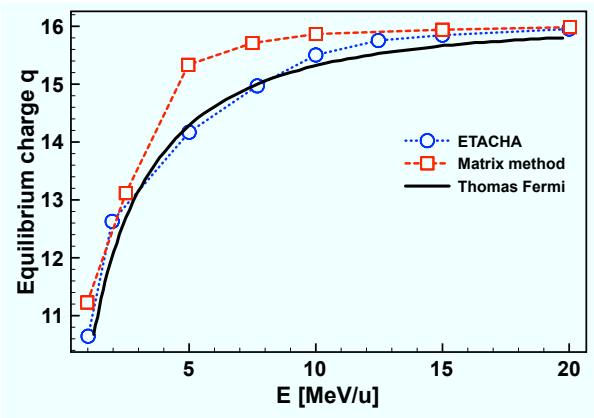

Figure 3.20: Calculated equilibrium charge for S in C. Squares: matrix method. Circles: ETACHA. Solid line: Thomas Fermi estimate eq. (3.19). Figure taken from [14].

Shima *et al.* have analyzed measurements of mean charge states of ions after emergence from foils. This analysis led to an empirical formula to determine the ion's mean charge [48]

$$\langle q \rangle = Z_1 \left[1 - \exp(-1.25X + 0.32X^2 - 0.11X^3)\right] \left[1 - 0.0019(Z_2 - 6)\sqrt{X} + 10^{-5}(Z_2 - 6)^2 X\right], \tag{3.20}$$

where Z_1 and Z_2 are the ion and target foil atomic number, and X is a reduced ion velocity

$$X = v/Z_1^{0.45} v_0.$$

The authors state that eq. (3.20) is valid for $Z_1 \geq 8$, $4 \leq Z_2 \leq 79$ and $E \leq 6$ MeV/u.

A direct comparison of the equilibrium charge $\langle q \rangle$ obtained using the ETACHA code and the matrix method for the case of S in C is given in figure 3.20. Additionally, the equilibrium charge predicted by the Thomas–Fermi estimate eq. (3.19) is shown. While the ETACHA calculations are in good agreement with the Thomas–Fermi estimate, the matrix method shows a strong overestimation of the equilibrium charge state by almost 2 charges within (5–10) MeV/u. The comparison with ETACHA is much better for larger ion energies.

The origin of this overestimation is not yet understood.

3.10 Conclusions

The matrix method is from a numerical point of view a superior way to compute charge fractions vs. the pathlength of the incoming ion beam using cross–sectional input. The accuracy of the method is given by the quality of the input and can easily be predetermined. Unlike using the numerical solution of the rate equations or Monte Carlo methods, charge fractions can be determined at any desired depth x without having to pre–calculate all charge fractions $\mathbf{F}(x)$ for all previous values of x. The numerical implementation is easy and fast, allowing to compute systems of 100 states or more. The use of a truncated exponential series implies convergence problems for large pathlengths. This can be easily overcome by dividing the target into layers and subsequently convoluting the solution. Doing so also allows to take the energy loss of the projectile into account in future implementations of the matrix method. In the present implementation the cross–section input is extracted using the ETACHA code. While ETACHA calculates partial cross–sections, total cross–sections are used in the matrix method by summation of all cross–sections belonging to a pertinent charge state. This implies that excitation and deexcitation of states is not yet included in the model. Excitation states can be included in principle by allowing one (mean) or more excited states per charge state.

So far the results obtained by the matrix method are less than satisfactory, but are believed to become quite accurate with improved cross–sections.

For future works it is planned to use scaling laws as those outlined in section 3.8 to deliver the input for capture cross–section, while loss and excitation cross–sections can be obtained utilizing the binary collision theory. A general idea of how to incorporate Auger decay processes was outlined in section 3.7.3.

As was pointed out in section 2.6 the matrix method can be used to compute related quantities like the energy loss and straggling in the presence of charge exchange. A first step in doing so was reported in [14].

4 Two temperature model

In the previous chapter the effect of the target on the penetrating ion was studied. The penetration of a stopping media leads to charge exchange processes. The present chapter in turn describes the effect of the penetrating ion on the target, *i.e.* the excitation of the target electrons and the subsequent energy transfer into the lattice by electron–phonon coupling. While the excitation of the target electrons leads to an increase of the electron temperature, electron–phonon couplings lead to an increase of the phonon temperature. In this chapter the basic model to describe the electron energy transport, the electron–phonon coupling as well as the necessary parameters will be explained. Finally, the model is applied to the irradiation of crystalline silicon with a swift heavy ion. This application will demonstrate the drawbacks of the model.

4.1 Introduction

The interaction of MeV ion beams with solids is a process which primarily involves the excitation of electrons. The energy of the excited electrons is distributed through the target due to electron–electron collisions, while the target itself is heated subsequently via electron–phonon interactions.

First calculations of the spreading of the electron energy and the heating of the lattice due to this swift heavy ion irradiation based on a two temperature approach emerged back in the mid 1950s [49–52]. The general idea is to treat the electron propagation within an integrated continuum approximation. Thus instead of calculating the transport based on the electron's momentum and coordinates, the computed quantity is the integrated momentum, the electron's kinetic energy. The electron–phonon collisions result in the effective emission of phonons, thus heating the lattice. From a conceptual point of view the heating of a target by a swift heavy ion beam is similar to the heating by a laser pulse. In both cases the primary energy dissipation is due to the excitation of target electrons. In 1974 Anisimov *et al.* [53] applied the two temperature model (TTM) to the case of laser excitation, improving the method and in a general sense made it popular [54–61].

4.2 Basics

The basic process of the irradiation of a target matter with swift heavy ions (SHI) has been outlined in the introduction. The ion loses part of its kinetic energy due to inelastic collisions with the target electrons, thus exciting these target electrons. These electrons then can traverse through the target and may lose energy due to emission of phonons [62, 63], which in turn results in the heating of the lattice. This spreading of the electron energy and the heating of the lattice can be treated with the help of the two temperature model. In this model the spatial and temporal evolution of the electronic and phononic system are represented via a set of two coupled heat diffusion equations, one for each subsystem:

$$
\begin{aligned}
C_e(T_e)\frac{\partial T_e}{\partial t}(\vec{r},t) &= \nabla\cdot(\kappa_e(T_e)\nabla T_e(\vec{r},t)) - \\
&- g(T_e,T_p)\cdot(T_e(\vec{r},t)-T_p(\vec{r},t)) + S(\vec{r},t)\ , \qquad (4.1)\\
C_p(T_p)\frac{\partial T_p}{\partial t}(\vec{r},t) &= \nabla\cdot(\kappa_p(T_p)\nabla T_p(\vec{r},t)) + \\
&+ g(T_e,T_p)\cdot(T_e(\vec{r},t)-T_p(\vec{r},t))\ . \qquad (4.2)
\end{aligned}
$$

The subscripts e and p represent the electronic and phononic system, respectively, while $\kappa_e(T_e)$ and $\kappa_p(T_p)$ denote the heat conductivity and $C_e(T_e)$ and $C_p(T_p)$ denote the temperature dependent heat capacity of the electrons and the lattice, respectively. Both equations are coupled by an exchange term $g(T_e,T_p)$ generally also depending on T_e and T_p, the so called electron–phonon coupling parameter. The ion's energy loss is used as a source term for the electron system and is denoted by $S(\vec{r},t)$. Any nuclear stopping, *i.e.* energy transfer of the ion directly into the nuclear subsystem due to ion–atom collisions is neglected here, since the electronic excitation dominates the nuclear collisions by more than two orders of magnitude [64, 65].

The heat conductivity can be expressed as

$$\kappa_{e,p}(T_{e,p}) = D_{e,p}(T_{e,p})\cdot C_{e,p}(T_{e,p})\ , \qquad (4.3)$$

allowing to substitute the heat conductivity with the diffusivity $D_{e,p}(T_{e,p})$ in eqs. (4.1) and (4.2), which then read

$$
\begin{aligned}
C_e(T_e)\frac{\partial T_e}{\partial t}(\vec{r},t) &= \nabla\cdot(D_e(T_e)C_e(T_e)\nabla T_e(\vec{r},t)) - \\
&- g\cdot(T_e(\vec{r},t)-T_p(\vec{r},t)) + S(\vec{r},t)\ , \qquad (4.4)\\
C_p(T_p)\frac{\partial T_p}{\partial t}(\vec{r},t) &= \nabla\cdot(D_p(T_p)C_p(T_e)\nabla T_p(\vec{r},t)) + \\
&+ g\cdot(T_e(\vec{r},t)-T_p(\vec{r},t))\ . \qquad (4.5)
\end{aligned}
$$

Doing so, both equations now are governed by the diffusivity D instead of the heat conductivity, while the heat capacity C acts only as a conversion factor between the temperature and the energy.

4.3 Source term $S(r,t)$

As can be seen from eq. (4.4), the energy loss of the incoming ion provides the source term for the initial electronic excitation. Obviously, the shape of the function $S(\vec{r},t)$ plays an important role. Assuming a fixed energy deposition x, then the energy per unit area and unit time will affect the solution of eqs. (4.4) and (4.5).

Following [66, 67] the source term for a cylindrical excitation can be written as

$$S(r,t) = bS_e \exp\left[-(t-t_0)^2/2\sigma^2\right] F(r)\ , \qquad (4.6)$$

where t is measured from the moment of the ion impact and r is the radial distance from the ion's impact point. The half–width of the Gaussian σ is chosen to be equal to t_0. The time t_0 is assumed to be the mean time of flight of the (mean) δ–electrons, *i.e.* electrons that were initially excited by the incoming ion, and is in the order of 1 fs [67]. In [66] the authors claim that t_0 is equal to the time required for the electrons to reach the equilibrium distribution.

The spatial distribution $F(r)$ is given by the formulation of Waligorski *et al.* [68] and reads[1]

$$F(r) = \frac{n_e e^4 Z^{*2}}{\alpha m_e c^2 \beta^2 r} \left[\frac{\left(1 - \frac{r+\theta}{\mathfrak{T}+\theta}\right)^{\frac{1}{\gamma}}}{r+\theta} \right] \quad . \tag{4.7}$$

Here n_e is the number of electrons per cm^3, e is the elementary charge, while Z^* is the effective charge of an ion moving with the relative velocity $\beta = V/c$ (c is the speed of light and V is the ions velocity) and γ is a constant. Following the argument given by Waligorski *et. al*, the relation between the range (r) and the energy (w) of an electron can be expressed by a power law

$$r = kw^{\gamma} \quad , \tag{4.8}$$

where the proportionality constant k is given as[2]

$$k = 6 \times 10^{-6} \text{g cm}^{-2} \text{keV}^{-\gamma} \quad . \tag{4.9}$$

The constant γ is

$$\begin{aligned} \gamma &= 1.079 \text{ for } w < 1 \text{ keV} \quad , \\ \gamma &= 1.667 \text{ for } w > 1 \text{ keV} \quad . \end{aligned} \tag{4.10}$$

Furthermore, θ is the minimal range of an electron, *i.e.* the range of an electron with the energy w=I according to eq. (4.8), where I is the target ionization potential. The maximum range of an electron $\mathfrak{T}$ is limited by the kinematically allowed maximal energy transfer W, thus according to eq. (4.8),

$$\mathfrak{T} = kW^{\gamma} \text{ and,} \tag{4.11}$$

$$W = \frac{2m_e c^2 \beta^2}{1-\beta^2} \quad . \tag{4.12}$$

Finally b in eq. (4.7) is a normalization constant, so that

$$\int_0^{r_m} \int_0^{\infty} 2\pi r b S_e \exp\left[-(t-t_0)^2/2\sigma^2\right] F(r) \mathrm{d}r\mathrm{d}t = S_e \quad , \tag{4.13}$$

while S_e is the projectile's electronic stopping power. Equation (4.6) assumes a smooth radial distribution for the electron energy. This is not necessarily the case. Improvements may be achieved via the incorporation of electron velocity distributions.

The main advantage of eq. (4.6) is its simple form and the fact that the stopping power S_e can readily be obtained, using for instance the SRIM code [69].

[1] It should be noted, that here the radius r is in units of g/cm^2. Conversion from g/cm^2 to cm is simply done with the knowledge of the target atomic density.

[2] The unit of the constant k indeed depends on the constant γ defined by eq. (4.10).

4.4 Electronic System

The irradiation of metals by ion or laser beams has been studied thoroughly using the TTM. Unlike in a metal, in an insulator electrons participating in the heat transferring process first have to be excited into the conduction band. Therefore the heat transfer and the excitation process are strongly entwined processes.

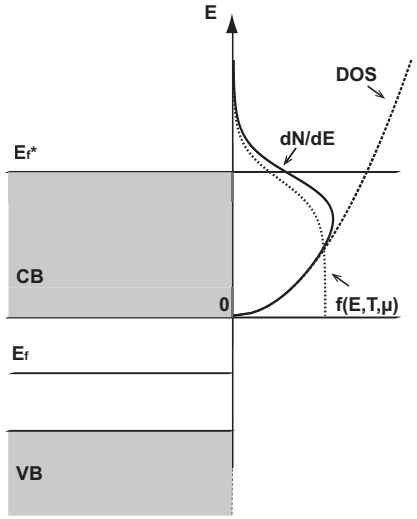

Figure 4.1: Schematic view of the valence (VB) and conduction band (CB) of an insulator. Electrons can be excited by the swift heavy ion from the valence into the conduction band. The excited electrons are then treated as a free electron gas with their appropriate Fermi distribution and a free electron density of states. The energy zero point is assumed at the bottom of the conduction band.

One fundamental idea for the description of ion–excited insulators is that excited electrons in an insulator behave like free electrons in a metal [64]. According to this idea, the electrons in the conduction band can be described by a *pseudo* fermi distribution, a *pseudo* fermi energy E_f^* and a free electron gas density of states (DOS). The energy zero point is located at the bottom of the conduction band. This is schematically shown in fig. 4.1. This pseudo fermi distribution starts at the bottom of the conduction band and stretches into infinity.

Within this chapter the electrons in the conduction band are assumed to be thermalized at all times. This assumption will be relaxed in chapter 5, where the thermalization of the conduction band electrons will be considered separately.

4.4.1 Electron Heat Capacity

The temperature dependence of the electron heat capacity can by directly obtained using the fermi distribution, which often, however, is not known directly. Instead one often uses the free electron gas model, where the temperature dependence of the electron heat capacity is usually approximated by introducing two distinct temperature regimes. For low electron temperatures the heat capacity can be calculated using $C_e = \gamma T_e$, where T_e is the electron temperature and

γ the heat capacity constant, which is given by

$$\gamma = \frac{\pi^2}{2}\frac{n_e k_B^2}{E_F} \ , \tag{4.14}$$

where $E_F = \hbar^2/2m_e$ is the Fermi energy, m_e is the electron mass, n_e the electron density. Also the Planck constant $\hbar$ and the Boltzmann constant k_B are introduced. This proportionality in T_e is followed up to the Fermi temperature $T_F = E_F/k_B$, at which the heat capacity remains constant

$$C_e = \frac{3}{2} n_e k_B \ . \tag{4.15}$$

Doing so, the transition from the linear temperature dependence to the constant value of the heat capacity is not well defined, *i.e.* the complicated intermediate temperature regime is not considered in detail. The use of eq. (4.14) assumes a good knowledge of the Fermi energy, while both equations, (4.14) and (4.15), require the electron density to be known.

In the case of a metal, the electron density is trivially given. However, in the case of an insulator the electron density in the conduction band is initially close to zero, thus the value of the electron density entering eqs. (4.14) and (4.15) is non trivial.

4.4.2 Electronic Diffusivity

If one considers a gas composed of n particles with a mean velocity $\langle v \rangle$, then the particle current J is given as

$$J = \frac{1}{6} n \langle v \rangle \ , \tag{4.16}$$

where the factor 1/6 stems from averaging the motion of the particles in all positive and negative directions $(\pm x, \pm y, \pm z)$. Considering now a concentration gradient along a certain direction x. Let the concentration at x be n, while the concentration at $x \pm \lambda$ is $n \pm \lambda dn/dx$. This is shown in figure 4.2. The particle current along the positive x direction J^+ then is

$$J^+ = \frac{1}{6} n \langle v \rangle + \frac{1}{6}\frac{dn}{dx} \lambda \langle v \rangle \ , \tag{4.17}$$

while the particle current along the negative x direction J^- is

$$J^- = \frac{1}{6} n \langle v \rangle - \frac{1}{6}\frac{dn}{dx} \lambda \langle v \rangle \ . \tag{4.18}$$

The resulting current along the positive x axes is then given by

$$J = J^+ - J^- = -\frac{1}{3}\frac{dn}{dx} \lambda \langle v \rangle \ . \tag{4.19}$$

With a definition similar to that of the Fourier's law one can rewrite eq. (4.19)

$$J \equiv -D\frac{dn}{dx} \ , \tag{4.20}$$

comparing eqs. (4.19) and (4.20) finally gives the diffusion coefficient

$$D = \frac{1}{3} \lambda \langle v \rangle \ , \tag{4.21}$$

where λ can be identified as the particles mean free path. The mean free path can be expressed in terms of a scattering rate τ, so that D can be written as

$$D = \frac{1}{3}\lambda v = \frac{1}{3}\langle v\rangle^2 \tau \ . \tag{4.22}$$

For the case of electrons, both the electron–electron scattering rate τ_{e-e} as well as the electron–phonon scattering rate τ_{e-ph} contribute to the total scattering rate τ [70]

$$\frac{1}{\tau} = \frac{1}{\tau_{e-e}} + \frac{1}{\tau_{e-p}} = aT_e^2 + bT_p \ , \tag{4.23}$$

where a and b are parameters, which can be extracted for instance using low temperature resistivity measurements [61]. Using eq. (4.23) in (4.22) then yields the electron diffusivity D_e

$$D_e(T_e, T_p) = \frac{1}{3}\frac{\langle v\rangle^2}{aT_e^2 + bT_p} \ . \tag{4.24}$$

In the case of metals, the velocity entering eq. (4.22) can be identified as the Fermi velocity.

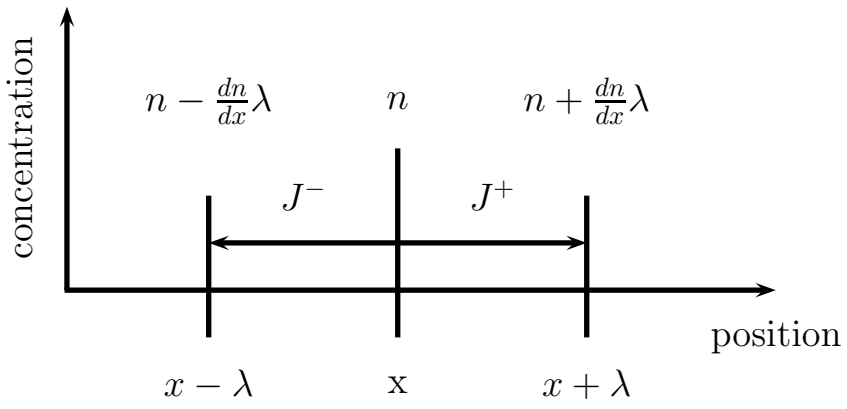

Figure 4.2: Schematic drawing of a gas with different concentrations n at different positions x.

For insulators this velocity is equal to the pseudo Fermi velocity of the conduction band electrons (compare figure 4.1). Assuming that the electrons can be described by a Fermi distribution at all times leads to a velocity proportional to the square root of the electron temperature $v \propto \sqrt{T_e}$ and finally a temperature–dependent electron diffusivity

$$D_e(T_e, T_p) = \frac{2k_B}{\pi m_e}\frac{T_e}{aT_e^2 + bT_p} \ . \tag{4.25}$$

For $bT_p \ll aT_e^2$ equation (4.25) is proportional to $1/T_e$ confining the electronic excitation to a small area [61].

4.5 Phononic System

While the penetrating ion interacts only with the electronic system, the lattice is heated due to electron–phonon scattering. Phonon–phonon scattering then transports the energy out of the excitation region [71]. This can be described by the lattice diffusivity

$$D_p(T_P) = \frac{\kappa_p(T_p)}{C_p(T_p)} \ . \tag{4.26}$$

The temperature–dependent heat conductivity is approximated by $\kappa = (\alpha T_p)^{-1}$ [72] with a fitting parameter α. Tabulated data for various materials at different temperatures exist throughout the literature, both for the heat conductivity as well as for the heat capacity.

4.6 Electron–Phonon Coupling

First estimations of the interaction strength between electrons and phonons, the so called electron–phonon coupling, were performed by Kaganov *et al.* [51] on the basis of the free electron gas model. There it was suggested that the energy exchange rate between electrons and phonons could be related to the electron relaxation times at the appropriate electron and phonon temperatures, T_e and T_p, respectively. For electron and phonon temperatures much higher than the material's Debye temperature T_D, the electron–phonon coupling can be written as

$$g = \frac{\pi^2}{6} \frac{m_e n_e v_s^2}{\tau(T_e) T_e} \quad , \quad T_e \gg T_p \gg T_D, \tag{4.27}$$

where m_e is the (effective) electron mass and n_e is the electron density. In the original work of Kaganov *et al.* [51], $\tau(T_e)$ is called 'the time of free flight of an electron'. The sound velocity v_s is given as

$$v_s = \frac{k_B T_D}{\hbar (6\pi^2 n_a)^{1/3}} \ , \tag{4.28}$$

here n_a is the atomic density. The electron–phonon energy exchange rate reads

$$\frac{\partial E_e}{\partial t}|_{e-p} = g \cdot (T_p - T_e) \ . \tag{4.29}$$

Assuming further that $\tau(T_e) \propto T_e^{-1}$ [73], the coupling factor g eq. (4.27) becomes constant.

The determination of the scattering rate $\tau(T_e)$ is a complicated task. To avoid this problem Wang et al. [74] have related the scattering rate to the electrical conductivity $\sigma_e(T_e)$ via the Drude model [75, 76]:

$$\sigma_E(T_e) = \frac{e^2 \tau n_e}{m_e} \ , \tag{4.30}$$

substituting this into eq. (4.27) gives

$$g = \frac{\pi^2}{6} \frac{(e n_e v_s)^2}{\sigma_e(T_e) T_e} \ . \tag{4.31}$$

Furthermore, by using the Wiedemann–Franz law

$$\kappa_e(T_e) = L \sigma_e(T_e) T_e \ , \tag{4.32}$$

where L is the Lorentz number, the electron–phonon coupling can be written as

$$g = \frac{\pi^2}{6} \frac{(en_e v)^2 L}{\sigma_e(T_e) T_e} \quad . \tag{4.33}$$

By substituting the Lorentz number $L = \frac{\pi^2}{3} \left(\frac{k_B}{e}\right)^2$ the authors of [74] obtained an electron–phonon coupling which depends on the electron heat conductivity

$$g = \frac{\pi^4}{18} \frac{(k_B n_e v)^2}{\kappa_e(T_e)} \quad . \tag{4.34}$$

Going beyond the free electron gas model and incorporating the electron density of states, an estimate on the electron–phonon exchange rate can be found on the basis of rate equations for the electron–phonon collisions. This was done by Allen [77], where it was found that the energy exchange between electrons and the lattice can be expressed as

$$\frac{\partial E_e}{\partial t}|_{e-p} = \frac{4\pi}{\hbar} \sum_{k,k\prime} \hbar\omega_Q |M_{kk'}|^2 S(k,k') \delta(\epsilon_k - \epsilon_{k'} + \hbar\omega_Q) \quad , \tag{4.35}$$

where k and Q denote the electron and phonon quantum numbers, respectively, and $M_{kk'}$ is the matrix element, *i.e.* the probability for a scattering of an electron from the initial state k, and the corresponding energy ϵ_k into the state k' with the energy $\epsilon_{k'}$ due to scattering with a phonon with the energy $\hbar\omega_Q$. The term $S(k,k')$ is given as

$$S(k,k') = (f_k - f_{k'}) n_Q - (1 - f_k) f_{k'} \quad , \tag{4.36}$$

and expresses the phonon emission and absorption process during the electron–phonon scattering, where f_k and n_Q are the electron and phonon occupation numbers, respectively. Equation (4.35) allows the use of arbitrary electron densities of state, thus allowing for a material specific estimation of the electron–phonon coupling, provided that the matrix element $M_{kk'}$ is known.

4.7 Application

In this section the TTM will be applied to the irradiation of crystalline silicon (c–Si). The material parameters for the c–Si lattice are well known from experiments. However, no data is available for the electron system. These parameters, especially the electron–phonon coupling g, will be treated as free parameters. Within this section, the effect of selected parameters like g will be studied by a variation of these parameters. As was mentioned in the introduction, the TTM assumes melting of the target as the cause of the experimentally observable modifications. Additionally, similar to the ablation of matter due to intense laser irradiation, vaporization might be the cause of the modification. Therefore, both criteria will be compared. Another point to be addressed will be the source term $S(r,t)$, given by eq. (4.6), where the influence of non thermal electrons will be studied in a simple manner. The calculations are performed in cylindrical geometry with the cylinder axis perpendicular to the ion trajectory. The output of these calculations are temporal and spatial resolved lattice temperatures. Using the melting/vaporization criterion the so–called damage threshold S_{th} can be determined. The damage threshold is the minimal required stopping power, provided by the penetrating ion,

in order to damage the target. Measurements as well as calculations of this damage threshold were given in [78] for a different target.

The irradiation geometry is shown in figure 4.3. The ion penetrates the surface under normal incidence and excites the target electronic system within a cylinder of typically a few angstroms in diameter, the so–called *track core*. The final modification is called the track, while the track radius is measured from the ion impact point.

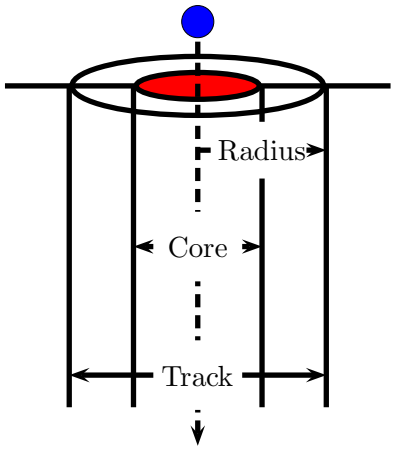

Figure 4.3: Irradiation scenario

4.7.1 Parameters

The first set of parameters, which are needed according to eq. (4.2), has the lattice heat capacity $C_p(T_P)$ and the heat conductivity $\kappa_p(T_p)$. Both parameters have been measured from 0 K up 1500 K [79] and are shown in figure 4.4 (left graph). Additionally, the lattice diffusivity according to eq. (4.26) is shown. The melting temperature of c-Si is $T_m = 1683$ K, the vaporization temperature is $T_v = 3107$ K and the atomic density is 2.23 g/cm^3 [80].

In contrast to the experimentally known lattice parameters, parameters for the electronic system are unknown. Especially the electronic density n_e of the excited electron system is needed for the heat capacity $C_e(T_e)$, the source term $S(r,t)$ and the electron–phonon coupling $g(T_e, T_p)$. In this section, the electron density is treated as a free parameter and is chosen to be $n_e = 1 \times 10^{19}$ cm^{-3}. Similar to the electron density, the electron–phonon coupling for c–Si is also unknown and will be set initially[3] to $g = 5 \times 10^{18}$ Wm^{-3}K^{-1}. In this section the effect of the coupling constant will be studied by variation of its value. The electron specific heat capacity is calculated according to eqs. (4.14) and (4.15), using the above mentioned electron density. For the electron heat conductivity, a parametric function is given in [81]

$$\kappa_e(T_e) = \left(-5.559 \times 10^{-3} + 7.122 \times 10^{-5} T_e\right) \text{ W/(cmK)} \ . \tag{4.37}$$

[3]Typical calculated values for metals range from 10^{16} Wm^{-3}K^{-1} up to 10^{19} Wm^{-3}K^{-1} [73]. So the chosen value is somewhere in the middle.

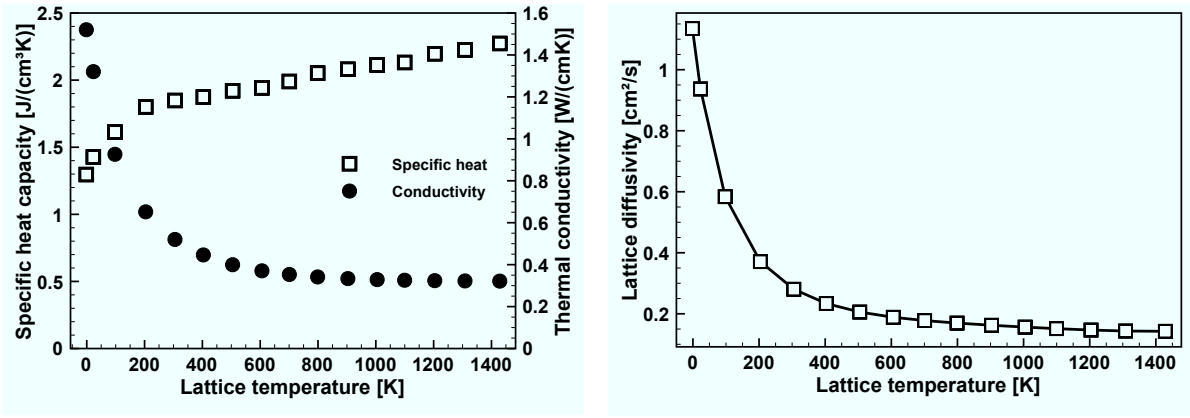

Figure 4.4: Left: heat capacity (squares) and thermal conductivity (circles) of crystalline silicon. Right: lattice diffusivity according to eq. (4.26) for crystalline silicon. Pictures reproduced from [79].

The source term is calculated according to eq. (4.6). Again the electron density enters the equation. Additionally, the ionization potential I of the target is needed. Here $I = 160$ eV is used as the mean ionization potential according to [82]. The spatial distribution $F(r)$ is shown exemplary for three different projectile energies, 1 MeV, 10 MeV and 100 MeV gold in silicon, in figure 4.5. As can be seen, eq. (4.7) predicts that most of the energy is transferred close to the ion impact point and decreases with the distance from the impact point. Additionally, a sharp kink in the radial energy distribution can be observed in figure 4.5. This critical radius is due to the fact that the electrons do not have sufficient energy to travel further. For larger energies, this kink shifts towards larger radii, while less energy is transferred close to the center. It should be noted here that $F(r)$ does not enter the TTM directly, but indirectly through a normalization (see section 4.3). Additionally, as is quite obvious, no direct connection between time and space is given by $F(r)$. This implies that no further electron impact ionization processes are considered in $F(r)$. The importance of impact ionization in Si has been noted in [83]. Finally, the stopping power S_e entering eq. (4.6) is taken from SRIM calculations [69].

4.7.2 Results: evolution of electronic and lattice temperatures

At this point, all necessary parameters for the TTM calculations are given. Exemplary results for the irradiation of 15 keV/nm Au in c–Si are shown in figures 4.6. The temporal temperature evolution for different radii from the ion impact point are shown for the lattice and the electrons in figures 4.6 (a) and (b), respectively. Furthermore, the spatial temperature distribution for different times after the ion impact for the lattice and for the electrons is shown in figures 4.6 (c) and (d), respectivly. In order to determine the radius of the modified area induced by the SHI, the I-TS assumes that the lattice temperature exceeds the melting temperature, taking the heat of fusion into account. The radius of this molten area is then assumed to be the radius of the modified area. The lattice temperature shown in 4.6 (a) exceeds the melting temperature of $T_m = 1683$ K within a radius of 1.6 nm from the point of the ion impact corresponding to a material modification with the same radius.

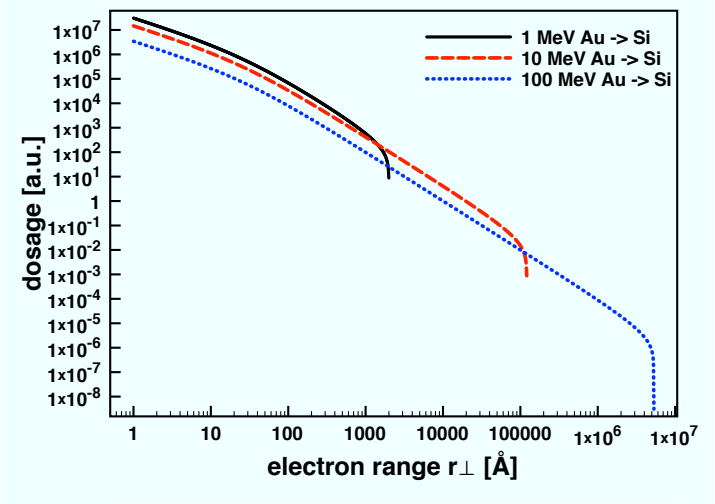

Figure 4.5: Radial electron energy distribution for 1 MeV, 10 MeV and 100 MeV gold in silicon. The deposited energy (dosage) is given in arbitrary units. The radius is given in Å and is measured perpendicular to the ion trajectory.

4.7.3 Results: track radius and damage threshold

To determine the damage threshold, calculations with different stopping powers are performed. The result is shown in figure 4.7 (left graph), where the resulting radius of the modified area, applying two different criteria, is shown versus the corresponding stopping power. The circles denote the radius of the damaged area under the assumption that the material has to be in a molten state. From this figure a damage threshold of $S_{th} = 8$ keV/nm is found. For this stopping power a molten area with a radius of 0.1 nm results.

From an experimental point of view, such modifications can be observed using for instance atomic force microscopy [59]. Such kind of experiments usually imply that the sample is irradiated under ultra–high–vacuum conditions, while the analysis is performed in a different chamber or even a different building. Thus, the initial irradiation and the final observation of the modification are well separated in time. This implies that the observed material modification leading to the damage is permanent, or exists at least on a long time scale. Therefore, one might assume, that not only the melting of the target is necessary to induce defects, but that the material has actually to be vaporized. Thus, the same calculation is performed, but instead of assuming that the melting of the target is sufficient to induce an observable modification, it is assumed that the lattice has to reach the vaporization temperature. The result is shown by the triangles in figure 4.7 (left graph). With the criterion of vaporization, the damage threshold for c–Si is $S_{th} = 25$ keV/nm. Compared to the results obtained with the melting criterion, this is an increase of the threshold by a factor of 3.

So far, all calculations were performed with a fixed electron–phonon coupling constant g. Changing the value of g will affect the calculated damage threshold. To study the effect of g on the damage threshold, a series of calculations are performed, in which the coupling constant is varied within a range from $(5 \times 10^{17} - 1 \times 10^{19})$ $\mathrm{Wm^{-3}K^{-1}}$. In order to separate the influence of the coupling constant from the effect of the damage creation criterion, below the damage threshold is determined by assuming the melting criterion. The result is shown on the right side of figure 4.7. Decreasing the electron–phonon coupling parameter leads

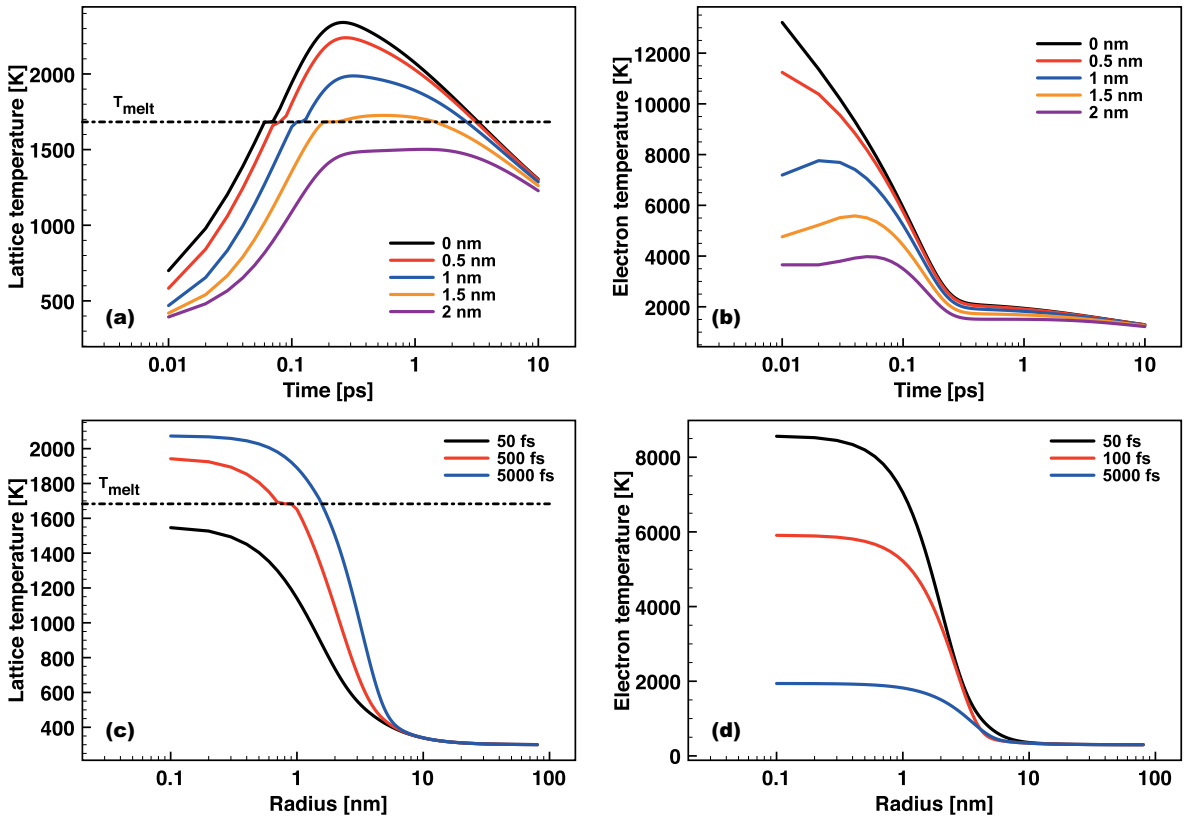

Figure 4.6: Temperature evolution for different radii from the ion impact point for the lattice **(a)** and for the electrons **(b)**. Spatial temperature distribution for different times after the ion impact for the lattice **(c)** and for the electrons **(d)**. The lattice temperature **(a)** exceeds the melting temperature T_m within a radius of 1.6 nm from the ion impact.

to an increased damage threshold. The decrease of g within one order of magnitude, from $(5 \times 10^{18} - 5 \times 10^{17})$ $\mathrm{Wm^{-3}K^{-1}}$, leads to an increase of the damage threshold from 8 keV/nm to 21 keV/nm, respectively. This is an increase by a factor of 2.6, which is very close to the factor of 3 found when changing the damage criterion from melting to vaporization. Thus, the electron–phonon coupling as well as the choice of the criterion are of equal importance when calculating the damage threshold. Next, the influence of the electron density will be studied, by variation of its value. A change of the electron density n_e leads to a change in the electron heat capacity (eqs. (4.14) and (4.15)), the electron–phonon coupling (eq. (4.27)) and in principal the heat conductivity. However, it should be noted here that the heat conductivity κ_e, as it is given by eq. (4.37), does not depend on the electron density directly[4]. Furthermore, a constant value of the electron–phonon coupling parameter $g = 5 \times 10^{18}$ $\mathrm{Wm^{-3}K^{-1}}$ is chosen. The results of these calculations are shown in figure 4.8. By increasing the electron density it is found that the damage threshold is increasing as well. This can be explained by the fact, that an increase of the density results in a larger electron heat capacity, which in turn leads to a less effective heating of the electrons by the ion's energy loss. The results presented in figure 4.8

[4]Changing the value of the electron density will change the heat capacity of the electrons. This in turn will affect the heat diffusivity in an indirect way.

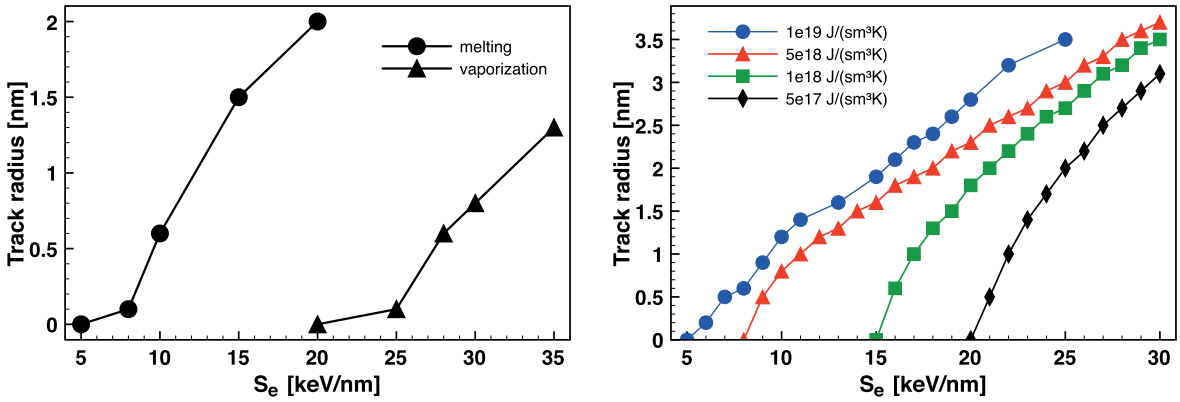

Figure 4.7: Radius of the modified area vs. the ion stopping power. Left: The electron–phonon coupling parameter was set to be $g = 5 \times 10^{18}$ Wm^{-3}K^{-1}. Circles: modification due to melting of the target. Triangles: modification due to vaporization. Lines to guide the eye. Right: The same, but for different electron–phonon coupling constants. Melting of the target was assumed as the criterion for damage. Lines to guide the eye. Figures are taken from [84].

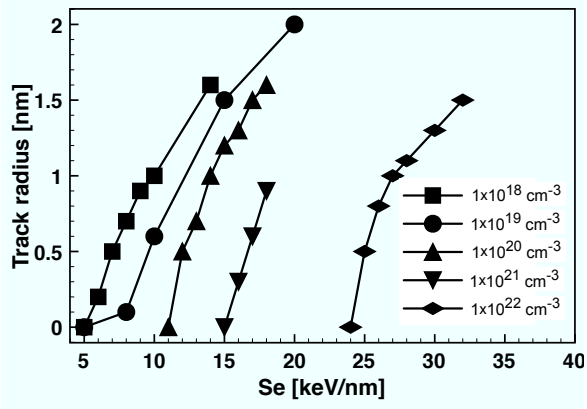

Figure 4.8: Radius of the modified area vs. the ion stopping power for different values of the electron density n_e. The electron–phonon coupling parameter was set to be $g = 5 \times 10^{18}$ Wm^{-3}K^{-1}. Melting of the target was assumed as the criterion for damage. Lines to guide the eye. Figures are taken from [84].

should be interpreted with care, since not all dependences on the electron density are included in the calculations. At this point the source term $S(r,t)$ is addressed. $S(r,t)$ is given by eq. (4.6), which implies that all electrons of the target are excited and that these electrons will be given a certain "mean" energy. One could also consider that not all energy is distributed equally among the electrons. Indeed, considering the fact, that exciting the electrons into the conduction band requires the ionization potential of the electron to be transferred and that this excitation is likely to take place from deep atomic shells, it seems that the assumption of all electrons being excited with the same mean energy is not justified. Furthermore, it was suggested in [85, 86] that the source term $S(r,t)$ can not be given as a product of the spatial and the temporal electron energy evolution.

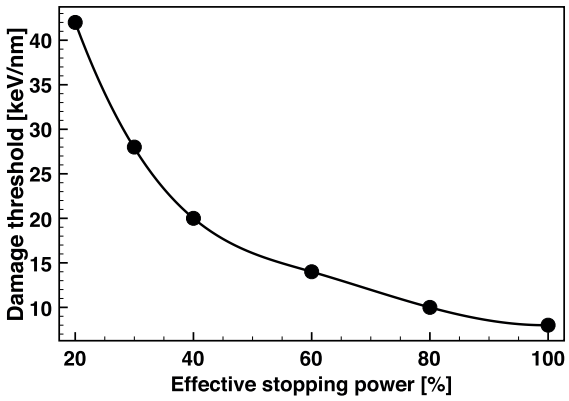

Figure 4.9: Damage threshold vs. effective stopping power. The electron–phonon coupling parameter was set to be $g = 5 \times 10^{18}$ Wm^{-3}K^{-1}. Melting of the target was assumed as the criterion for damage. Lines to guide the eye. Figures are taken from [84].

A detailed study of the electron density is not feasible using an approach like the TTM. Instead, a simpler way of studying a non–uniform energy distribution among electrons will be performed here. Such non–uniformities might be due to non–thermal, ballistic electrons. By introducing an effective stopping power[5], to account for different loss channels, like ballistic electrons, a series of calculations has been performed, in which it was assumed that only a certain percentage of the ion's stopping power is transferred directly into thermal electrons. Thus, an effective stopping power of 100 % is interpreted in such a way that the total electronic stopping power S_e is used. While 20 % means that only 20 % of the stopping power is used, so that 80 % of the stopping power is carried away far from the trajectory by δ–electrons. Again, in order to separate the different effects, the following calculations are performed using an electron–phonon coupling $g = 5 \times 10^{18}$ Wm^{-3}K^{-1} and the melting criterion. Therefore, an effective stopping power of 100 % corresponds to the damage threshold found in figure 4.7 (left graph, circles). For each effective stopping power the corresponding damage threshold is computed and shown in figure 4.9.

A reduction of the effective stopping power leads to an increased damage threshold, however, this effect is not linear. This non–linearity originates from the interplay between the transport of the electron's and phonon's energy and the electron–phonon coupling itself, which is also observed in figure 4.7. Reducing the effective energy loss from 100 % to 20 % increases the damage threshold from 8 keV/nm up to 42 keV/nm, *i.e.* by a factor of 5.25. On the other hand, decreasing the electron–phonon coupling led to an increase of the damage threshold by a factor of 3. Thus making the contribution of the effective stopping power the strongest effect studied in this work.

Considering the results of this section, it is quite obvious that the damage threshold of c–Si cannot be determined. Indeed, the unknown electron–phonon coupling is a common problem within the TTM. However, it was shown that the influence of the source term is of most significance. In order to obtain a complete picture of the damage creation due to swift heavy ion irradiation on dielectrics, a model has to be developed, which accounts for the excitation

[5] Effective stoping power does not mean that the energy loss of the ion is different. While the energy transferred per unit length is still the same, the amount of energy available for the electron–phonon coupling is effectively different from S_e.

and redistribution of electrons as well as being capable of delivering the unknown material parameters.

5 MC-TTM

The two temperature model (TTM) was introduced in the previous chapter. It has been pointed out that the application of the TTM, as it was shown, has certain disadvantages. One of these disadvantages is the fact that material parameters like the electron–phonon coupling are not known from the literature. Therefore, such parameters are often treated as fit–parameters. However, as was pointed out in the last section, the results of the TTM depend heavily on these parameters, thus estimates of physical quantities like the damage threshold can be questionable. Furthermore, as was demonstrated in the last section, non–equilibrium electrons, *e.g.* ballistic electrons, may have a strong influence on the solution of the TTM. This kind of non–equilibrium processes is completely neglected within the perviously described approach.

In this section a model will be introduced, which is based on a combination of a kinetic approach via the Monte Carlo (MC) method and a continuous approach via a TTM. This MC–TTM model is applied to the irradiation scenario 11.4 MeV/u Ca^{19+} in SiO_2.

The outline of the section is as follows: first, a general overview will be given, which also serves as the motivation for this section. Next, the Monte Carlo algorithm is explained in general terms, followed by a detailed description of the applied algorithm. In the following section the main Monte Carlo output, *i.e.* the electron energy and particle density, is presented. This is followed by an estimation of the electron diffusivity and the electron–phonon coupling, based on the Monte Carlo output. The next section describes how the Monte Carlo output can be coupled to the TTM. This is done by a detailed analysis of the electron energy distribution and conversion into a Fermi distribution. After this will be shown, that the electron specific heat capacity can be calculated using the Monte Carlo output, giving detailed information of this quantity in highly non–equilibrium conditions. Finally, the result of the performed MC–TTM combination is presented, which is then followed by the conclusions. The results presented here have been published in [71, 86, 87].

5.1 Introduction/Motivation

In this section the limitations of the implementation of TTM as explained in section 4 will be discussed. The main disadvantage is the use of the electronic temperature, requiring that the electron system is in a equilibrium state at all times. However, this assumption may not be fulfilled shortly after the swift heavy ion (SHI) impact, since the electronic excitation induced by the ion might disturb the electron distribution function. This disturbance in turn may lead to a distribution function which is no longer described by the Fermi–distribution, *i.e.* the electron system is no longer in an equilibrium. Therefore an estimate on the relaxation time of the electrons, *i.e.* the time after the ion impact at which the electrons can be described using a Fermi distribution, is necessary.

Another disadvantage within the applied TTM is the restriction that the electron transport has to be diffusive. However, after the excitation either by a SHI or a laser, high energetic electrons will be generated. These electrons may have a much larger mean free path while

traversing through the target as compared to electrons around the Fermi edge. The source term, eq. (4.6) in section 4.3, which assumes a cylindrical electron energy deposition, also neglects ballistic electrons. As high energetic, ballistic electrons travel through the target, scattering events with the target atoms will occur. These events will lead to the creation of secondary electrons and as the pathlength of high energetic electrons is large, the electron energy distribution will be broader than that assumed by eq. (4.6).

Furthermore, the density of the electrons enters the TTM through the necessary parameters. In the case of an insulator, this density is identified to be the density of the free electrons, *i.e.* electrons in the conduction band, created either directly by the penetrating SHI or indirectly due to secondary impact ionization of the target atoms by high energy electrons. The density of the free electrons is often assumed to be equal to the electron density in the valence band [61, 66, 80, 88]. The energy deposition by the SHI is so large that the atoms along the SHI path are fully ionized, so that the number of excited electrons is equal to the total number of electrons. However, away from the SHI path this is not true, in fact, the electron density will decay with increasing radius.

The electronic material parameters needed within the TTM are often difficult to come by. Most of the measurements do not reflect the transient nature of the excitation induced by a SHI or laser beam. Especially the electron–phonon coupling is difficult to obtain, as it requires good knowledge of the electron scattering rates. Due to these difficulties the material parameters are often treated as fitting parameters.

Considering these difficulties, it is evident that the early times after the SHI impact are crucial and should therefore be accounted for with great care. This can be done by applying kinetic equations as a substitute for the continuous approximations used within the TTM. However, a kinetic approach, based on the Boltzmann equation [89, 90] for instance, does not include spatial resolution so far. On the other hand a pure ballistic approach can hardly account for the electron–phonon interactions, which are believed to be essential in the understanding of the material modifications induced by SHI beams. Therefore, a combination of a kinetic approach, based on the Monte Carlo (MC) method, and the TTM is applied.

In the following, the irradiation of an insulator by a SHI is studied by applying the combination of the MC method with the TTM (MC–TTM). As a model system, the irradiation of SiO_2 by a Ca^{19+} ion with a total energy of 11.4 MeV/u is considered. Therefore, all figures are specific to this irradiation scenario, while the general scheme can be used for any SHI–insulator combination.

The results presented in this section have been obtained in a cooperation with Dr. Nikita Medvedev at the Technische Universität Kaiserslautern. While the MC calculations are performed by Nikita Medvedev, the interpretation of the data was performed in cooperation. The incorporation of the MC data into the TTM and the TTM calculations were performed by me.

5.2 Monte Carlo Method

In the present section a general introduction of the MC method will be given, which is followed by the description of the applied numerical algorithm. Finally, the main output of the MC, namely the calculated electron energy density and the electron number density, will be presented. Both the energy and number density will be used in the following sections to obtain material parameters like the electron diffusivity, the electron–phonon coupling parameter and the electron heat conductivity.

5.2.1 Description Of The Numerical Scheme

The back bone of most of the performed MC simulations is the concept of the mean free path

$$\lambda(E) = \frac{1}{N\sigma(E)}, \tag{5.1}$$

where N is the number of collision partners and $\sigma(E)$ is the total cross–section for all considered collisions,

$$\sigma(E) = \sum_i \sigma_i(E). \tag{5.2}$$

A collision free path is determined, using a random number generator utilizing the Poisson distribution. Then a random number is calculated again in order to determine what process, *i.e.* what kind of collision, is happening, according to the corresponding possibility

$$\frac{\sigma_i(E)}{\sigma(E)} = N\lambda\sigma_i(E). \tag{5.3}$$

Then, according to the chosen cross section, the particle is given a new energy, direction, state, etc.

The MC algorithm applied in this work was developed by Nikita Medvedev. Details can be found in references [91, 92] and his Ph.D. thesis. A brief summary of the algorithm is given in [87]:

"Invented decades ago, the Monte-Carlo method became one of the classical ways to describe particle transport in matter [68, 85, 93–98]. Recently, it has been used for studying excitation and relaxation of electrons irradiated with SHI or laser pulses [68, 86, 91, 92, 98, 99]. Within the method, each process occurring with each particle in the system is considered event by event. Every particle undergoes a collision process with a certain probability. The probability of a particular event depends on its cross-section relative to the total cross-section summed over all possible interactions.

Our Monte-Carlo approach, including all applied cross-sections and sampling algorithms is thoroughly described in Ref. 91. Here, we briefly recall some aspects of the algorithm, focusing on the physical background of our model. As a first step, we calculate the free paths between collisions of the incoming projectile with the target atoms; then ionization may occur for each collision, which results in the creation of the first generation of free electrons, so called δ–electrons. Secondly, we calculate the free paths between all possible subsequent collisions for all free electrons. This includes scattering on bound electrons in different energetic states and elastic scattering on target atoms. In case of an ionization event, the bound electron corresponding to the shortest possible path length is chosen and the transferred energy is calculated. Consequently, the free path and time for each of these electrons, i.e. for electrons with different energies, are also obtained. Each ionization of a bound electron is accomplished by the creation of a hole. The possibility of hole decay by Auger recombination and, thus, further creation of secondary electrons is also included in the MC simulation. In case of the elastic scattering, the energy transferred to an atom as well as the electron scattering angle are calculated. To obtain the resulting distributions of electrons and their energies, the simulations are repeated many times and finally averaged.

For simplicity, we assume perpendicular incidence, applying cylindrical geometry and periodic boundary conditions along the z–axis and neglect any nuclear stopping of the SHI. This neglection is justified for ions with energies above ~ 1 MeV/u. Since we, on the other hand,

neglect relativistic effects, the model is valid for intermediate ion energies. The projectile is assumed to have an equilibrium charge state which we describe according to the Barkas formula [65, 92, 98].

The solid is considered as a homogeneous random arrangement of atoms. Therefore, no effect like channeling or other influence of a particular material structure on particle propagation are entering the simulation. Sequential collisions of a SHI penetrating through homogeneous media is described with the Poisson law for the mean free path. For solids the corresponding mean free path can be chosen equal to the mean interatomic distance [68, 85, 95–98]. According to their energy levels, the target electrons are placed randomly around the nucleus. These target electrons are considered as not moving during the collision with the SHI. This is equivalent to a condition on the projectile velocity being much greater than the electronic Bohr velocity in the atom. The impact parameter is chosen randomly within the interatomic distance [91, 97] and the energy transfer is then calculated according to this impact parameter [91, 92]. If the energy transfer exceeds the electrons' ionization potential, this electron is considered as a free electron after collision. In the other case no energy is transferred and the electron remains bound at the atom. The scattering angle is explicitly determined by the transferred energy, and the polar angle is uniformly distributed within the interval $[0, 2\pi)$. The ionized electrons are treated as independent particles, *i.e.* the transferred energies and angles of emission of electrons are uncorrelated [68, 85, 95–98].

These resulting high-energy electrons may as well ionize target atoms. Such collisions are called inelastic collisions of free electrons with atoms in contrast to elastic collisions, which do not change the ionization state of the atoms but solely transfer kinetic energy. To calculate the mean free path for inelastic collisions of free electrons with atoms, we apply the Gryzinski ionization cross-section [98, 100], depending on the energy of the electron and the ionization potential of the bound electron. The transport and scattering of the secondary electrons, created by these ionizations, are included in the simulation in the same manner [91, 92, 99, 101].

In contrast to the penetrating SHI, excited electrons may loose kinetic energy to target atoms. We refer to these collisions as elastic collisions. Such collisions do not change the energy of the electron significantly, however, they change the direction of motion of the electron. This is especially important for electrons with a kinetic energy smaller than the bandgap of the solid $E_e < E_{\mathrm{gap}}$, since for these electrons elastic collisions are the only scattering channel. Mott's cross-section with the screening parameter by Moliere for electronic scattering [85, 91, 95, 96] is used to calculate the mean free path for the elastic collisions. This cross-section depends on the electron energy and the atomic number of the atom. The scattering angle for this collision is defined by the transferred energy, while the polar angle is uniformly distributed in the interval $[0, 2\pi)$.

Thus, in the frame of the MC approach, electrons can loose their energy due to both, elastic or inelastic collisions. The realized free path of the electrons is chosen as the shortest possible path according to Poisson's law. Thus, elastic collisions with the target atoms and inelastic collisions with bound electrons at different energy levels contribute to the mean free path [91, 92]. Additionally, low energy electrons can loose their energy due to emission of phonons [85, 95, 96] [...]. Phonon emission provides the main heating mechanism of the lattice, since the above mentioned elastic collisions of the electrons heat the atoms only slightly on the considered timescales.

Scattering among free electrons is not taken into account, since, apart from the very narrow track core, the free-electron density is much smaller than the density of valence band electrons and the density of atoms [91]. Thus, collisions with the latter two partners are the dominant

electron scattering mechanisms, determining energy transport away from the track core.

After the ionization of a target atom, a hole is created. These holes then can decay due to Auger–recombination. The Poisson law for the time of decay is applied to calculate this recombination process [91, 101]. Every atomic shell of a target atom has a characteristic Auger-decay time [102]. The electron, which is enabling the Auger-transition, and the other electron, which gains the excess energy, are chosen randomly among the bound electrons. The difference between the energy released by the filling of the hole in a deeper shell and the electrons' own ionization potential determines its final energy after the recombination. The electrons' momentum is then chosen uniformly within the solid angle. Filling of a hole by an electron from a neighboring atom, so called Knotek-Feibelman processes [103–105], are also taken into account. The characteristic time of these processes is assumed to be equal to usual Auger recombination times. As we have shown in Ref. 92, Knotek-Feibelman processes are especially important for the atoms in the close vicinity of the SHI trajectory where multiple ionizations result in a lack of own electrons of these atoms. The neighboring atoms can provide electrons for the energy release via such interatomic Auger-decays.

To determine the spatial and temporal particle and energy distributions, we follow every electron and hole and then average over the respective ensemble. Once the electrons exhibit a thermalized behavior, the MC part is considered to be finished and we switch to the TTM calculations [61, 86] [...]"

5.2.2 Monte Carlo Output

In this section the output of the MC calculation for the irradiation of SiO_2 with a Ca^{19+} ion with a total energy of 11.4 MeV/u will be presented.

Electron Energy Density

The energy density of the electrons versus the track radius for different times after the ion impact is shown in figure 5.1. It can be observed that the most energetic electrons are located within a cylinder of around 0.2 nm radius around the ion's impact point. After that the energy density exhibits a much smaller decrease. In the following the first cylinder is called zone I. Zone II is the cylinder with the radius $r\epsilon[0.2\text{ nm}, 100\text{ nm}]$. Zone III is then "the rest of the solid".

The electron energy density in each zone can be understood in the following way [91, 101].

The penetration of the primary ion leads to the excitation of high energetic ions within zone I. These so called δ–electrons traverse through the target and may collide with it, which may lead to the ionization of the target atoms and consequently to the further creation of free electrons, so called secondary electrons. These secondary electrons have less kinetic energy than the δ–electrons and are created further away from the ion impact point. The secondary electrons are created in zone II.

Both the δ– as well as the secondary electrons may then ionize other atoms, which will further increase the density of the free electrons. Finally the electrons then leave zone II. As stated above, zone III can be referred to as "the rest of the solid". The δ–electrons in this zone are moving almost undisturbed and are penetrating far into the target.

Electron Number Density

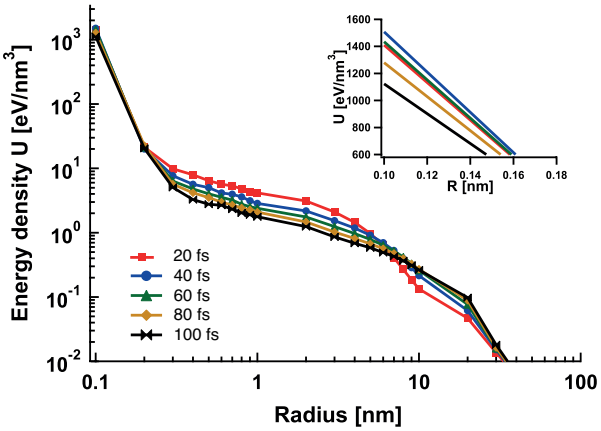

Figure 5.1: Calculated electron energy–density for different times after the ion impact. The inset shows a non–logarithmic enlargement in the center of the ion impact point. Figure taken from [87].

The electron number density, shown in figure 5.2, exhibits a similar behavior compared to the electron energy density shown in figure 5.1. Again three different zones can be distinguished. Within zone I the largest electron density can be found. This is again due to the strong excitation induced by the ion. The number density drops by almost two orders of magnitude within zone II, where electrons are predominately created by impact ionization due to collisions of δ–electrons with the target atoms. The electron number density drops down below 0.1 nm^{-3} in zone III, indicating that this zone behaves almost like a undisturbed target.

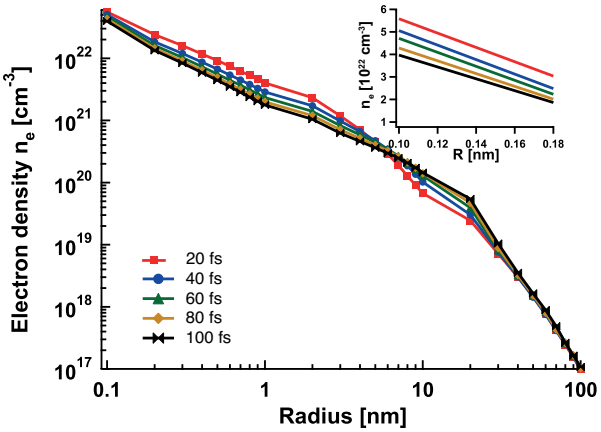

Figure 5.2: Calculated electron–density for different times after the ion impact.

Figure 5.2 quite dramatically demonstrates that the assumption of a spatially constant density as well as the assumption that the density of the excited electrons is equal to the target electron density (both often used and for example stated explicitly in [66]) is not valid.

5.3 Interpretation of Monte Carlo Method Results

In this section the output of the MC calculations will be analyzed and presented. In contrast to the Boltzmann transport equation, where the electron distribution is calculated and can directly be compared to the equilibrium Fermi distribution, the MC method calculates single electron trajectories, where the information of the electron distribution is not readily available. However, using the calculated electron density and energy transport, a criterion can be derived at which time the electron system is in an equilibrium state.

Furthermore, an estimate of the strength of the electron–phonon coupling will be given based on the MC calculations.

5.3.1 Ballistic and Diffusive Electronic Transport

The TTM assumes that the electron transport is diffusive. In this chapter, the transport behavior of the electrons computed within MC will be studied, to determine whether the assumption of a diffusive transport is valid.

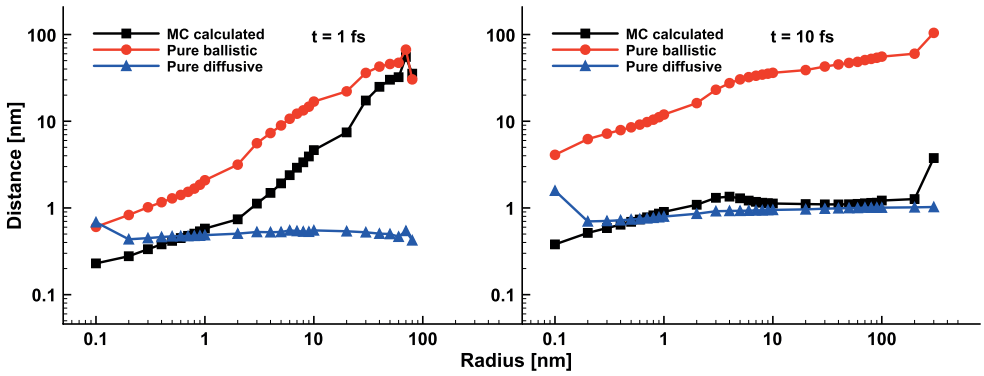

Figure 5.3: Comparison between ballistic and diffusive electron transport at 1 fs (left) and 10 fs (right) after the ion impact. The figure is reproduced from [87].

As a criteria to determine whether the electrons propagate diffusively, the following analysis is performed. For each electron at a certain radius from the ion impact point, the distance travelled Δx within the time needed for ten collision events Δt is calculated within the MC method. This is shown for the time instance of 1 fs after the ion impact on the left side of figure 5.3. Here the ordinate shows the initial position from the ion track and the abscissa the traveled distance considering ten collisions. The black squares are the results of the MC calculations.

If one assumes diffusive propagation of the electrons, then one can relate the the distance travelled Δx per time Δt with the diffusion coefficient D_e

$$D_e = \frac{\Delta x^2}{\Delta t} \Rightarrow \Delta x \propto \sqrt{\Delta t} \ . \tag{5.4}$$

Since the time interval Δt is known, eq. (5.4) can be applied to calculate the corresponding travelled distance Δx. The results are shown in figure 5.3 as blue triangulars. In the case of a ballistic transport, the electrons are propagating without a change in the direction of their

motion. Δx can be obtained using the corresponding cross–section. The results are shown as red circles.

The fastest electrons far away from the impact point are purely ballistic, while electrons close to the track show a intermediate behavior between ballistic and diffusive transport. Electrons, which are only several angstroms away from the ion impact point, were just created by Auger–decays, and thus did not have time to travel a significant distance.

The same analysis is performed for the electrons at 10 fs after the ion impact and is shown in figure 5.3 (right). Most of the electrons demonstrate already diffusive behavior at this time instance, except for the very front of the excitation. The electrons in the direct vicinity of the ion impact point are again just recently created due to Auger–recombination and thus did not travel far away. From this one can conclude that the electron transport after 10 fs after the ion impact can already be described using a diffusive model like the TTM.

5.3.2 Electron Diffusivity

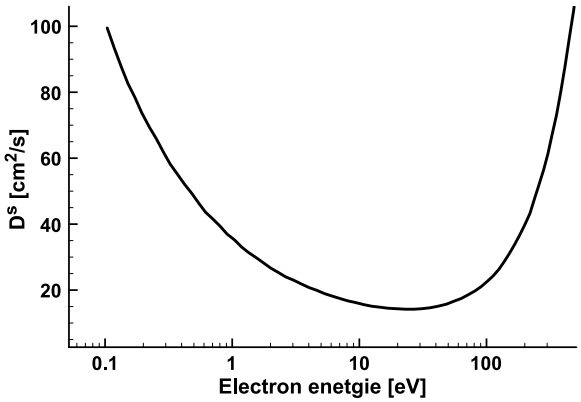

Figure 5.4: Calculated electron diffusivity versus the electron energy. The picture is taken from [71].

One of the main quantities needed within the TTM is the electronic diffusivity. One way of calculating this was shown in section 4.4.2 (eq. (4.24)), however the parameters a and b are often unknown and must either be obtained using experimental measurements or be treated as fitting parameters.

Within the MC approach a convenient way to obtain the electronic diffusivity is to use eq. (4.21) $D_e = 1/3\lambda\langle v\rangle$ where λ and $\langle v\rangle$ are the electron mean free path and velocity, respectively. Within the MC calculation individual electron trajectories are followed. Thus, the mean free path for an electron with a velocity $v(E)$ can be directly computed. The product between the electron velocity v and the mean free path λ is according to eq. (4.21)

$$D^s(E) = \frac{1}{3}\lambda v \ , \tag{5.5}$$

where the superscript s denotes the fact that $D^s(E)$ is a kind of single electron diffusivity. This quantity is shown for different electron energies in figure 5.4. $D^s(E)$ shows a linear decrease for small energies. This dependence is also observed in [61], where only electron–electron scattering is taken into account. However, within the MC approach the scattering of electrons

with the target atoms is also considered. This inclusion of the electron–atom scattering results in a minimum of the diffusivity at around 20 eV after which $D^s(E)$ is increasing again.

For the TTM calculations for SiO_2, performed by Toulemonde et al. [67, 106], the authors also linked the electron diffusivity to the electron–electron scattering, however taking only the minimum value of 20 cm^2/s into account. This value is also reproduced in figure 5.4.

As figure 5.4 only considers single particles, one has to average $D^s(E)$ with the appropriate Fermi distribution $f(E, T_e, \mu)$ to obtain the electron diffusivity $D_e(T_e)$

$$D_e(T_e) = \frac{\int_0^\infty \alpha(E) f(E, T_e, \mu) D^s(E) \mathrm{d}E}{n_e} \ , \tag{5.6}$$

where $\alpha(E)$ is the free electron density of states and n_e is the electron number density. According to eq. (5.6), the single electron diffusivity $D^s(E)$ is integrated over the single

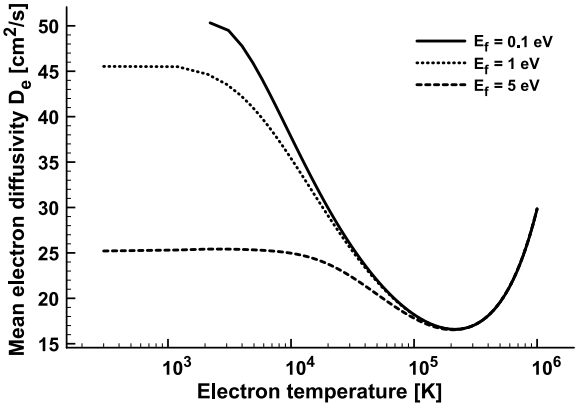

Figure 5.5: Averaged electron diffusivity according to eq. (5.6) for different chemical potentials. The figure is taken from [87].

electron energies and thus $D_e(T_e)$ will depend on the respective Fermi distribution, i.e. the electron temperature T_e and the chemical potential μ. The result of this averaging is shown in figure 5.5 for different Fermi energies, *i.e.* for different electron densities. Starting with the case for $E_F = 0.1$ eV, *i.e.* a Boltzmann gas, that the overall behavior of $D^s(E)$ is well reproduced. With increasing μ the behavior of $D_e(T_e)$ deviates more and more from $D^s(E)$ for low electron temperatures. This difference stems from the fact that at low temperatures and positive chemical potentials electrons are in a degenerate state and high energy contributions of $D^s(E)$ are truncated by the Fermi edge. Consequently, this effect recovers for sufficient large T_e, where ultimately the chemical potential becomes negligible, i.e. the electrons are fully non–degenerated. Equation (5.6) is evaluated According to the local density calculated using the MC method (see figure 5.2) and the corresponding chemical potential μ and electron temperature T_e at each space point.

5.3.3 Electron–Phonon Coupling Parameter

As was mentioned in section 4.6, the energy transferred from the electrons to the lattice is determined by the electron–phonon coupling parameter g. In principal g can be obtaind by evaluation of eq. (4.27). However, this requires the knowledge of the scattering rate τ, which is

often unknown. One approach to estimate the electron–phonon coupling is to use experimental data as a boundary condition [61, 67, 106, 107].

However, a more direct computation of the electron–phonon coupling parameter is possible within the MC method. In principal g stands for the amount of energy transferred to the lattice by the electrons ΔE, per unit time t and per unit volume V. The energy transfer between electrons and the target atoms is computed in the MC simulations within the binary approximation and therefore directly included. For the estimation of the time unit, one single atom can be considered and the time between two electron collisions can be measured. Finally, since single trajectories are followed, the volume can be identified as the volume of this one atom. Doing so the electron–phonon coupling was estimated to be on the order of 10^{18} $\mathrm{J{\cdot}(sm^3K)^{-1}}$ [71].

It should be noted that the electron–phonon coupling was obtained using purely classical considerations. Therefore no quantum effects are included.

5.3.4 Auger decay

The ionization of target atoms by the penetrating ion leads to the creation of free electrons. However, the creation of a free electron is accompanied by the creation of a hole. Depending on, from which energy level of the atom the electrons are removed, these holes are created in different atomic shells. The holes may then decay radiatively, or due to intra– as well as inter–atomic Auger processes, thus changing the energy distribution of the holes. Holes are not only created by the ionization of the target atoms due to the primary ion, but also due to impact ionization caused by the δ–electrons. Such impact ionization processes lead to the creation of holes and free electrons even at times much larger than the interaction time of the incoming ion with the target atom.

The decay of a hole due to Auger decay leads to an increase of the electron energy density, as the excess energy is transferred to another electron, which is then excited into the conduction band. Therefore one may say that the decay of holes acts as an additional energy source for the electrons. In fact, it was found in [71], that almost 82 % of the energy loss experienced by the ion is stored in holes. However, the decay of holes is not an instantaneous process, as the energy stored in the holes can not simply be added to the initial electron energy.

The emission of individual electrons due to the decay of individual holes is included within the MC method, while it is impossible to include this process within the TTM calculations. A first approximation to include the increase of the electron energy density due to Auger decay of holes can be done by introducing an additional sourceterm S_h for the electron heat diffusion equation (4.4),

$$S_h(\vec{r},t) = E_h(\vec{r}) \cdot \left(1 - e^{-t/\tau}\right) \quad , \tag{5.7}$$

where $E_h(\vec{r})$ is the hole energy density at the point $\vec{r}$ and τ is a characteristic hole decay time. Equation (5.7) assumes an exponential decrease of the hole energy, which is governed by a decay time τ. The general idea is that deep shell holes, such as K or L holes, will decay due to Auger decay. For each Auger decay the hole is promoted energetically upwards the valance band, while simultaneously an electron per Auger decay is emitted into the conduction band. However, for every single auger decay one additional hole in an energetically higher shell is created. This is called the Auger–cascade. While the individual Auger decay from one shell to another shell is a fast process, the entire cascade requires more time.

For the calculations presented here a decay time of $\tau = 100$ fs was used in accordance to [108, 109].

5.4 Conduction Band–Fermi Distribution

As already mentioned, the irradiation of insulators with SHI results in the creation of free electrons. The creation and the following evolution of these free electrons is calculated within the MC model as was described above. Furthermore, in section 4.4 the fundamental idea was presented of excited electrons in an insulator behaving like free electrons in a metal. According to this idea the free electrons calculated within the MC method are then to be described by a pseudo Fermi distribution $f^*(E, T_e, \mu)$. Next it will be described how the pseudo Fermi distribution can be obtained.

Within the MC method the electron is characterized by its coordinate and velocity, while the velocity defines the electrons kinetic energy. Within the TTM the electron system is described by a temperature. Consequently, in order to define the electron system within the TTM, one may calculate the energy density U of the electrons obtained from the MC simulation and convert that into an electronic temperature via the specific heat capacity at constant volume C_V, as was shown in section 4.4.1. However, C_V is unknown for insulators and especially for insulators during SHI irradiation. Again one may use eq. (4.14) or the high temperature limit eq. (4.15), however, neither the Fermi energy E_F nor the temperature, at which the high temperature limit is valid, are known. A direct computation of the electron temperature seems to be the best choice.

5.4.1 Obtaining The Pseudo Fermi Distribution

Assuming that the electrons are in a local equilibrium and are well described by the thermodynamic equations. Then the electron temperature is defined by the Fermi distribution,

$$f(E, T_e, \mu) = \frac{1}{1 + \exp[(E - \mu)/k_B T_e]} \ , \tag{5.8}$$

where k_B is the Boltzmann constant and μ the chemical potential.

Since neither the electron temperature nor the chemical potential are known, these two unknown variables must be determined first. This can be done by exploiting the zeroth and the second moment of the Fermi distribution with respect to the energy E.

The zeroth moment represents the electron particle density

$$n_e \ = \ \int_0^\infty \alpha(E) f(E, T_e, \mu) \mathrm{d}E \ , \tag{5.9}$$

while the second moment over the Fermi distribution yields the electron energy density,

$$U \ = \ \int_0^\infty E \cdot \alpha(E) f(E, T_e, \mu) \mathrm{d}E \ , \tag{5.10}$$

where $\alpha(E)$ is the free electron density of states.

The particle density n_e as well as the energy density U are both known from the MC calculation as is shown in figures 5.2 and 5.1, respectively. Apparently n_e and U have to be identified as local particle and energy densities.

The particle density n_e prescribed by the MC simulation can be used as a boundary condition for eq. (5.9). Variation of μ and T_e, under the given boundary condition, leads to a relation $\mu(T_e)$. The same procedure is repeated for eq. (5.10), taking the energy density U as the boundary condition.

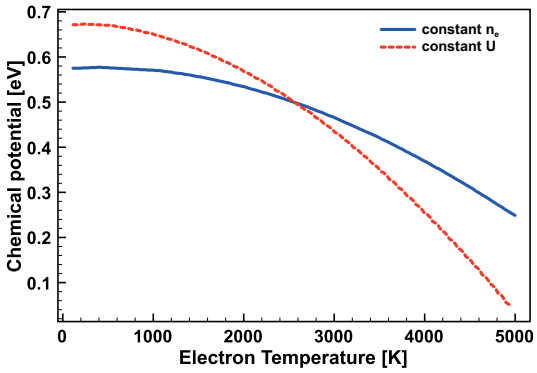

Figure 5.6: Temperature dependence of the chemical potential μ evaluated from eq. (5.9) and (5.10). Calculations have been performed at an arbitrary radius from the ion impact point.

Figure 5.6 shows the results of the above mentioned calculations for exemplary values for the electron density $n_e = 2 \times 10^{21}\text{cm}^{-3}$ and an electron energy density $U = 160$ Jcm^{-3}. For both equations (5.9) (blue curve) and (5.10) (red curve), a respective independent $\mu(T_e)$ function is obtained. Although the particle and energy density are treated here as independent quantities, both are related to the same physical electron ensemble. Therefore, both functions $\mu(T_e)$ have to be evaluated exactly at the point, where both functions intersect. This way, the electron ensemble characterized by n_e and U can now also be characterized by its chemical potential μ and the electron temperature T_e. The intersection point (μ, T_e) is an uniquely defined point, as both functions as well as their first derivatives are monotonically decreasing.

Since the energy and particle density are functions of the radius, the calculations have to be performed for all radii.

The calculations performed here have two purposes. First, the electron energy density U is transformed into the corresponding electron temperature T_e. Furthermore, the pseudo Fermi distribution $f^*(E, T_e, \mu)$, belonging to the electron ensemble at each distance from the ion impact point, can be obtained for any given time instance.

Furthermore it should be noted here, that these calculations also serve as zero–order criteria for the thermalization of the electron ensemble. Within the MC simulation the energy and particle density can be extracted at any chosen time instance and space point. However, it is not necessarily the case that the electron system at that precise time instance and space point have established a fermi distribution. As a consequence, if no intersection point for eqs. (5.9) and (5.10) is found, this indicates that the distribution function does not reassemble a Fermi distribution and thus no electron temperature is defined. Similarly, if the intersection point yields unphysical values like negative temperatures, this results also in an undefined electron temperature.

Numerically eqs. (5.9) and (5.10) can be solved quite straight forward. The integration is performed using a Romberg integration routine as is implemented in the GSL library.

5.4.2 From Thermalization To Electronic Temperature

The routine described in the previous section is then used to calculate the electron temperature corresponding to the electron number density and energy density, respectively, calculated within the MC approach as shown in figures 5.2 and 5.1. The temperature is calculated for different radii between 0.1 nm and 10 nm and for different times after the ion impact.

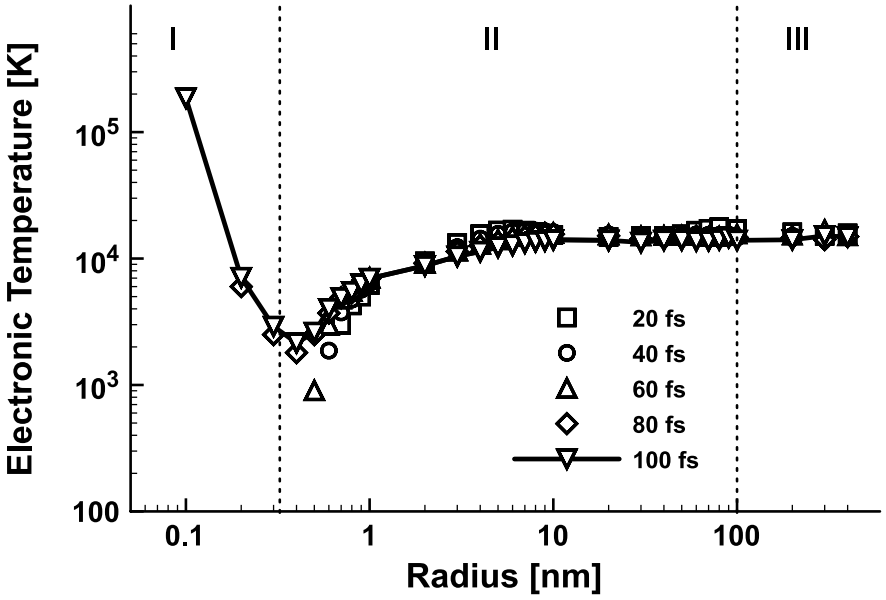

Figure 5.7: Calculated electronic temperature along the lateral track radius for different times after the ion impact, evaluated from equations (5.9) and (5.10). The solid line is a eye guide only.

The results of the calculations are shown in figure 5.7. Focusing first at $t = 20$ fs (squares) after the ion impact. It can be seen that for track radii larger than 0.7 nm electron temperatures of a few thousand Kelvin are calculated. However, for radii smaller than 0.7 nm no temperature is defined, since the calculated values of μ or T_e are not physical. For the time of 40 fs (circles) it is observed that for radii larger than 0.6 nm an electron temperature is defined. A similar behavior as that for 20 fs is observed, but with somewhat elevated temperatures within 0.2 nm and 2 nm, while the temperature decreases for radii larger than 2 nm. It is again impossible to define a temperature for radii smaller than 0.6 nm. Repeating the calculations for the time of 60 fs (triangular) again shows a similar behavior for radii larger than 0.5 nm. By the time of 80fs (diamonds, solid line in figure is a eye guide) however, a temperature is found for the entire interval. This indicates that only by a time of around 80 fs the electron state is characterized meaningfully by a temperature, and thermodynamical equations like the TTM can be safely applied.

Therefore at a time of around 80 fs - 100 fs the TTM can be applied, as by that time a temperature can be defined for the entire track.

Three zones can be found in figure 5.7. Zone I is located around the track core with a radius of about 0.2 nm. Within this zone the electrons are predominantly heated by Auger recombination, leading to a continuos energy deposition into the electron system in that zone, and thus an elevated electronic temperature compared to the rest of the track is observed. However, one has to keep in mind that the decay of holes and the related energy deposition into the electron system result in the fact, that "new" secondary electrons are constantly created and thus act as a perturbation of the electron Fermi distribution.

Zone II starts from 0.2 nm and reaches up to around 100 nm and is populated by mainly low energetic secondary electrons, created by impact ionization induced by the δ–electrons. Unlike secondary electrons created in the first zone, these secondary electrons have a much smaller kinetic energy. Electrons in this zone have a much lower energy and are therefore described by a lower temperature.

Finally, zone III is populated by electrons originating from within the first two zones. These electrons move through the solid and remove energy from the track.

Figure 5.7 should be interpreted as a set of snap–shots of the electron energy distribution due to impact ionization and Auger recombination processes, rather than a temperature profile. It is quite obvious that it is impossible to model the energy transport profile shown in figure 5.7 using a diffusive, hence a thermal approach. The solution of a diffusion equation is an exponential in space with a certain characteristic length. Obviously, the function shown in figure 5.7 is far from being an exponential. The increase of the energy/temperature after the minimum stems from the fact that high energetic electrons create secondary electrons through impact ionization.

The electron temperature computed in the center of zone I at 80 fs is on the order of 10^5 Kelvin and is more than one order higher than compared to the other zones. Estimations of the electron temperature on the order of 10^5 Kelvin after SHI irradiation, either by calculations or interpretations of measured electron energies [110], are often found in the literature. However, figure 5.7 indicates that such high electronic temperatures are only established within a very small zone close to the ion impact point. The majority of the electrons within zone II and III have temperatures of a few thousand Kelvin, as is often observed or calculated for the case of laser irradiation of solids.

If one assumes that the electrons are thermalized at all times, then the calculation of the electron temperature via the moments of the Fermi distribution, (5.9) and (5.10), is not necessary. In that case, one can relate the energy density of the electrons U with the electron number density n_e and the electron temperature T_e via

$$\begin{aligned} U &= \frac{3}{2} n_e k_B T_e \\ \Leftrightarrow T_e &= \frac{2}{3} \frac{U}{n_e k_B} \ . \end{aligned} \tag{5.11}$$

However, this is only true for Boltzmann distributed electrons. Thus, for eq. (5.11) to be valid, the following relation between the electron temperature and the chemical potential has to be fulfilled

$$T_e \gg T_F = \frac{E_F}{k_B} \ . \tag{5.12}$$

Here the chemical potential μ is calculated using eqs. (5.9) and (5.10), as is presented in section 5.4.1. The temperatures obtained using both methods can be directly compared. This comparison is shown for 20 fs, 60 fs and 100 fs after the ion impact.

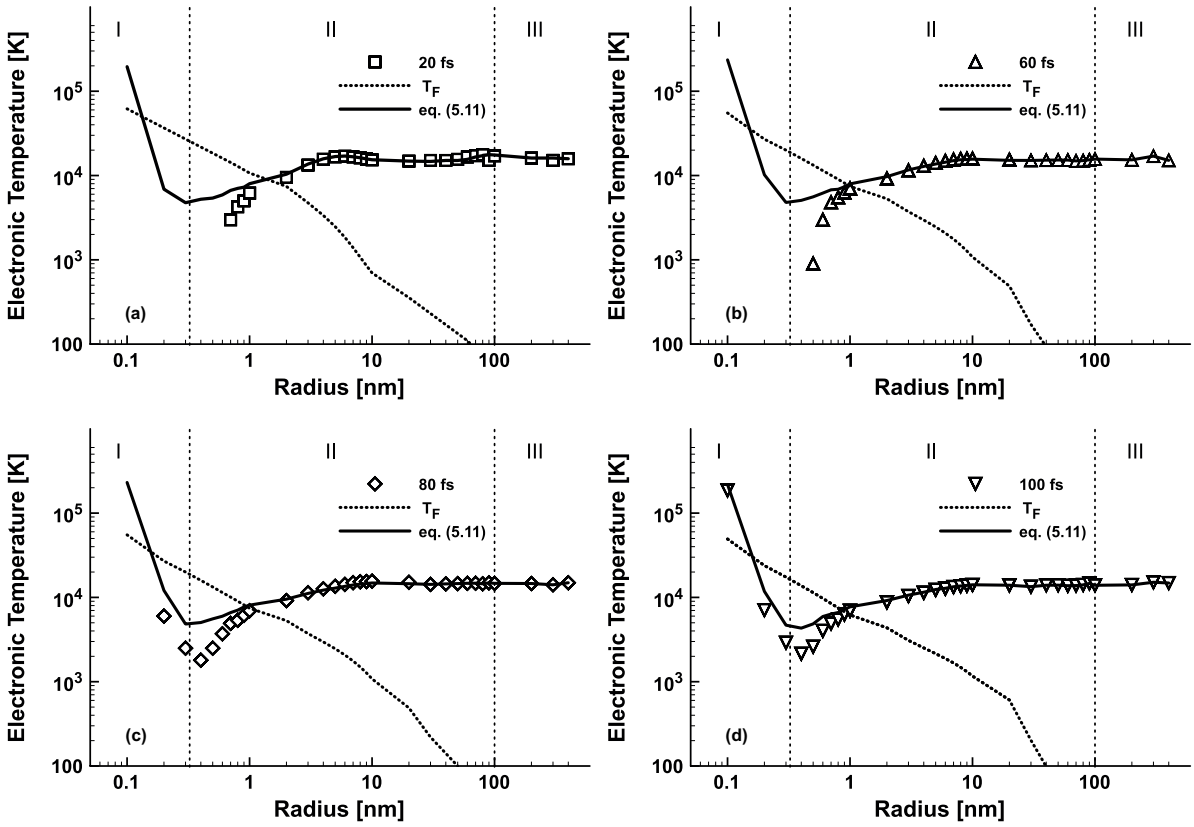

Figure 5.8: Electron temperature for different radii 20 fs (a), 60 fs (b), 80 fs (c) and 100 fs (d) after the ion impact. Symbols: calculations according to eqs. (5.10) and (5.9). Line: equation (5.11). Dotted line: E_F/k_B

Figures 5.8 (a)–(d) show the temperatures obtained using eq. (5.11) (straight lines) and the extracted temperatures using eqs. (5.9) and (5.10) (symbols). For radii larger than around 1 nm it is found that both methods give the same temperatures. However, for times shorter than around 80 fs–100 fs no temperatures can be defined in the near vicinity of the ion impact point using the moments of the Fermi distribution. In contrast to that, eq. (5.11) does result in a temperature in that area. As was mentioned above, the temperatures obtained by evaluating eq. (5.11) are only physically meaningful, if $T_e \gg T_F = E_F/k_B$ is true. The Fermi temperature T_F is given as the dashed lines in figures 5.8 (a)–(d). It can be seen that the temperatures do not agree, exactly in that area, where $T_e \gg T_F$. Close to the ion impact point, T_F is larger than the temperature predicted by eq. (5.11) and thus can not be applied here. A peculiar case is shown in figure 5.8 (c) and (d), where both methods yield a electron temperature. Although both temperatures exhibit a similar behavior, eq. (5.11) gives a larger temperature compared to the temperature obtained using the moments over the Fermi distribution. Again, this difference is explained by the fact that electrons in that area are degenerated, i.e. $T_F \gg T_e$. Consequently, the chemical potential μ must change its sign, *i.e.* positive where $T_F \gg T_e$ and negative for $T_F \ll T_e$. This is shown in figure 5.9 for the case of 100 fs after the ion impact. Here, the left axis shows the chemical potential μ (red), while the right axis is the electron temperature. The dashed line shows the zero chemical potential

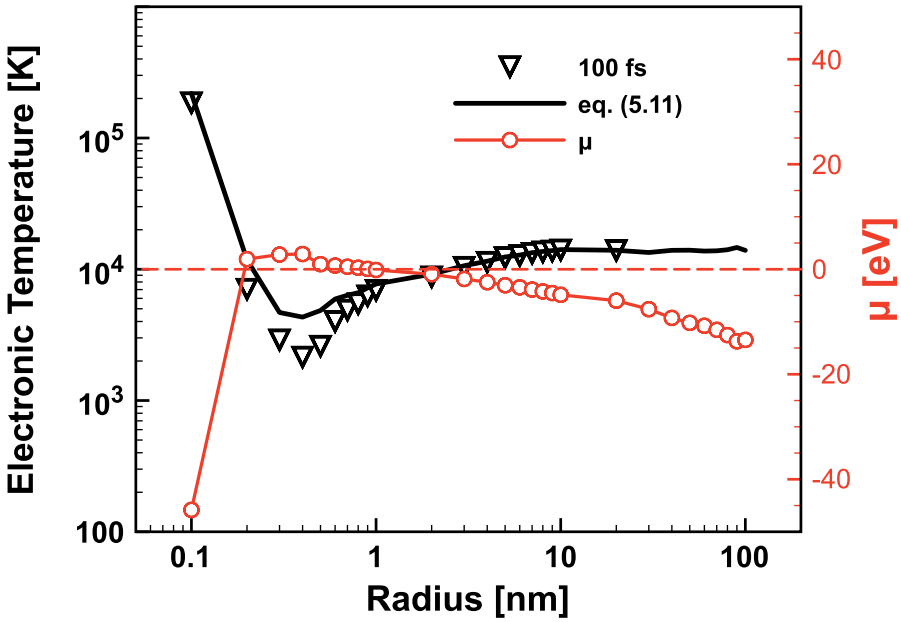

Figure 5.9: Calculated electronic temperature along the lateral track radius for $t = 100$ fs after the ion impact. Triangle: equations (5.9) and (5.10). Solid line: eq. (5.11). Circles: Calculated chemical potential μ. Dashed line: $\mu = 0$ eV.

and the solid line is eq. (5.11). Finally, it can be seen from the comparison between figures 5.8 (c) and (d), the difference between the two methods decreases with later times.

From figures 5.8 (a)–(d) it is found, that electrons in the near vicinity of the ion impact point exhibit a strong degenerate character. Thus it appears reasonable, to describe these electrons in a similar manner to eq. (5.11) but taking into account, that $T_F \gg T_e$. This can be done with the help of the so called *Sommerfeld–expansion*

$$U = \frac{3}{5} n_e E_F \left(1 + \frac{5}{12} \pi^2 \left(\frac{k_B T_e}{E_F} \right)^2 + \dots \right) \quad , \quad T_e \ll E_F / k_B \quad . \tag{5.13}$$

Equation (5.13) is shown for the exemplary case of 100 fs in figure 5.10. Evidently, eq. (5.13) (dash–dotted line) predicts quite well the electron temperature for radii from 0.3 nm up to 0.7 nm, while the classical approximation fails in this area. Again, the reason is that in this area the electron gas is degenerated. In the area where the electron temperature is comparable to the Fermi temperature (around 1 nm from the ion impact point) both approximations fail. In conclusion, it is found that eq. (5.11) can only be used far away from the ion impact point, where the electron density is low and the Fermi distribution equals its Boltzmann tail, while eq. (5.13) is only valid for small radii near the ion impact point.

Figure 5.10 suggests, that for a quick estimation of the electron temperature eqs. (5.11) and (5.13), together with the knowledge of the Fermi temperature T_F. If both equations yield $T_e \gg T_F$, implies that eq. (5.11) has to be used and vice versa. As mentioned above, this simple estimation of the electron temperatures breaks down if the electron temperature is comparable to the Fermi temperature.

The numerically more challenging approach to compute the electron temperature via the moments of the Fermi distribution (eqs. (5.9) and (5.10)), however gives a reliable estimate,

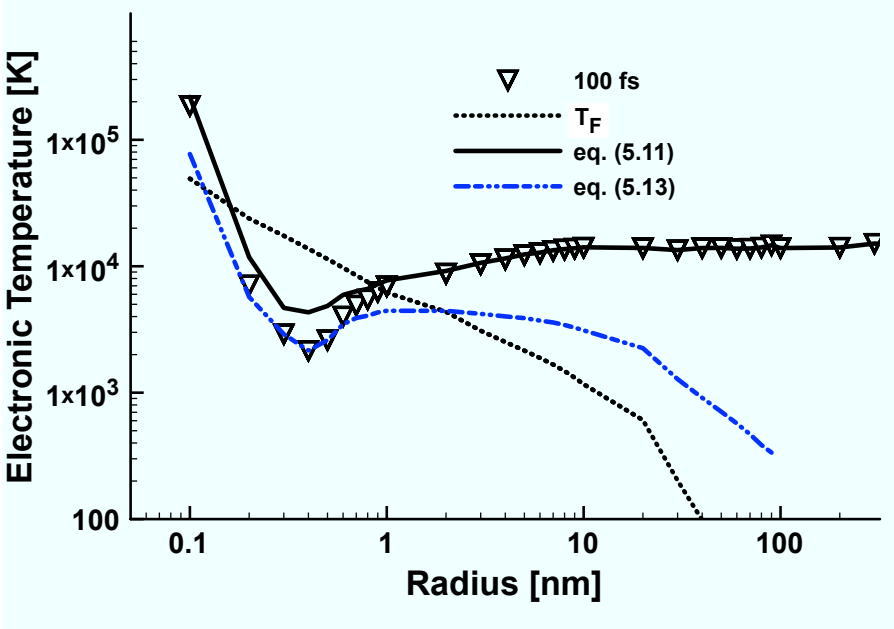

Figure 5.10: Calculated electronic temperature along the lateral track radius for $t = 100$ fs after the ion impact. Symbols: equations (5.9) and (5.10). Solid line: eq. (5.11). Dotted line: E_F/k_B. Dash–dotted line: eq. (5.13).

whether the electron system is in equilibrium, and the resulting electron temperature for all electron energy and number density combinations.

5.5 Electron Heat Capacity

In the previous chapter it was shown how, using both moments of the Fermi distribution with respect to the energy, the chemical potential μ and and the electron temperature T_e can be calculated. Each of these pairs (μ, T_e) are related to the electron ensemble at a certain time t after the ion impact and a certain radius from the impact point r. The pair (μ, T_e) can therefore be labeled $(\mu, T_e)\,|_{t,r}$. With this pair, a Fermi distribution is defined for all radii r and all times t, where μ and T exist. With the knowledge of the Fermi distribution, thermodynamical quantities like the electron heat capacity at constant volume C_V can be calculated,

$$C_V = \frac{\partial U}{\partial T_e} \approx \frac{\Delta U}{\Delta T_e} \ , \tag{5.14}$$

describing C_V as the ratio of an energy increase ΔU, induced by a temperature increase ΔT_e. To obtain the energy increase ΔU, eq. (5.10) can be evaluated under the condition $T_e = T_e' + \Delta T_e$, where T_e' is the electron temperature corresponding to the internal electron energy U. However, this requires the knowledge of the temperature dependent chemical potential $\mu(T_e)$. Assuming that the particle density remains constant during this energy increase, $\mu(T_e)$ can be calculated from eq. (5.9) resulting in the curve shown in fig. 5.6. Consequently, C_V depends on the electron density n_e, which is a function of the radius. On the left side in figure

5.11 the electron heat capacity at an arbitrary time instance and space point is illustrated. The graph labeled $C_{V,MC}$ represents the full temperature dependence of the heat capacity, calculated using eq. (5.14); additionally the low temperature limes, $\gamma \cdot T_e$ (eq. (4.14)), and the high temperature limes according to the high temperature limit, eq. (4.15), are shown.

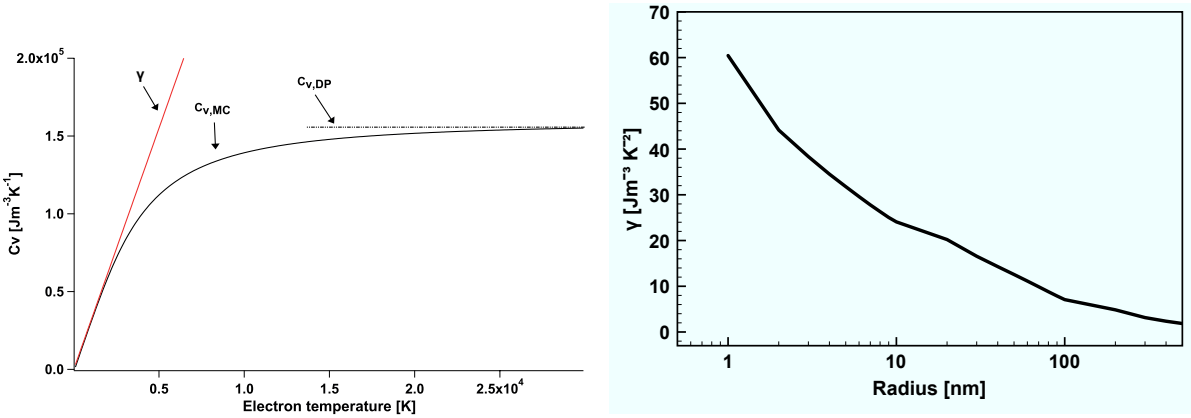

Figure 5.11: Left: Calculated electron heat capacity at constant volume versus electron temperature ($C_{V,MC}$). The dashed line is the value according to the high temperature limit ($C_{V,DP}$), while the straight line is $\gamma \cdot T_e$. Right: γ –factor for different radii from the ion impact point at a time instance of 80 fs after the ion impact.

As was explained earlier in section 4.4.1, the low temperature limes of the specific heat capacity is proportional to the electron temperature T_e. This proportionality is often used within TTM calculations. On the right side of figure 5.11, the γ–factor is calculated for different radii from the ion impact point at a time instance of 80 fs after the ion impact. With increasing radius the γ value decreases by almost one order of magnitude within an interval of 10 nm. This strong variation of γ stems from the large gradient in the electron density n_e calculated within the MC method (see figure 5.2).

The calculated temperature dependent electron heat capacity for different electron densities is shown in figure 5.12. The electron densities are corresponding to different radii from the impact point of the ion, according to figure 5.2, thus the electron heat capacity becomes a spatially dependent quantity. For the sake of readability only the values for the first 0.8 nm are shown, as C_V is decreasing quite strongly for larger radii. However, this figure demonstrates that the assumption of a spatially constant electronic heat capacity is not valid. The value of C_V ranges from some 10 kJ/m^{-3}K^{-1} up to 1000 kJ/m^{-3}K^{-1} within 1 nm of the track for the irradiation scenario studied here. Furthermore, assuming a temperature independence or simple proportionality appears not valid either, since the electron temperatures are not in the $C_V \propto T_e$ regime as the comparison of figures 5.7 and 5.12 reveals. In general, since the evolution of the electron temperature is calculated within the TTM, the entire temperature interval has to be considered. Assuming $C_V \propto T_e$ underestimates electron temperatures in the case of high electron energies appearing mainly in the center of the track.

For comparison, the electronic heat capacity for gold, calculated using the electron density of gold, is added in figure 5.12. The irradiated SiO_2 demonstrates a heat capacity that is quite comparable to that of gold at small distances from the ion impact point. However, within 0.4 nm the C_V of the irradiated SiO_2 drops to around halve the value of gold. Therefore,

speaking in terms of the electron heat capacity, the irradiated insulator exhibits a "metallic" character. This "metallic" character is confined to a small region close to the ion impact point. It should be noted here that the energy of the penetrating ion is just above the damage threshold for SiO_2, hence only a small modification can be observed. The area at which the insulator shows such "metallic" properties will increase with increasing energy of the primary ion. The large spatial variation of the electron heat capacity again originates from the large electron density gradient. Allowing the electron density to equilibrate this gradient within the TTM will result in a smoother spacial dependence of the electron heat capacity. See the outlook in section 6.1 for details.

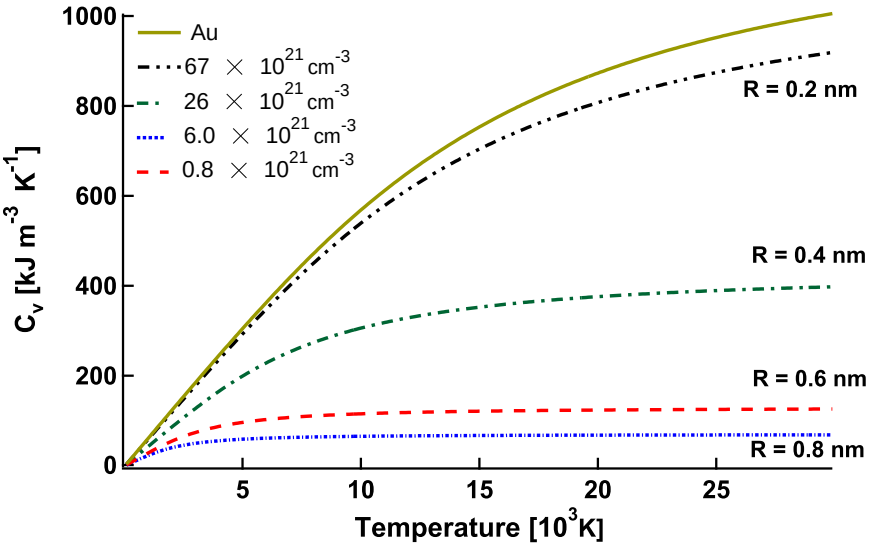

Figure 5.12: Temperature dependent electron heat capacity for different electron densities corresponding to different track radii. The solid line shows the electron heat for Au.

5.6 TTM Calculation

In order to compute the lattice temperature evolution, the TTM is used taking the MC output into account. This includes the electron–phonon coupling parameter g, the temperature dependent electron diffusivity $D_e(T_e)$, the electron density n_e and the temperature dependent electron heat capacity $C_V(n, T_e)$. With the exception of the electron–phonon coupling parameter, all mentioned quantities are spatially dependent. Furthermore, the MC method provides the initial conditions for the TTM calculations. These initial conditions are related to the electron energy density at a chosen time instance. The time at which the TTM is started is chosen to be 100 fs after the ion impact, since it was shown in a previous section (section 5.4.2) that the electron gas can be assumed as thermalized at approximately that time. The electron energy density, the lattice energy density as well as the energy stored in holes resulting from the MC calculations at the time instance of 100 fs after the ion impact are shown in figure 5.13. The electron energy as well as the lattice energy density are used directly as initial conditions for the respective subsystem, while the hole energy is used as a source term for the electron system (eq. (5.7)), as was explained in section 5.3.4.

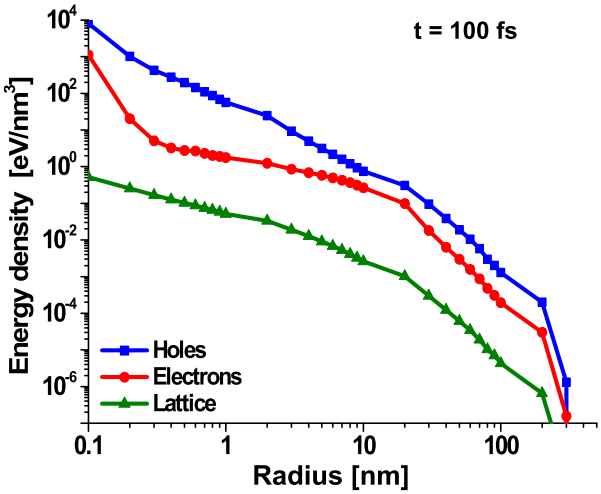

Figure 5.13: Calculated energy–density for electrons, holes and the lattice 100 fs after the ion impact. The energy–densities are used as initial conditions for the TTM calculation.

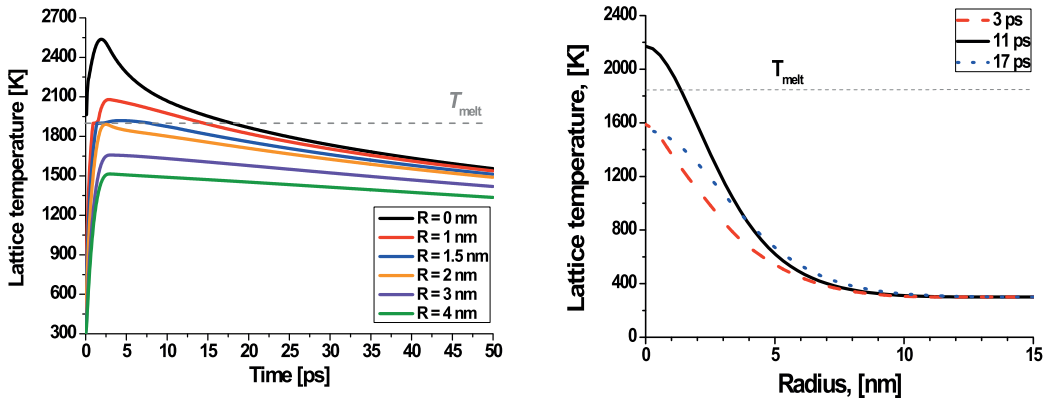

Figure 5.14: Left: The temporal lattice temperature evolution shown at different radii from the ion impact point. Right: The spacial lattice temperature evolution for three different times after the ion impact. T_{melt}=1830 K is the melting temperature of SiO_2

For the numerical implementation, both equations (4.1) and (4.2) are solved using the finite differences method. The input provided by the MC method includes the electron energy density, the lattice energy density, the energy stored in holes (figure 5.13), the electron–phonon coupling parameter g (see sec. 5.3.3), the electron diffusivity $D_e(T_e)$ (sec. 5.3.2) and the electron specific heat capacity $C_V(T_e)$ (sec. 5.5). All these input parameters are spatially dependent and are given at discrete spatial points. The MC output is interpolated using a linear interpolation scheme. The criterion to induce any material modifications due to thermal melting is that the melting temperature T_{melt} (1830 K for SiO_2), plus at least the latent heat of fusion (50 kJ/mol), has to be reached at least. Both values are taken from [111].

Figure 5.14 shows the lattice temperatures, as resulting from the TTM calculation using the MC data as input. On the left side, the temporal lattice temperature evolution for different radii from the ion impact point is shown. The black line shows the lattice temperature at

the center of the track. At the time[1] $t = 0$ the lattice temperature is already elevated to around 1900 K. This is due to the energy transfer accompanied by the electron–atom collisions calculated within the MC model. The lattice temperature then increases due to electron–phonon interactions until the maximal temperature is reached at around 5 ps, after which the temperature decreases again. The red curve indicates the lattice temperature at 1 nm from the ion impact point. The initial temperature at this space point is much smaller compared to that at 0 nm. The lattice temperature increases until the melting temperature is reached at which it remains constant, while the additional energy increase is used to overcome the latent heat of fusion. Afterwards the temperature increases further, until, after a maximum is reached, it decreases again. A similar behavior can be observed for the temperature evolution at a distance of 1.5 nm from the ion impact point, albeit with a lower peak temperature. The temperature evolution at 2 nm is different from that for smaller radii. The temperature is increasing until the melting temperature is reached. However, the energy increase is not sufficient to overcome the latent heat of fusion, so that the temperature does not raise higher than the melting temperature. For radii larger than 2 nm the temperature does not reach the melting temperature at all. Within the TTM it is assumed that the area, in which the lattice temperature exceeds the melting temperature, can be identified as the damage area induced by the SHI. From figure 5.14 it is found that the lattice is molten within an area of 3.3 nm in diameter. Experimentally the modification for a very similar irradiation scenario was measured to be 2.96 nm [88]. This agreement is more than satisfactory considering that no fitting was involved in the calculations. The differences in the measured and calculated modification may be due to the fact that no actual lattice modifications, in the sense of atomic motions, are considered within the TTM applied here. Therefore, the diameter calculated within the TTM serves as a lower limit.

5.7 Conclusion

In summary, the developed combination of the Monte Carlo method with a two temperature model (MC-TTM) is well capable of analyzing the temporal and spatial behavior of excited electrons in dielectric targets, as wall as the lattice temperature evolution governed by electron–phonon interactions. The model is well suited to predict the size of track induced by a swift heavy ion. Within the MC part of the calculations, important material parameters like the electron–phonon coupling, the electron diffusivity and the electron heat capacity can be calculated. These quantities are essential within the TTM description and are experimentally often unknown. In this section, the irradiation of SiO_2 with a Ca^{19+} ion with a total energy of 11.4 MeV/u was studied exemplary. Within the analysis, it was found that the electron specific heat capacity for irradiated SiO_2 reveals a strong transient increase of the electron heat capacity located around the track core. The specific heat capacity is compared to the electron heat capacity of gold.

It was observed that a temperature of electrons can not be defined in the presented scheme for a time shorter than around 80 fs–100 fs. This demonstrates that the TTM can not be used prior to that time and that the electron dynamics have to be calculated using a kinetic approach.

The spatial and temporal electron energy and particle density computed within the MC are

[1] The starting point for the TTM calculations is actually at 100 fs after the ion impact. Here the time of the TTM calculations is counted.

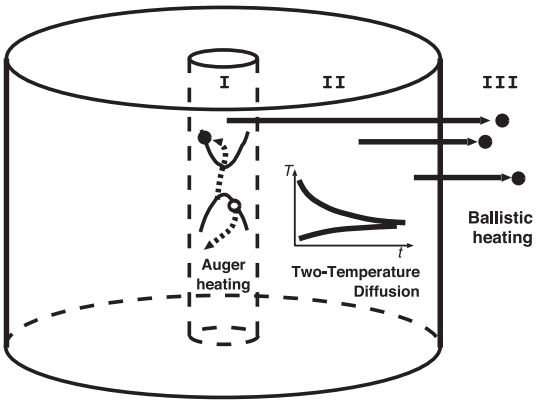

Figure 5.15: Three zone model: Zone I is the zone, where electrons are excited primarily by the ion beam. In this zone Auger decays lead to a continuous heating of the excited electrons. Electrons in zone II are created due to impact ionization due to collisions of electrons origination form zone I with the target atoms. This zone is populated by low energetic electrons, which are heating the target lattice via electron–phonon interactions. Electrons that move almost ballistically may escape Zone I and II and can travel deep into the target within zone III.

analyzed and indicate that three different zones around the ion impact point can be distinguished.

Zone I is located close around the ion impact point and has a radius of about 0.2 nm. The primary excitation induced by the ion occurs in this zone, leading to the creation of the δ–electrons and deep holes. These δ–electrons then propagate outwards from the center into zone II. The Auger recombination of the deep holes leads to a further creation of high energy electrons, which can be considered as a continuous Auger heating of the electrons located in zone I.

During their propagation through zone II, the high energetic electrons scatter with atoms leading to the creation of secondary electrons. These secondary electrons are less energetic than the electrons originating from zone I and exhibit a thermal character.

Finally the electrons, which originate in the first zone, can reach zone III, if they move almost ballistically trough the crystal. Figure 5.15 shows these three zones schematically.

The influence of the high energetic electrons is very complex. Apparently these electrons can not be described using a thermal description in the sense of Fermi distribution or a temperature. The influence of these almost ballistically moving electrons is that the energy transport can not be modeled using a thermal diffusion approach. This was quite dramatically demonstrated in figure 5.7. The energy transport depicted there shows a strong deviation from a pure exponential, which is the solution of a diffusion equation. The increase of the energy/temperature can not be explained in terms of thermal electrons. Additionally the ballistic character of the δ–electrons does not allow to separate the spacial and temporal evolution of these electrons,

which are used quite often throughout the literature for the calculation of ion induced modifications. The same conclusion was drawn by Akkerman et al. [85], who performed a very similar spatial and temporal analysis for the irradiation of silicon.

Finally, the electron and lattice temperature evolution was calculated using the TTM. The lattice temperature exceeded the melting temperature within a diameter of 3.3 nm, which corresponds well to the obtained diameter of the experimentally observed modification on a very similar irradiation scenario [88].

6 Outlook

In this section an outlook of future study topics will be presented.

6.1 Density Dependent TTM

The calculations performed in the previous chapter made use of the output provided by the Monte Carlo (MC) calculation. Most important were the spatially dependent electron number density (figure 5.2) and the spatially dependent electron energy density (figure 5.1). Obviously it is not valid to assume a constant electron number density along the track radius. Instead the density predicted by the MC calculation was used. However, in the present implementation of the TTM the density gradient was not taken into account *explicitly*, *i.e.* the value of the density was considered individually at each space point, but no effects of the gradient itself. Therefore, the solid computed within the presented MC–TTM approach will exhibit a permanent space charge around the ion impact point. Thus it is important to account for the relaxation of the electron density gradient within the TTM part of the model. A possible approach based on a TTM which includes a variable electron density and accounts for the density gradient was presented by H. van Driel [112] for the case of picosecond laser irradiation of semiconductors. The basic idea of van Driel is as follows. The incorporation of the density gradient consequently leads to a particle transport equation for the electron density n_e, which is related to the electron current $\vec{J}$. This current will drive the electrons into a local equilibrium, *i.e.* a homogeneous electron density. However, the excitation of electrons into the conduction band of a band gap material will lead to the creation of electron–hole pairs. The excess energy released during the recombination of an electron and a hole via Auger decay is spend to increase the energy of the electrons system in the conduction band.

A possible incorporation of this energy release in the TTM was presented in section 5.3.4. However, Auger recombination of electron–holes pairs also results in the decrease of the overall density of the electron gas and will therefore affect the electron density evolution. Furthermore, energetic electrons may have enough energy to ionize target atoms, so–called impact ionization. Thus, the electrons spends parts of its energy to excite other electrons into the conduction band, effectively increasing the electron density. This effect was also observed in the MC calculations presented in the last chapter. These impact ionization processes as well as the decay of holes, was identified to be of major importance for the description of swift heavy ion interactions with dielectrics. Therefore, both processes have to be included within the TTM part of the MC–TTM presented model. The evolution of the electron density n_e can in principle be expressed as

$$\frac{\partial n_e}{\partial t} = -R + II - \nabla \cdot \vec{J}, \tag{6.1}$$

where R and II represent recombination and impact ionization rates, respectively. Equation (6.1) describes the spatial and temporal change of the electron density. As the electron properties like the heat capacity and the diffusivity depend on the electron density (see sections

5.5 and 5.3.2, respectively), eq. (6.1) has to be solved in addition to the coupled electron and phonon heat diffusion equations.

6.2 Synchronized MC–TTM

The general idea of combining Monte Carlo and the two temperature model (MC–TTM) is, that within the MC part of the model the dynamics of individual electrons are calculated. Once these electrons show a sufficient thermal character, *i.e.* diffusive transport and Fermi like distribution, the MC calculations are stopped and the energy and number density is then used as initial conditions for the TTM. Thus, the MC and the TTM parts are subsequently performed.

The MC–TTM model presented in the previous sections focused on the application for dielectrics. Such materials, for instance the studied SiO_2, have large band gaps. The energy loss of the penetrating projectiles leads to the excitation of electrons. Ideally it is assumed that there are no free states in the band gap, *i.e.* impurities. Thus the ion's energy loss is spend to excite the electrons from the valence band into the conduction band. In this context it is quite obvious to separate between electrons within the valence band and such electrons in the conduction band. Within the presented Monte Carlo scheme, trajectories are only calculated for electrons within the conduction band, so called free electrons.

If the material exhibits a small band gap, the same formalism can be applied as presented, with the difference that more electrons occupy the conduction band while also the valance band electrons have to be considered.

In this section, a modification of the MC–TTM model will be proposed which is capable to deal with a large number of electrons, both in the valance as well as in the conduction band of the target.

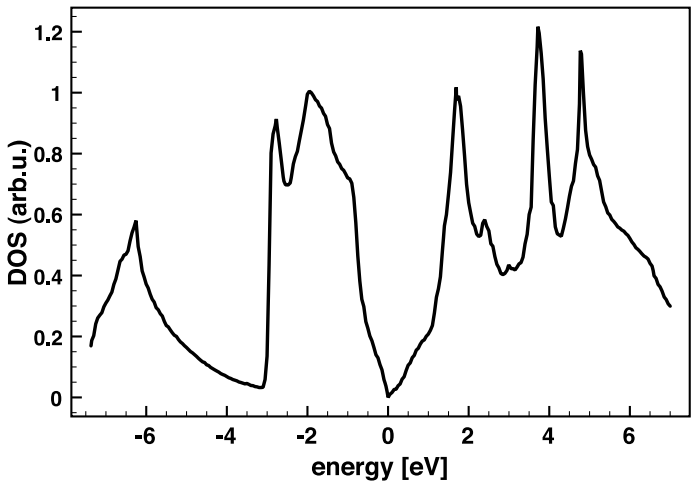

Figure 6.1: The electron density of states for amorphous germanium. Reproduced from [113]

As a target model system, amorphous germanium (a–Ge) is chosen. Figure 6.1 shows the electron density of states for a–Ge [113]. As can be seen, a–Ge does not have a band gap, both the valence and the conduction band are touching each other at the Fermi–edge. Thus a–Ge exhibits an non–zero electron density in the conduction band at room temperature. Another

consequence of this zero band gap is the fact that there is no minimal energy required to excite an electron into the conduction band, in principal an infinite small amount of energy will suffice. Thus a separation between valence and conduction band electrons as was done so far is no longer feasible. The proposed approach is as follows.

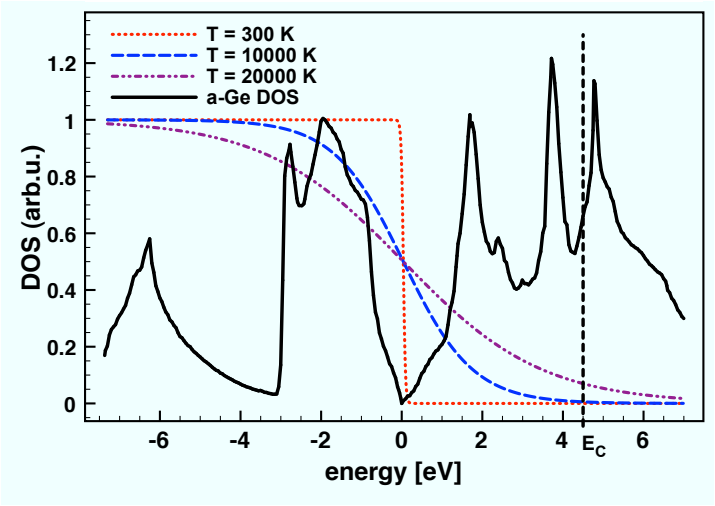

Figure 6.2: The electron density of states for amorphous germanium and the Fermi distribution function at different electron temperatures.

For simplicity, an equilibrium electron distribution function is considered. The density of states of a–Ge is superimposed with the Fermi distribution at different temperatures, as is shown in figure 6.2. With increasing electron temperature, a number of electrons is excited into the conduction band. The conduction band of the target can be separated into two regions. The first region starts from the Fermi–edge and stretches up to a certain cut–off energy E_C. All electrons, which are excited into this energy interval, are treated as thermalized. The second region starts at this cut–off energy and stretches into infinity. All electrons excited into this energy interval are considered to be non–thermal, *i.e.* ballistically moving. Electrons in region two are treated using the same algorithm as is presented in section 5.2. In the case of the electrons in region one, only the total energy of those electrons is considered. Thus, if an electron is excited due to impact ionization, the electron energy will either be in region one or two.

The first case is the case, where the electron is excited with an energy $E > E_c$. This electron is energetically in region two and will be treated as a free electron within the Monte Carlo method. Thus for every electron excited either directly by the penetrating ion or indirectly due to impact ionization, with an energy larger than the cut–off energy, the number of electrons considered explicitly with the Monte Carlo method increases. Electrons, which are excited with energies smaller than this cut–off energy, are considered as thermalized and the total energy of these thermalized electrons increases by that amount.

Consider now the case of an electron created by an impact ionization process with an energy of $E < E_c$. The energy of this electron is then 'added' to the total energy density of all electrons in region one and is not considered explicitly any more. Consequently, the number density of these electrons increases accordingly. Using the calculated number and energy density allows to compute the temperature of these electrons as well as the heat capacity, as was demonstrated in

sections 5.4.2 and 5.5, respectively. Thus, at every time step for every space point, the energy of these thermal energy electrons is updated and the new temperature can be calculated. The benefit of this approach is two–fold. First, the number of electrons that have to be considered explicitly within the Monte Carlo method is numerically manageable. Second, by assuming that the electrons in region one are thermalized, these electrons can be treated within the TTM. Within the same time step, the transport of the high energetic electrons are treated within the MC method, while the thermal electrons are propagating according to the TTM calculations.

This approach is a significant improvement compared to the model presented in section MC–TTM, since both kind of electrons, thermal and non thermal, are calculated at the same time step using the appropriate description, *i.e.* a kinetic model for ballistic and and continuous model for thermal electrons.

Considering this synchronized MC–TTM some open questions remain. The most obvious being the value of the cut–off energy. In the example shown in figure 6.2, the cut–off energy is chosen to be 4.5 eV. This value is chosen more or less randomly. From a numerical point of view, E_C determines how much electrons have to be followed in region two, *i.e.* have to be treated explicitly by the MC method. Thus a too small value will result in a large computation time. On the other hand, a value too large, will result in too few electrons populating region two and thus in poor statistics. From a physical point of view, a criterion for the value of E_C has yet to be determined.

A first run of this synchronized MC–TTM was performed for 185 MeV Au in a–Ge. The results were promising, however, no detailed analysis was performed at the present time.

7 Summary

In the present thesis the interaction of swift heavy ions with matter was studied. During the penetration of a beam of swift heavy ions through a target, the ions may lose or capture electrons due to charge exchange processes. The charge fractions of the ion beam can be calculated using computer codes like the ETACHA code. The ETACHA code was developed in 1994 and employs rate equations, which require cross–sections as input. ETACHA generates these cross–sections for electron capture, loss and excitation/deexcitation processes.

In this thesis a new model to calculate charge exchange processes was explored, the so called matrix method. This method takes the form of a simple algebraic expression. Like the rate equations, the matrix method uses cross–sections as input. From a physical point of view, both methods are equal. While in the presented implementation of the matrix method the cross–sections are taken from the ETACHA code, no excitation/deexcitation or Auger decay processes are included.

The charge fractions computed from both the matrix method as well as the ETACHA code have been compared for the case of carbon ions at different energies in a carbon target. It was observed that the charge fractions obtained using the ETACHA code suffer from numerical artifacts, which take the form of kinks in the charge fraction distribution or unphysical asymptotic behavior. All of these artifacts are completely avoided within the matrix method. From a numerical point of view the matrix method has proven to be a fast and robust tool. Computation times even for a very large number of charge states are in the second to minute regime. Comparisons of the calculated charge fractions using the matrix method and the ETACHA code have shown that for fast projectiles both methods are in excellent agreement with each other. However, the charge fractions computed using the matrix method show deviations from the charge fractions predicted by the ETACHA code for low ion energies. The reason for these deviations is most likely the fact that at the moment excitation and deexcitation processes are not included in the matrix method.

Computed charge fractions using both the matrix method as well as the ETACHA code have been compared with experimental measurements of charge fractions. From this comparison it was found that neither of the methods achieved a satisfactory agreement with the experiments. Most importantly, it was observed that the matrix method significantly overestimated the equilibrium depth. This overestimation stems from the fact that no Auger decay processes are included within the matrix method.

Finally, the equilibrium charge with respect to the ion energy was compared with the Thomas–Fermi estimate. This comparison demonstrated that the matrix method significantly overestimates the equilibrium charge. The origin of this overestimation is not yet fully understood, but may again be caused due to neglecting excitation/deexcitation and Auger decay processes.

A possible incorporation of the Auger decay was presented in section 3.7.3. Excitation processes may be included by taking one or more effective excited states into account, while a loss cross–section can be computed using any theory that can handle the ionization of atoms, like the binary collision theory. In order to include accurate capture cross–sections, different

scaling rules have been presented in section 3.8. When these processes are included, it is expected that the matrix method will produce reliable predictions of the charge fractions of swift heavy ions.

During the penetration, the ion loses part of its kinetic energy due to inelastic collisions with the target electrons. The energy lost by the ion is used to excite the electrons of the target. The excited electrons deexcite by electron–phonon interactions, which result in the emission of phonons. In the case of dielectrics, this lattice heating then may lead to the melting of the target and finally to the creation of defects in the target, so called ion tracks. This track creation is often explained in terms of a two temperature model (TTM), a set of two heat diffusion equations, coupled by an exchange parameter, the so called electron–phonon coupling parameter. This model was studied in detail in section 4.

The TTM requires certain material parameters as input such as the aforementioned electron–phonon coupling parameter, the electron heat diffusion and the electron heat capacity. These parameters are often unknown, especially for insulators and semiconductors. Furthermore, the number density of the excited electrons enters the TTM via the material parameters. In section 4.7 the TTM was applied to the irradiation of a dielectric target with a swift heavy ion. The calculation was aimed at calculating the so called damage threshold, *i.e.* the minimal ion energy necessary to induce a defect in the target. However, parameters like the electron–phonon coupling and the number density of the excited electrons are unknown, so that they were treated as free parameters. To study the effect of these parameters on the TTM, they were varied and the damage threshold was computed for this set of parameters. It was found that by changing the electron–phonon coupling parameter within one order of magnitude, the variation of the calculated damage threshold was almost a factor of three. Similar effects were observed, when the number density of the excited electrons was changed. From these results it is obvious that without a profound knowledge of the material parameters and the number density of the excited electrons reliable estimations, of the track radius and the damage threshold, for instance, using the TTM can not be expected.

In order to determine the density of the electrons, a method which is capable to deal with the ionization of target atoms induced by the ions energy loss, as well as to calculate the temporal evolution of a rather large number of electrons with spatial resolution is introduced. The method applied for it was the Monte Carlo (MC) method. A short overview of such an approach was presented in section 5.2. The main output of the MC simulations are the number density and the energy density of the excited electrons. It was shown that, using the MC method, it is possible to estimate material parameters like the electron diffusivity, the electron–phonon coupling as well as the electron heat capacity and how these quantities can be implemented within the TTM (see sections 5.3.2, 5.3.3 and 5.5, respectively).

The excitation of electrons by the ion leads to a perturbation of the electron distribution function. Therefore, the electrons are believed to be in a non–equilibrium state after the ion impact. Using the number density and the energy density of the excited electrons, it was demonstrated that it is possible to determine whether the electrons may be described by a Fermi distribution, by exploiting moments over the Fermi distribution function. It was found that electrons can not be treated as thermalized prior to 100 fs after the ion impact. The analysis revealed three distinct zones within the track. The first zone is close to the ion impact point and is populated by high energetic electrons, so called δ–electrons, which were initially created by the penetrating ion. These electrons traverse through the target and may excite other electrons due to impact ionization of target atoms. These electrons are usually called secondary electrons. The secondary electrons, mainly populating zone II, have lower

kinetic energies and exhibit a thermal character.

The analysis of the energy density transport calculated within the MC method revealed that the energy/temperature transport can–not be described by using thermal electrons, but that a significant amount of energy is carried away from the ion track due to the ballistic transport behavior of the δ–electrons.

Finally, the MC–TTM model was applied to calculate the track radius induced by the penetration of a swift heavy ion. It was found that the track radius is in good agreement with experimental measurements of the track radius for a very similar irradiation scenario. The good agreement between the model and the experiments is a strong indication that the MC–TTM model is very capable to determine the track radius in dielectrics induced by a swift heavy ion. In section 6 it was suggested, how the MC–TTM model could be applied for a system with a small or even vanishing band gap.

The interaction of swift heavy ions with matter is indeed a very complicated task. Within this thesis, a first step in improving the description of these interactions, especially the track creation process was done. Many open questions have been answered, while many more new questions arouse. But this is a tale for another time.

Bibliography

[1] J. J. Thomson. Cathode rays. *Phil. Mag.*, 44:293, 1897.

[2] E. Rutherford. The scattering of alpha and beta particles by matter and the structure of the atom. *Phil. Mag.*, 21:669–688, 1911.

[3] N. Bohr. On the theory of the decrease of velocity of moving electrified particles on passing through matter. *Phil. Mag.*, 25:10–31, 1913.

[4] J. Chadwick. The existence of a neutron. *Proc. R. Soc. A*, 136:692–708, 1932.

[5] J.D. Cockcroft and E.T.S. Walton. Artificial production of fast protons. *Nature*, 129:242, 1932.

[6] L. Meitner and O. Frisch. Disintegration of uranium by neutrons: a new type of nuclear reaction. *Nature*, 143:239, 1939.

[7] E. Fermi. The development of the first chain reaction pile. *Proc. Am. Philos. Soc.*, 90:20–24, 1946.

[8] A.K. Nix, H.G. Gehrke, J. Krauser, C. Trautmann, A. Weidinger, and H. Hofsäss. Track-etched nanopores in spin-coated polycarbonate films applied as sputtering mask. *Nucl. Instr. and Meth. B*, 267(6):1032 – 1034, 2009.

[9] S. Akcöltekin, H. Bukovska, T. Peters, O. Osmani, I. Monnet, I. Alzaher, B. Ban d'Etat, H. Lebius, and M. Schleberger. Unzipping and folding of graphene by swift heavy ions. *AIP*, 98:103103, 2011.

[10] P. Sigmund. *Particle penetration and radiation effects.* Springer Berlin Heidelberg New York 2006.

[11] L. Meitner and K. Freitag. Über die α-Strahlen des ThC+c' und ihr Verhalten beim Durchgang durch verschiedene Gase. *Z Physik*, 37:481–517, 1926.

[12] N.G. van Kampen. *Stochastic Processes in Physics and Chemistry.* North-Holland, Amsterdam, 2007.

[13] O. Osmani and P. Sigmund. Charge evolution of swift–heavy–ion beams explored by matrix method. *Nucl. Instr. and Meth. B*, 269:813–816, 2010.

[14] P. Sigmund, O. Osmani, and A. Schinner. Charge–exchange straggling in equilibrium. *Nucl. Instr. and Meth. B*, 269:804–809, 2010.

[15] L. Flamm and R. Schumann. Die Geschwindigkeitsabnahme der α–Strahlen in Materie. *Ann. Phys.*, 50:655, 1916.

[16] G. H. Henderson. Changes in the charge of an α-particle passing through matter. *Proc. R. Soc. A*, 102:496, 1922.

[17] E. Rutherford. The capture and loss of electrons by alpha particles. *Phil. Mag.*, 47:277, 1924.

[18] N. Bohr. The penetration of atomic particles through matter. *Mat. Fys. Medd. Dan. Vid. Selsk.*, 18:8, 1948.

[19] S. K. Allison. Experimental results on charge–changing collisions of hydrogen and helium atoms and ions at kinetic energies above 0.2 kev. *Rev. Mod. Phys.*, 30:1137, 1958.

[20] N. Bohr and J. Lindhard. Electron capture and loss by heavy ions penetrating through matter. *Mat. Fys. Medd. Dan. Vid. Selsk.*, 28:7, 1954.

[21] H. D. Betz. Charge states and charge–changing cross sections of heavy ions penetrating trhoug gaseous and solid media. *Rev. Mod. Phys.*, 44:465, 1972.

[22] J.P. Rozet, C. Stephan, and D. Verhet. ETACHA: a program for calculating charge states at GANIL energies. *Nucl. Instr. and Meth. B*, 107:67, 1996.

[23] A. Blazevic, H. G. Bohlen, and W. von Oertzen. Charge-state changing processes for Ne ions passing through thin carbon foils. *Phys. Rev. A*, 61:032901, 2000.

[24] P. Sigmund, A. Gras-Marti, and H. M. Urbassek. *Interaction of charged particles with solids and surfaces.* NATO ASI Series (Plenum Press, New York, 1991), 1991.

[25] P. Sigmund. Statistical theory of charged–particle stopping and straggling in the presence of charge exchange. *Nucl. Instr. and Meth. B*, 69:113, 1992.

[26] C. Moler and C. V. Loan. Nineteen doubious ways to compute the exponent of a matrix. *SIAM Rev.*, 20:801, 1978.

[27] G. P. Library. Gnu sientific library.

[28] J. P. Rozet, A. Chetioui, P. Piquemal, D. Vernhet, K. Wohrer, C. Stephan, and L. Tassan-Got. Charge–state distributions of few–electron ions defuced from atomic cross-sections. *J. Phys. B: At. Mol. Opt. Phys.*, 22:33, 1989.

[29] J. Eichler. Relativistic eikonal theory of electron capture. *Phys. Rev. A*, 32:112, 1985.

[30] H. A. Bethe and E. E. Salpeter. *Quantum Mechanics of One- and Two-Electron Atoms.* (Plenum, New York, 1977).

[31] M. Imai, M. Sataka, K. Kawatsura, K. Takahlro, K. Komaki, H. Shibata, H. Sugai, and K. Nishio. Charge state evolution of 2 MeV/u sulfur ion passing through thin carbon foils. *Nucl. Instr. and Meth. B*, 256:11, 2007.

[32] M. Imai, M. Sataka, K. Kawatsura, K. Takahlro, K. Komaki, H. Shibata, H. Sugai, and K. Nishio. Equilibrium and non–equilibrium charge–state distributions of 2 MeV/u sulfur ions passing through carbon foils. *Nucl. Instr. and Meth. B*, 267:2675, 2009.

[33] D. Vernhet, J. P. Rozet, K. Wohrer, L. Adui, C. Stephan, A. Cassimi, and J. M. Ramillon. Exitation in swift heavy ion–atom collisions. *Nucl. Instr. and Meth. B*, 107:71, 1996.

[34] W. Fritsch and C. D. Lin. The semiclassical close–coupling description of atomic collisions: recent developments and results. *Review section of physics letters*, 1&2:1–97, 1991.

[35] M. S. Weng, A. Schinner, A. Sharma, and P. Sigmund. Primary electron spectra from swift heavy-ion impact: Scaling relations and estimates from modified Bohr theory. *Eur. Phys. J. D*, 39:209, 2006.

[36] P. Sigmund and A. Schinner. Electron ejection in collisions between swift heavy ions and atoms. *Nucl. Instr. and Meth. B*, 258:116, 2007.

[37] D. P. Dewangan and J. Eichler. Charge exchange in energetic ion–atom collisions. *Physics Reports*, 59:219, 1994.

[38] Dz. Belkic, R. Gayet, and A. Salin. Computation of total cross-sections for electron capture in high energy ion-atom collisions I. *Computer Physics Communications*, 23(2):153 – 167, 1981.

[39] Dz. Belkic, R. Gayet, and A. Salin. Computation of total cross-sections for electron capture in high energy collisions. II. *Computer Physics Communications*, 30(2):193 – 205, 1983.

[40] Dz. Belkic, R. Gayet, and A. Salin. Computation of total cross-sections for electron capture in high energy collisions. III. *Computer Physics Communications*, 32(4):385 – 397, 1984.

[41] N.O. Lassen. Total charges of fission fragments as functions of the pressure in the stopping gas. *Mat. Fys. Medd. Dan. Vid. Selsk.*, 26:1–19, 1951.

[42] N.O. Lassen. Total charges of fission fragments in gaseous and solid stopping media. *Mat. Fys. Medd. Dan. Vid. Selsk.*, 26:1–28, 1951.

[43] A. S. Schlachter, J. W. Fstearns, W. G. Graham, K. H. Berkner, R. V. Pyle, and J. A. Tanis. Electron capture for dast highly charged ions in gas targets: An empirical scaling rule. *Phys. Rev. A*, 27:11, 1983.

[44] V. P. Shevelko, Th. Stöhlker, H. Tawara, I. Yu. Tolstikhina, and G. Weber. Electron capture in intermediate-to-fast heavy ion collisions with neutral atoms. *Nucl. Instr. and Meth. B*, 268:2611, 2010.

[45] V. Shevelko, O. N. Rosmej, H. Tawara, and I. Y. Tolstikhina. The target-density effect in electron-capture processes. *J. Phys. B.: At. Mol. Opt. Phys.*, 37:201, 2004.

[46] H. Knudsen, H. K. Haugen, and P. Hvelplund. Single–electron–capture cross section from medium– and high–velocity, highly charged ions with atoms. *Phys. Rev. A*, 23:597, 1981.

[47] P. Sigmund. *Stopping of heavy ions.* Springer, 2004.

[48] K. Shima, T. Ishihara, and T. Mikumo. Empirical formula for the average equilibrium charge–state of heavy ions behind various foils. *Nucl. Instr. and Meth. B*, 200:605, 1982.

[49] V. L. Ginzburg and V. R. Shabanskiy. *Dokl. Akad. Nauk SSSR*, 100:445, 1955.

[50] F. Seitz and J. Köhler. Displacement of atoms during irradiation. *Solid State Phys.*, 2:305, 1956.

[51] M. I. Kaganov, I. M. Lifshitz, and L .V. Tanatarov. Relaxation between electrons and the crystalline lattice. *Soviet Phys. JETP*, 4:232, 1957.

[52] M. I. Kaganov, I. M. Lifshitz, and L .V. Tanatarov. *Reactor Sci.*, 12:69, 1960.

[53] S.I. Anisimov, B.L. Kapeliovich, and T.L. Perel'man. Electron emission from metal surfaces exposed to ultrashort laser pulses. *Sov. Phys. JETP*, 39:375, 1974.

[54] Dmitriy S. Ivanov and Leonid V. Zhigilei. The effect of pressure relaxation on the mechanisms of short pulse laser melting. *Phys. Rev. Lett.*, 91:105701, 2003.

[55] M. Lisowski, P.A. Loukakos, U. Bovensiepen, J. Stahler, C. Gahl, and M. Wolf. Ultrafast dynamics of electron thermalization, cooling and transport effects in Ru(001). *Appl. Phys. A*, 78:165, 2004.

[56] A. Meftah, J.M. Costantini, N. Khalfaoui, S. Boudjadar, J.P. Stoquert, F. Studer, and M. Toulemonde. Experimental determination of track cross-section in $Gd_3Ga_5O_{12}$ and comparison to the inelastic thermal spike model applied to several materials. *Nucl. Instr. and Meth. B*, 237(3-4):563–574, August 2005.

[57] M. Borghesi, P. Audebert, S.V. Bulanov, T. Cowan, J. Fuchs, J.C. Gauthier, A.J. Mackinnon, P.K. Patel, G. Pretzler, L. Romagnani, A. Schiavi, T. Toncian, and O. Willi. High-intensity laser-plasma interaction studies employing laser-driven probes. *Laser and Particle Beams*, 23(03):291–295, 2005.

[58] O. N. Rosmej, S.A. Pikuz, S. Korostiy, A. Blazevic, E. Brambrink, A. Fertman, T. Mutin, V.P. Shevelko, V.P. Efremov, T.A. Pikuz, A.Ya. Faenov, P. Loboda, A.A. Golubev, and D.H.H. Hoffmann. Radiation dynamics of fast heavy ions interacting with matter. *Laser and Particle Beams*, 23(03):396–396, 2005.

[59] E. Akcöltekin, T. Peters, R. Meyer, A. Duvenbeck, M. Klusmann, I. Monnet, H. Lebius, and M. Schleberger. Creation of multiple nanodots by single ions. *Nat. Nanotechnol.*, 2(5):290–294, May 2007.

[60] C. Strangio, A. Caruso, D. Neely, P.L. Andreoli, R. Anzaloner, R. Clarker, G. Cristofari, E. Del Prete, G. Di Giorgio, C. Muhrphy, C. Ricci, R. Stevens, and M. Tolley. Production of multi-MeV per nucleon ions in the controlled amount of matter mode (CAM) by using causally isolated targets. *Laser and Particle Beams*, 25(01):85–91, 2007.

[61] E. Akcöltekin, S. Akcöltekin, O. Osmani, A. Duvenbeck, H. Lebius, and M. Schleberger. Swift heavy ion irradiation of $SrTiO_3$ under grazing incidence. *New J. Phys.*, 10:053007, 2008.

[62] A.F. Akkerman. Modeling charged particles trajectories in matter. *EnergoAtomIzdat, Moscow*, 1991.

[63] A.F. Akkerman, Yu.M. Nikitushev, and V.A. Botvin. *Monte-Carlo Solutions of Problems of fast Electron Transport in Matter [in russian].* Nauka, Alma-Ata, 1971.

[64] I. A. Baranov, Yu. V. Martynenko, S. O. Tsepelevich, and Yu. N. Yavlinski. Inelastic sputtering of solids by ions. *Usp. Fiz. Nauk*, 156(11):477, 1988.

[65] N.J. Carron. *An Introduction to the Passage of Energetic Particles through Matter.* 3rd ed. (Taylor and Francis Group, New York - London), 2007.

[66] C. Dufour, A. Audouard, F. Beuneu, J. Dural, J. P. Girard, A. Hairie, M. Levalois, E. Paumier, and M. Toulemonde. A high-resistivity phase induced by swift heavy-ion irradiation of Bi: a probe for thermal spike damage? *J. Phys.: Condens. Matter*, 5:4573, 1993.

[67] M. Toulemonde, C. Dufour, G. Wang, and E. Paumier. Atomic and cluster ion bombardment in the electronic stopping power regime: A thermal spike description. *Nucl. Instr. and Meth. B*, 112:26, 1996.

[68] M.P.R. Waligorski, R.N. Hamm, and R. Katz. The radial distribution of dose around the path of a heavy ion in liquid water. *Nucl. Tracks Radiat. Meas.*, 11:309, 1986.

[69] J.F. Ziegler and J.P. Biersack. *The stopping and range of ions in matter (SRIM).* http://www.srim.org/, 2008.

[70] X Y. Wang, D.M. Riffe, Y.S. Lee, and M.C. Downer. Time–resolved electron-temperature measurement in a highly excited gold target using femtosecond thermionic emission. *Phys. Rev. B*, 50:8016, 1994.

[71] O. Osmani, N. Medvedev, B. Rethfeld, and M. Schleberger. Excitation and relaxation of swift heavy ion irradiated dielectrics. *e-J. Surf. Sci. Nanotech.*, 8:278, 2010.

[72] P. G. Klemens. Thermal resistance due to point defects at high temperature. *Phys. Rev.*, 119:507–509, 1960.

[73] Z. Lin, Leonid V. Zhigilei, and V. Celli. Electron-phonon coupling and electron heat capacity of metals under conditions of strong electron-phonon nonequilibrium. *Phys. Rev. B*, 77:075133 1–17, 2008.

[74] Z. G. Wang, C. Dufour, E. Paumier, and M. Toulemonde. The S_e sensitivity of metals under swift-heavy-ion irradiation: a transient process. *J. Phys. : Condens. Matter*, 6:6733, 1994.

[75] P. Drude. Zur Elektronentheorie der Metalle. *Ann. Phys.*, 306:566, 1900.

[76] P. Drude. Zur Ionentheorie der Metalle. *Phys. Z*, 1:161, 1900.

[77] P. B. Allen. Theory of thermal relaxation of electrons in metals. *Phys. Rev. Lett.*, 59:331, 1987.

[78] M. Karlušić, S. Akcöltekin, Orkhan Osmani, I. Monnet, H. Lebius, M. Jakšić, and M. Schleberger. Energy threshold for the creation of nanodots on $SrTiO_3$ by swift heavy ions. *New Journal of Physics*, 12(4):043009, 2010.

[79] R.F. Wood and G.E. Giles. Macroscopic theory of puls–laser annealing. I. thermal transport and melting. *Phys. Rev. B*, 23:2923—2942, 1981.

[80] M. Toulemonde, C. Dufour, and E. Paumier. Transient thermal process after a high-energy heavy-ion irradiation of amorphous metals and semiconductors. *Phys. Rev. B*, 46:14362–14369, 1992.

[81] J.K. Chen, D.Y. Tzou, and J.E. Beraun. Numerical investigation of ultrashort laser damage in semiconductors. *Int. J. Heat Mass Transfer*, 48(3-4):501 – 509, 2005.

[82] S. Mukherji. Calculation of the mean ionization potentials of the elements for stopping-power computations. *Phys. Rev. B*, 12:3530–3532, 1975.

[83] N. Medvedev and B. Rethfeld. A comprehensive model for the ultrashort visible light irradiation of semiconductors. *J. Appl. Phys.*, 108:103112, 2010.

[84] O. Osmani, I. Alzaher, T. Peters, A. Ban d'Etat, B.and Cassimi, H. Lebius, I. Monnet, N. Medvedev, B. Rethfeld, and M. Schleberger. Damage in crystalline silicon by swift heavy ion irradiation. *Nucl. Instr. and Meth. B*, Accepted, 2011.

[85] A. Akkerman, M. Murat, and J. Barak. Ion track structure calculations in silicon – spatial and temporal aspects. *Nucl. Instr. and Meth. B*, 269:1630, 2011.

[86] N. Medvedev, O. Osmani, B. Rethfeld, and M. Schleberger. Track creation after swift heavy ion irradiation of insulators. *Nucl. Instrum. And Meth. B*, 268:3160, 2010.

[87] O. Osmani, N. Medvedev, B. Rethfeld, and M. Schleberger. Energy dissipation in dielectrics after swift heavy ion impact: a hybrid model. *Phys. Rev. B (Accepted)*, 2011.

[88] P. Kluth, C.S. Schnohr, O.H. Pakarinen, F. Djurabekova, D.J. Sprouster, R.Giulian, M.C. Ridgway, A.P. Byrne, C. Trautmann, D.J. Cookson, K. Nordlund, and M. Toulemonde. Fine structure in swift heavy ion tracks in amorphous SiO_2. *Phys. Rev. Lett.*, 101(17):175503, 2008.

[89] B. Rethfeld, A. Kaiser, M. Vicanek, and G. Simon. Ultrafast dynamics of nonequilibrium electrons in metals under femtosecond laser irradiation. *Phys. Rev. B: Condens. Matter*, 65:214303, 2002.

[90] B. Rethfeld, K. Sokolowski-Tinten, D. von der Linde, and S. I. Anisimov. Ultrafast thermal melting of laser-excited solids by homogeneous nucleation. *Phys. Rev. B*, 65(9):092103, Feb 2002.

[91] N. Medvedev, A.E. Volkov, N. Shcheblanov, and B. Rethfeld. Early stage of the electron kinetics in swift heavy ion tracks in dielectrics. *Phys. Rev. B*, 82:125425, 2010.

[92] N. Medvedev, A.E. Volkov, B. Rethfeld, and N. Shcheblanov. Effect of inter-atomic auger processes on relaxation of electronic vacancies at deep levels of highly ionized atoms in swift heavy ion tracks. *Nucl. Instr. and Meth. B*, 268:2870–2873, 2010.

[93] M. Metropolis and S. M. Ulam. The monte carlo method. *J. Amer. Statist. Assoc.*, 44:335, 1949.

[94] M. J. Berger. *Methods in computational physics*. Academic Press, Inc., New York, 1963.

[95] I. Plante and F.A. Cucinotta. Cross sections for the interactions of 1 eV–100 MeV electrons in liquid water and application to Monte-Carlo simulation of HZE radiation tracks. *New J. Phys.*, 11:063047, 2009.

[96] A. Akkerman, J. Barak, and D. Emfietzoglou. Ion and electron track-structure and its effects in silicon: model and calculations. *Nucl. Instr. and Meth. B*, 227:319, 2005.

[97] W. Eckstein. *Computer Simulations of Ion-Solid Interactions*. Springer-Verlag, New York, 1991.

[98] B. Gervais and S. Bouffard. Simulation of the primary stage of the interaction of swift heavy ions with condensed matter. *Nucl. Instrum. Methods Phys. Res., Sect. B*, 88:355–364, 1994.

[99] N. Medvedev and B Rethfeld. Transient dynamics of the electronic subsystem of semiconductors irradiated with an ultrashort vacuum ultraviolet laser pulses. *New J. Phys.*, 12(7):073037, 2010.

[100] M. Gryzinski. Two-particle collisions. I general relations for collisions in the laboratory system. *Phys. Rev. A*, 138:302–336, 1965.

[101] N. Medvedev and B. Rethfeld. Effective energy gap of semiconductors under irradiation with a femtosecond VUV laser pulses. *Europhys. Lett.*, 99:55001, 2009.

[102] O. Keski-Rahkonen and M.O. Krause. Total and partial atomic-level widths. *Atomic Data and Nuclear Data Tables*, 14:139–146, 1974.

[103] M.L. Knotek and P.J. Feibelman. Stability of ionically bonded surfaces in ionizing environments. *Surface Science*, 90:78–90, 1979.

[104] C.N. Rao and D.D. Sarma. Interatomic auger transitions in transition-metal oxides. *Phys. Rev. B*, 25:2927, 1982.

[105] G.W. Wertheim, D.N. Rowe, J.E. Buchanan, and P.H. Citrin. Experimental interatomic auger rates in sodium halides. *Phys. Rev. B*, 51:13669–13674, 1995.

[106] M. Toulemonde, E. Paumier, and C. Dufour. Thermal spike model in the electronic stopping power regime. *Radiat. Eff. Defect. S.*, 126:201, 1993.

[107] O. Osmani, H. Lebius, B. Rethfeld, and M. Schleberger. Energy dissipation in insulators induced by swift heavy ions: A parameter study. *Laser and Particle Beams*, 28:229, 2010.

[108] P. Martin, S. Guizard, Ph. Daguzan, G. Petite, P. D'Oliveira, P. Meynadier, and M. Perdrix. Subpicosecond study of carrier trapping dynamics in wide-band-gap crystals. *Phys. Rev. B*, 55:5799–5810, 1997.

[109] F. Quéré, S. Guizard, P. Martin, G. Petite, O. Gobert, P. Meynadier, and M. Perdrix. Ultrafast carrier dynamics in laser-excited materials: subpicosecond optical studies. *Applied Physics B: Lasers and Optics*, 68:459–463, 1999.

[110] G. Schiwietz, G. Xiao, P. L. Grande, E. Luderer, R. Pazirandeh, and U. Stettner. Determination of the electron temperature in the thermal spike of amorphous carbon. *EPL (Europhysics Letters)*, 47(3):384–390, 1999.

[111] A. Meftah, F. Brisard, J. M. Constantini, E. Dooryhee, M. Hage-Ali, M. Hervie, F. Studer, and M. Toulemonde. Track formation in SiO_2 quartz and the thermal-spike mechanisms. *Phys. Rev. B*, 49:12457, 1994.

[112] H.M. van Driel. Kinetics of high–density plasmas generated in Si by 10.6– and 0.53–μm picosecond laser pulses. *Phys. Rev. B*, 35:8166, 1987.

[113] F. Herman and J. P. Van Dyke. New interpretation of the electronic structure and optical spectrum of amorphous germanium. *Phys. Rev. Lett.*, 21:1575, 1968.

Acknowledgments

I would like to say, that i am very thankful to both my supervisors Dr. Bärbel Rethfeld and Prof. Dr. Marika Schleberger for the opportunity to work on this topic, which finally resulted in this thesis.

Although a distance of 312 km lay between both groups, i always felt at home.

Especially i want to appreciate the discussions and the chit–chat with Dr. Nikita Medvedev. What started which a shared office ended in a very promising model and friendship.

I owe a grate deal of gratitude to Prof. Dr. Peter Sigmund. Those months i spend in Odense where, sometimes stressful but always very enlightening. I am very thankful that he gave me the chance to learn and work with him.

Also i want to thank Prof. Dr. Preben Hvelplund and Prof. Dr. Helge Knudsen for the discussions about charge exchange and capture cross–sections. They gave me a big red book full of measured capture cross–sections, from which i used some in this thesis. I really hope i gave it back to them.